Spring 2015

ESTIMATING SURFICIAL SEAFLOOR SEDIMENT PROPERTIES USING AN EMPIRICAL ORTHOGONAL DECOMPOSITION ON ACOUSTIC BACKSCATTER WAVEFORM PROPERTIES

Joshua Lincoln Humberston
University of New Hampshire, Durham

ESTIMATING SURFICIAL SEAFLOOR SEDIMENT PROPERTIES USING AN EMPIRICAL ORTHOGONAL DECOMPOSITION ON ACOUSTIC BACKSCATTER WAVEFORM PROPERTIES

by

Joshua L. Humberston
B.S. Geological Sciences, University of Delaware, 2012

THESIS

Submitted to the University of New Hampshire
In Partial Fulfillment of
the Requirements for the Degree of

Master of Science
in
Oceanography

May 2015

ESTIMATING SURFICIAL SEAFLOOR SEDIMENT PROPERTIES

USING AN EMPIRICAL ORTHOGONAL DECOMPOSITION ON

ACOUSTIC BACKSCATTER WAVEFORM PROPERTIES

by

Joshua L. Humberston

This thesis/dissertation has been examined and approved in partial fulfillment of the requirements for the degree of Master of Science in Oceanography by:

Thomas Lippmann, Ph.D
Thesis Director, Associate Professor, Department of Earth Sciences

Larry Ward, Ph.D.
Resarch Associate Professor, Department of Earth Sciences

Semme Dijkstra, Ph.D.
Lecturer, Department of Ocean Engineering

On January 5, 2015

Original approval signatures are on file with the University of New Hampshire Graduate School.

ACKNOWLEDGMENTS

I would like to thank Tom Lippmann for being an exceptional advisor during this thesis work. From my last minute visit to the university nearly 3 years ago which convinced me to attend UNH until now, he has made himself available to help me at every turn and wisely guided me forward both in classes and research. I would also like to thank my other committee members, Semme Dijkstra and Larry Ward, for their help and support. I would like acknowledge NOAA and the New Hampshire DES for generously supporting my research efforts. Lastly, I would like to thank friends and family for their constant support in all my efforts, academic and otherwise.

TABLE OF CONTENTS

LIST OF FIGURES

ABSTRACT

ESTIMATING SURFICIAL SEAFLOOR SEDIMENT PROPERTIES

USING AN EMPIRICAL ORTHOGONAL DECOMPOSITION ON

ACOUSTIC BACKSCATTER WAVEFORM PROPERTIES

by

Joshua L. Humberston
University of New Hampshire, May, 2015

Seafloor classification and environmental assessment in shallow marine waters are crucial to habitat mapping, coastal management policies and maintaining navigational waterways. There are existing methods for remotely estimating some bottom properties, but the large variety of desired measured sediment properties frequently leads to insufficient quantifiable data to support marine policy decisions. This problem is exacerbated by the highly variable bottom composition of typical coastal and estuarine environments. In this work, field observations from an Odom Echotrac vertical-incidence echosounder with a 200 khz transducer were used to estimate seafloor sediment characteristics in regions with variable bottom types. Observations were obtained in water depths ranging 0.5-24 m of the Little Bay, New Hampshire, during February and March, 2013. Backscatter waveforms (the acoustic return representing the first interaction with the bottom) were analyzed and their properties compared to sediment grain size distributions. These comparisons showed varied degrees of predictive capability and require subjective *a priori* selection. In an effort to better capture the collective effects of seafloor sediment's composition on acoustic returns, empirical orthogonal functions (EOF's) were computed from an ensemble of seven waveform properties and compared with observed surficial sediment size fractions, bulk density, and porosity. A simple logarithmic model relating first mode EOF spatial variability to observed mud fractions explained 43% of the variability and well estimated the spatial pattern of mud across the bay from deep channels (with no mud) to high concentrations of mud on the shallower flats near the sides of the estuary. This method produced greater coverage and higher resolution predictions of mud fraction than could be obtained using traditional sediment measuring techniques. Deviations from the model are shown to be correlated with lower sediment porosity most likely due to river inflow from the Bellamy River draining into the Bay. Still, application of the model to a new area in the Great Bay, New Hampshire showed favorable results with RMS errors below 15% along two surveyed lines. This empirical analysis provides a first order objective means to interpret acoustic backscatter, an important step towards a widespread quantitative assessment of shallow water seafloor sediments.

Chapter 1

INTRODUCTION

Remote Mapping Background

Seafloor mapping typically focuses on measuring the elevation of submerged topography (bathymetry) with acoustic echosounders mounted on research vessels. An echosounder functions by sending specific electric signals to a carefully constructed piezoelectic sensor known as a transducer. The electric charges are converted to sound pulses which are directionally emitted from a submerged transducer at a prescribed frequency and propagate at sound speeds determined by the elasticity modulus of the water (a function of the temperature and salinity distribution of the water body) and angles determined by Snell's Law for wave refraction (Lurton, 2002). Acoustic energy associated with each sound pulse (ping) is attenuated in the water column by spherical spreading losses, scattering and absorption from suspended particulate matter, and volume scattering at the seabed (Jackson, D. and Briggs, K., 2013). Spherical and, in shallow water, cylindrical spreading and scattering affects are the dominant causes of transmission losses and can be accounted for analytically (e.g., Lurton, 2002 and Heggen, 2010).

The component of the acoustic signal reflected back towards the receiving transducer (backscatter) is converted to an electronic voltage by the transducer reordered as a raw voltage. Backscater is a function of depth and properties of the seafloor that affect the acoustic impedance, including characteristics of the sediment composition and compactness (a function of grain size and porosity). For estimation of bathymetry, the initial seafloor return is found through various digital search algorithms and the two-way travel time, the time duration from when the pulse is sent until the reflection is measured, is converted to depth using observed (or modeled) sound speed profiles. Information on seafloor surficial sediment composition or geotechnical properties is based on more in-depth analysis of the measured acoustic response and requires ground truth verification based on field measurements of seabed sedimentary properties.

The extraction of meaningful measurements from full acoustic backscatter data has been a topic of discussion for some time (Anderson, J., *et al*., 2008 and Anderston, 1992). Brown, *et al*. (2011) provides a good synopsis of some of the major remote characterization efforts over time. Over the last 10 to 15 years there have been studies that develop and improve remote seafloor classification and characterization techniques using acoustic methods (Alexandrou and Pantzartzis, 1993; Amiri-simkooei, *et al*., 2011; Clarke, 1994; Fonseca, *et al*., 2007; and others). These methods have taken different approaches and focused on the advantages of both single beam and multi-beam echo-sounding systems (MBES). Even in recent years as multi-beam systems have become the preferred mapping method in many environments, some groups such as Snellen, *et al*. (2011) and Haris, *et al*. (2012) have continued to explore the practicality of the use of single-beam echosounders for seafloor characterization and sediment classification. Single-beam studies, in conjunction with recent efforts to better interpret multi-beam data for the effects of high incident angles (Fonseca, *et al*., 2007 and Fonseca and Calder, 2005), have produced increasingly accurate seafloor characterizing methodologies.

Still, most classifications efforts have been centered on depicting general differences between soft (mud) and hard (rock) sediments. Relatively few studies have explored the potential for remote seafloor characterization in shallow to very shallow water and the possibility of relating acoustic responses to other sediment characteristics (Lyons and Abrahm, 1999 and Freitas, *et al*., 2008). One specific shallow marine environment that could greatly benefit from an effective remote bottom classification method is estuaries and their associated shallow bays.

Estuaries

Estuaries are highly variable inland water systems which vary in definition, but are frequently referred to as partially enclosed bodies of water open to the sea that extend to the upper limit of tidal rise (Fairbridge, 1980). On the east coast of the United States, most estuaries are drowned river valleys resulting from sea level rise. The hydrologic structure of estuaries is highly dependent on the amount of freshwater input from rivers, the tidal flux, and an estuary's morphology and bathymetry. Geologically, estuaries tend to be one of the most complex nearshore environments due to their underlyng morphology, sediment input levels and types, and

potentially strong tidal currents. In some estuaries, continuous maintenance dredging adds to the temporal variability of flow structure and the resulting sediment distribution.

Most estuaries serve as effective sediment traps for both fluvial and oceanic sediment inputs (Meade, 1969). Sediment from rivers is deposited into the main channels of an estuary during high flow periods. Over time, higher flows in the channels winnow away fine sediments leaving coarser or limited material in the deeper channels. The suspended fine grained sediment is frequently deposited in the lower flow regions along the sides of the estuary (Dronkers, 1986). The net result is a residual transport of fine-grained sediment towards the shallower banks and mudflats on the sides of the main channel. However, the combined effects of complex morphology, tidal variations, strong currents, and freshwater variations tend to complicate sediment distribution in estuarine environments. Bottom sediments can vary from exposed bedrock and large boulders to fine sands and mud.

The distribution of sediment types is of interest to various fields of study. For safety purposes, particularly in high trafficked shipping channels, hydrographic mapping surveys are concerned not only with bathymetry, but also seafloor composition. For example, a shoal composed of rock is a larger risk to vessels than a muddy shoal. Ecologically, estuaries can serve as habitats to a variety of organisms, both in the sediment and in the water column. Bottom composition is also of great importance in the consideration of nutrient fluxes, engineered structures and studies of sediment dynamics (Hasegawa, *et al.*, 2008; Airoldi, *et al*.; 2005, and Botto and Iribarne, 2000.)

However, due to difficulties and high time and financial costs, many physical interpretations and policy decisions are made in these fields based on limited field observations of seabed sedimentary material. This problem is exacerbated by the highly variable bottom composition of many estuaries. More extensive and more easily producible maps of bottom characteristics could improve hydrographic, ecologic, and engineering decision making in estuarine and other shallow water environments. Models that predict not only variations in sediment type, but also specific sediment properties such as mud fraction and median grain size, could greatly aid coastal scientists, engineers, and managers concerned with benthic properties and habitats (Atema, and Stenzler, 1977; Cogan, *et al*., 2009; and Correll, *et al*., 1992).

Introduction to Remote Seafloor Characterization

Shallow water remote seafloor characterization is often limited by sampling techniques in shallow water. Some work has been done with light distance and ranging (lidar) methods to remotely determine bottom characteristics in shallow water (Pe'eri and Long, 2011), but these techniques are bounded even in shallow water by increased turbidity in the water column. Several intermediate and deep water classification techniques have been applied with some success in shallow water, but their algorithms are not suited to resolve the rapidly varying sediment characteristics in these environments (Freitas, *et al*., 2008).

Different studies have used a variety of techniques to relate backscatter properties to bottom characteristics. Some approaches have compared the energy of the second return relative to the first while others have looked solely at the properties of the first return (Greenstreet *et al*., 1997; Mayer, 2006; Sternlicht and Moustier, 2003). The most recent work has focused on how data from multibeam systems can be adjusted to account for the effects of incident angle to better understand backscatter-sediment correlations across the full swatch (Fonseca, L and Mayer, L., 2007). While these new efforts have produced favorable results, one large drawback is the financial cost associated with carrying out an effective multibeam survey, particularly in shallow coastal waters where the footprint of a multibeam is greatly limited by depth. Fortunately, single-beam surveys often suffice for many scientific, commercial, and managerial purposes in shallow water environments, and are significantly lower in cost and more available to the wider community.

In this work, we consider an objective method of utilizing acoustic backscatter waveform properties for seafloor characterization in shallow water and develop an empirical model for estimating mud fraction in a shallow estuary, a potentially valuable tool for many scientific studies and policy decisions. Hughes-Clarke, et al. (1996) noted that "the remote characterization of the seafloor [by acoustic methods] has important practical application in a broad range of disciplines, including marine geologic, geotechnical, hydrographic, biological, fisheries and environmental research" (Hughes-Clarke *et al*., 1996). This increasingly holds true in estuarine environments that serve as valuable ecologic habitats, highly trafficked waterways, and recreational areas.

The method developed in this study uses a single-beam vertical-incidence echosounder to obtain full acoustic backscatter records. The waveform, defined in this study as the segment of the acoustic backscatter representative of the signal's first interaction with the bottom, is extracted and further analyzed. A statistical decomposition of the waveform's properties reveals spatial patterns in acoustic data that are related to the bottom composition. This method (similar to those used by Preston and Collins, 2000; Tsemahman *et al*, 1997; Amiri-Simkooei, 2011; Milligan *et al*, 1978; De *et al*, 2010, and others) removes subjective biases by using an empirical orthogonal function (EOF) to decompose waveform properties and objectively determine the significance of those properties. The results of the statistical decomposition are compared to measured mud fractions from bottom sediment samples, and used to model sediment properties in areas where only acoustic data has been collected. Further relationships between acoustic responses, bulk density, and porosity measurements are also considered.

Chapter 2

METHODS

Field

Acoustic Survey

A single-beam vertical-incidence echosounder survey of the Little Bay, New Hampshire (NH) (Figure 1), was conducted over 16 days in the winter of 2013 (12-15, 20-22, 25-26 February, and 11-15 and 26-27 March). The survey extended from the General Sullivan Bridge to Adam's Point. Survey times were focused around high tide during daylight hours to allow surveying of the very shallow mudflats surrounding much of the estuary. Survey lines were planned with 20 *m* spacing and run cross estuary. These lines were uploaded into Hypack, a hydrographic survey software, and used for navigation during the survey. A total of 360 prescribed cross channel lines were surveyed, a cumulative 383 *km*. The boat speed was kept at approximately 3 to 5 *knots* during data collection to allow for a relatively high along-track ping density (approximately 70 pings per meter). The high density of acoustic measurements allowed for more robust measurements of waveform properties during later analysis. Up to 3 conductivity-temperature-depth (CTD) casts were made each survey day using a YSI Cast-a-way CTD to determine the sound speed in the water column because water column variability associated with tidal currents. Owing to the well-mixed estuarine water at the time of collection, a simple linear correction was made to the sound speed by using an averaged sound speed from the nearest CTD cast (in time).

An additional survey using the same sampling procedure was conducted in spring 2014 in the Great Bay, New Hampshire (Figure 1). Four lines were surveyed in different areas of the bay, two with the same sonar settings used in the Little Bay and two with different transmit, gain, and pulse width settings.

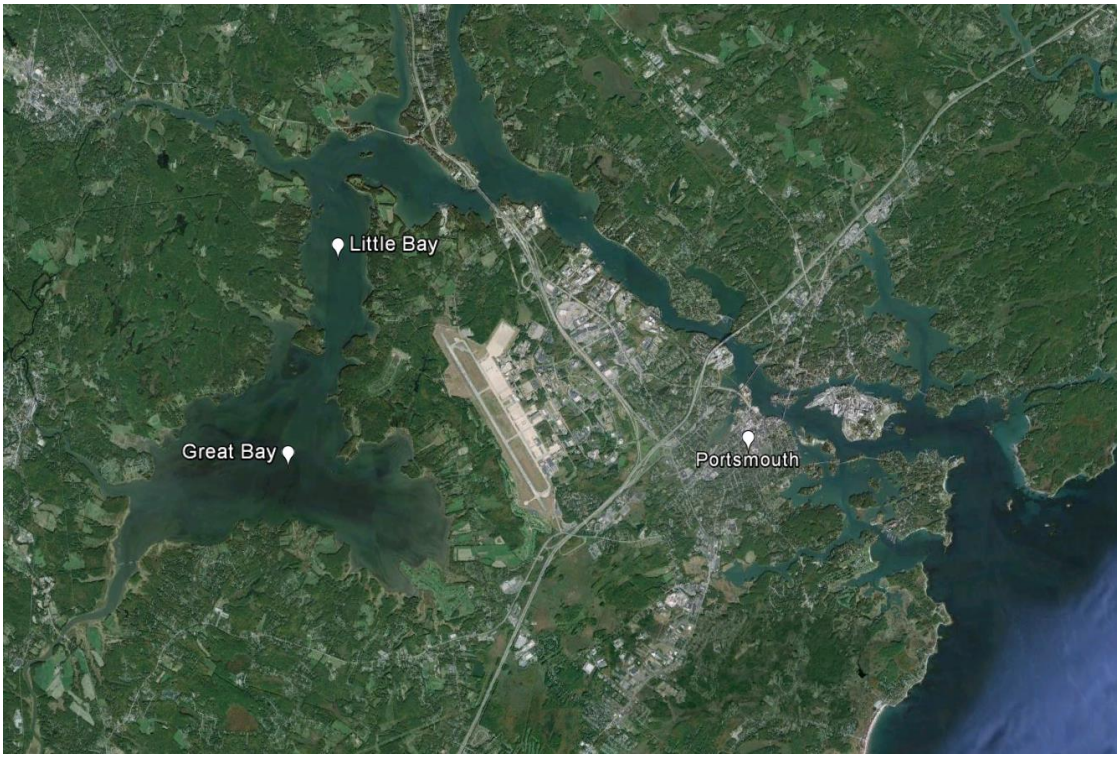

Figure 1 The Little Bay and Great Bay are part of the Great Bay Estuary system located inland of the town of Portsmouth in southern New Hampshire. (Image from Google Earth; imagery date: 10/9/2014)

Positioning

Echosounder positioning was obtained using a GPS receiver mounted to the top of the transducer pole with real time kinematic (RTK) corrections. RTK is a methods used to increase position precision by measured the phase of the measured satellite signal. Corrections were transmitted from a nearby Trimble 5700 GPS base station which was established through OPUS. Base stations were located at either the Great Bay Marina or near the boat launch at Adam's Point, depending on the proximity to the area being surveyed (Figure 22). RTK corrections were transmitted at 1 *s* intervals, resulting in 1-5 *cm* horizontal positioning accuracy throughout the survey based on the GPS uncertainty and the travel time of the acoustic signals. Depth was recorded relative to the WGS84 ellipsoid, converted to NAD83, and then shifted to the NAVD88 vertical datum using the National Geodetic Survey's 2003 Geoid Model. The total uncertainty resulting from the combined sonar depths and GPS vertical locations uncertainties resulted in an estimated 10 *cm* uncertainty.

Figure 2 GPS Base Station set up at the Great Bay Marine. The RTK antenna (right) transmitted correction from the GPS receiver (left) to the boat.

Echosounder and Transducer

The survey was conducted using an Odom CV2 echosounder system with an Airmar M108 duel-frequency (24 and 200 khz) transducer. The beam width of the 200 *kHz* signal was 4° and the beam width of the 24 *kHz* signal was 20°. The bandwidth of the 200 and 24 *kHz* signals was 100 *kHz* (Q = 2) and 3.2 *kHz* (Q = 7.5) and the pulse width 0.001 *ms* and 0.004 *ms*, respectively. The transducer was pole mounted to the starboard side of the R/V Galen J, a 22 *ft* open-cabin vessel with a 75 *hp* outboard motor (Figure 33). The bottom of the transducer was set at approximately 30 *cm* below the waterline with fore and aft straps attached to reduce vibrations of the transducer head. Ping rate was depth dependent, but averaged about 14 *Hz*. Full waveform 1600 sample returns (extending up to 30 *m* water depth) were recorded with the return intensity measured in uncalibrated millivolts. The echosounder steady-state gain was set so that the maximum intensity returns would not saturate, and then left constant for all days of the survey. A time variable gain based on 20log*R* (with *R* being range; Lurton, 2002) was also applied to account for spherical spreading loss of the acoustic pulse. In this study, acoustic absorption was ignored as it was assumed to be small in the shallow and calm Little Bay.

Figure 3 The R/V Galen J, a 22 foot open-cabin vessel used for surveying with the airmar transducer pole mounted to the starboard side with straps to stabilize the transducer head. A GPS receiver is mounted to the top of the transducer pole and a RTK receiver is mounted to the roof of the cabin.

Bottom Sampling

Grab Sampling

Bottom sediment samples were collected during 5 days in summer 2013 (26-27 June, and 1, 13, 14 August) using a gravity driven grab sampler (Figure 44). An initial total of 101 sample sites were sampled along 5 cross channel lines. The grab sampler was deployed at all sites, but sample sizes sufficient for analysis could not be collected at 29 sites. Insufficient samples were due to either negligible sediment retrieval or retrieval of one or a few rocks. Where little or no sediment could be collected, records were kept on the apparent bottom type. Sediment samples were stored in plastic bags and placed in a refrigerator upon returning to shore. An additional 19 sediment samples were collected in the spring of 2014 (1 and 22 April) along two new lines in areas of interest, one of which crosses the mouth of the Bellamy River where it flows into the

Little Bay. In total, there were 7 transects sampled for seabed sediment characteristics (Figure 55).

Figure 4 The gravity driven grab sampler used to collect surface sediment for grain size analysis

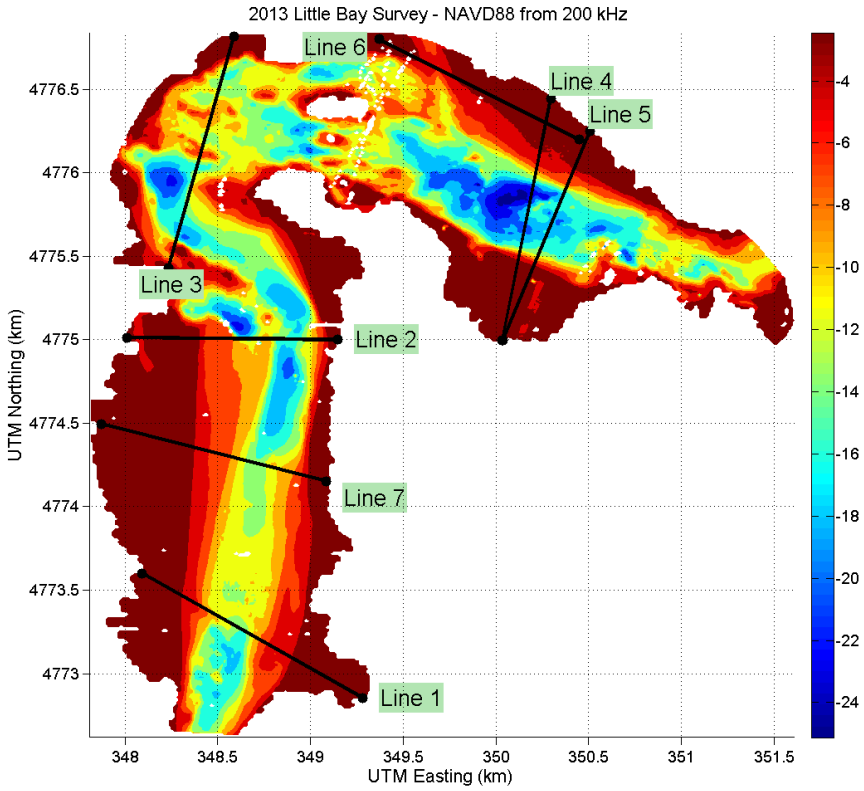

Figure 5 Sediment samples were collected along lines 1 through 5 in summer, 2014. Additional samples were collected along lines 6 and 7 in spring 2014.

Videography

To observe the *in situ* appearance of the bottom, particularly in areas where sediment samples could not be collected, an underwater video camera was lowered near the sediment sample sites. The underwater video camera collected images of the bottom with an associated GPS location at the surface (Appendix A) with an uncertainty on the order of a few meters given positioning uncertainty and bowing of the camera cable. The camera was supported above the bottom by a metal frame that included a marked 30 *cm* square in the camera's view (Figure 6). The video images revealed areas with exposed rocks and no mud. General large grained sediment sizes could also be qualitatively estimated using the known size gradation on the marked square of the frame.

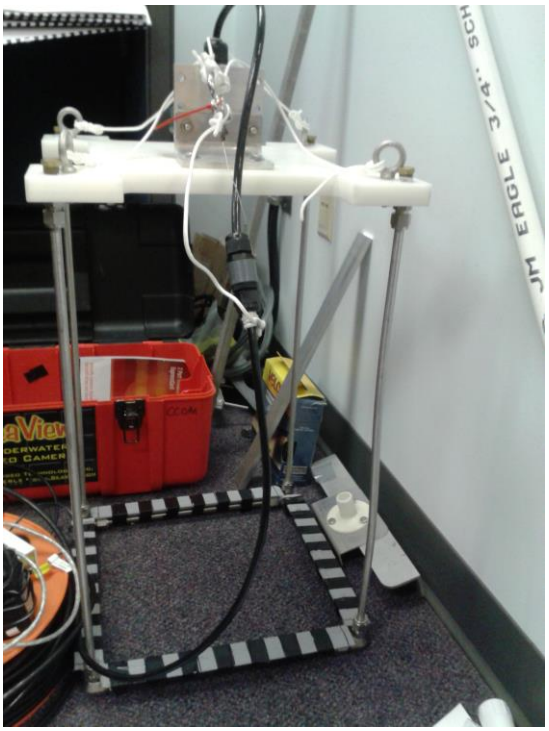

Figure 6 Underwater Video Camera at top with metal frame below to suspend camera above bottom.

Bulk Density Sampling

Bulk density measurements were made along line 4 which transects the main channel near the General Sullivan Bridge (Figure 77). To determine bulk density, a procedure was followed where two divers carefully inserted a 10.8 *cm* diameter tube into the sediment at approximate locations where previous grab samples were taken. The divers then capped the core, carefully

extracted it from the seabed, removed the top cap, inserted a plug beneath the sediment, and then re-capped the top of the core, at all times being careful to not disrupt the sediment-water interface. The core was then brought to the surface and extruded upward using a hydraulic press (Figure 88) until 2 *cm* was exposed. This volume of sediment (183.218 cm^3) was then carefully placed in a sealed bag, and later stored in a 4 *deg* C refrigerator. A 2 cm^3 subsample was removed from each sample to be used for sediment grain size analysis.

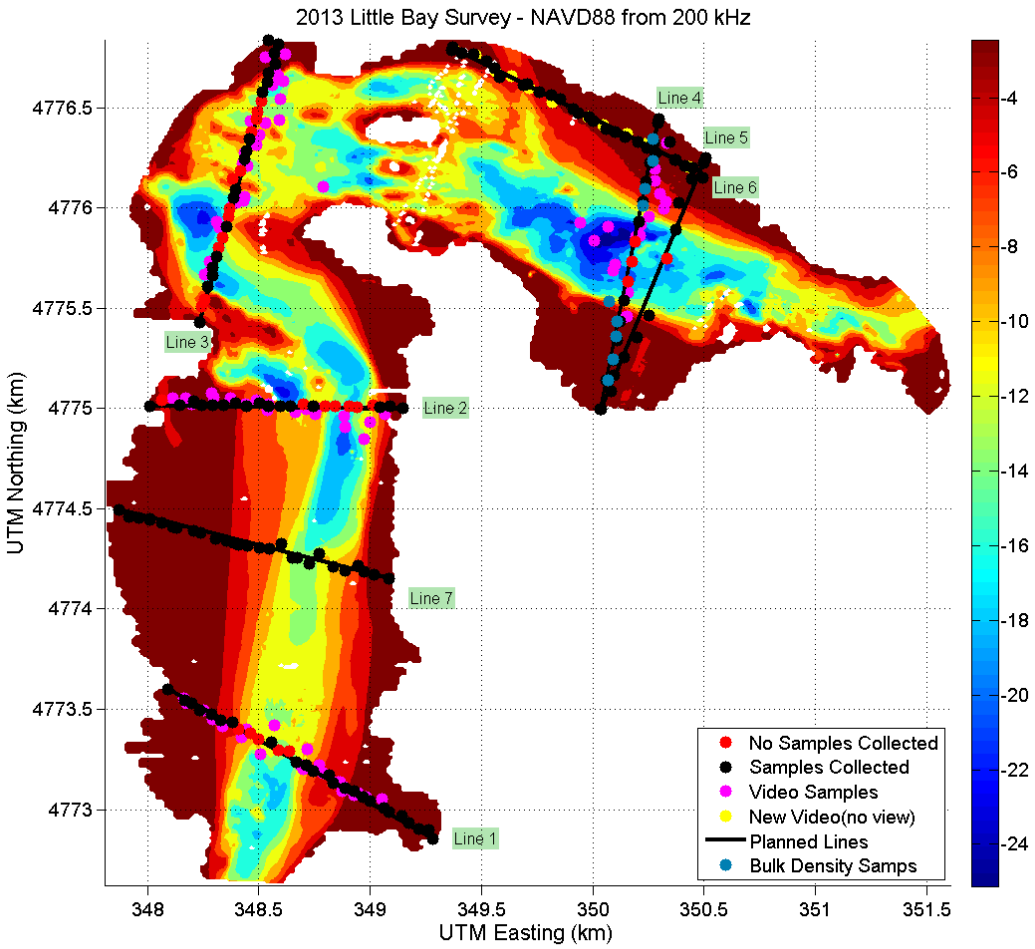

Figure 7 All sample locations including bottom samples, video samples, and bulk density samples.

Figure 8 An aluminum frame held a core in place while a hydraulic jack was used to slowly push the core upward until exactly 2 *cm* were exposed.

Laboratory Sediment Analysis

Bulk Density

In the laboratory bulk density analysis, the entirety of the remaining sample (181.218 cm^3) was placed in pre-weighed beakers, weighed, and then put in a 60-100 *deg* C oven for at least 24 hours to dry. Once dry, the samples were cooled to room temperature in a desiccator and reweighed. The difference in mass of the samples before and after drying was assumed to be entirely due to the removal of water. The mass of the wet sample per the volume of the sample is the wet bulk density, and the mass of the dried sample per the volume of the sample is the dry bulk density. A correction was made to the dry bulk density to account for the mass of salts in the pore water which remain in the samples after drying (Dadey, *et al*, 1992). The water

temperature and salinity at the time of sample collection was used to estimate a water density of 1.02 g/cm^3. The mass of water lost was divided by this density to determine the water volume contained within the original sample. Using the resulting water volume estimate, the porosity of each of the samples was determined by dividing the volume of water by the total volume of the sample. No gas appeared to be present in the sample, so it was assumed that all pore space had been filled with water at the time of collection.

Sediment Size Distributions

Sediment samples were analyzed for size distribution using a Malvern Mastersizer Laser Particle Size Analyzer (Figure 99) which emits a laser beam directed at a thin area of dispersed particle sample and measures the intensity of light scattered from the sample. It is limited to measuring maximum sized particles of 2 mm. The size analyzer produces an average size distribution based on 3 separate runs for each sample from which the percentage of sand and silt/clay (mud) was determined (Figure 10). A median sediment size (D50) was also determined by the particle size analyzer.

Figure 9 The Malvern Mastersizer laser diffraction size analyzer used to measure the size distribution of sediment samples.

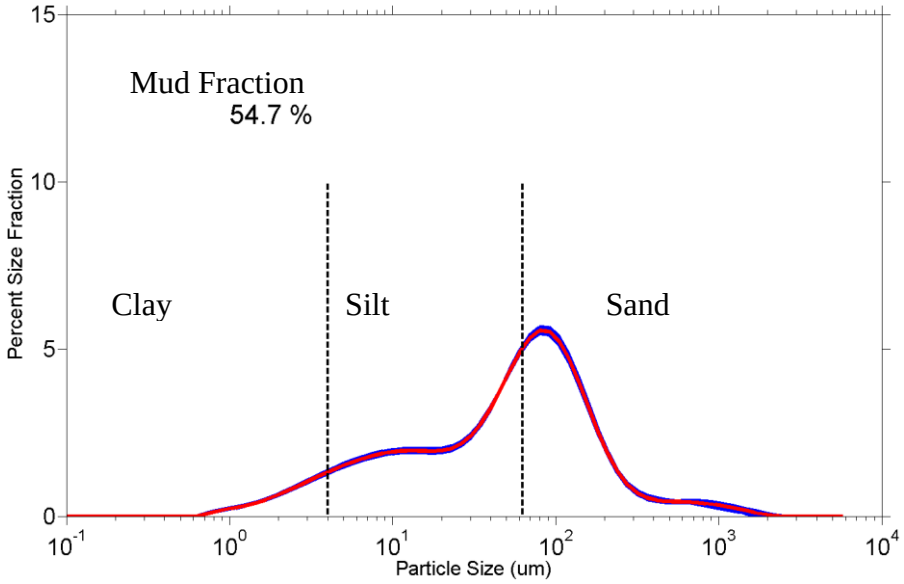

Figure 10 An example of a sediment size distribution with the measured mud fraction shown. Blue lines show the results from the 3 trials and red shows the average. The dashed lines show the threshold between clay and silt (4 μm; left) and silt and sand (62 μm; right)

Data Analysis

Acoustic Waveform Analysis

Sonar data and RTK-GPS GGA NMEA strings were recorded simultaneously in an ODOM *dso* file. The data from the *dso* files was parsed and the full returns were stored in new binary files along with ancillary sonar settings, position, and time information. Each full return was interrogated based on a median intensity threshold to find and extract the portion of the waveform representative of the first acoustic interaction with the bottom (similar to Dijkstra, 2000). Waveforms with erroneous depth or positions were filtered out using a 3 standard deviation filter. Groups of 2, 3, 5, 10, and 20 consecutive waveforms were averaged together and retained for later comparative analysis. Each isolated waveform was then analyzed to extract shape defining parameters: intensity maximum, waveform width, mean intensity, integrated total area, rise time, skewness, and kurtosis (Figure 111).

In this analysis, the maximum is defined as the highest measure of millivolts within the chosen waveform. The width describes the number of samples within the waveform (which

could also be expressed in time or distance once sound speed corrections were applied). The mean of the waveform is the mean amplitude (in *millivolts*) of the waveform. The integrated total is the integrated total of millivolts along the width of the waveform. The rise time of the waveform is the number of samples (or time) from the beginning of the waveform to the maximum value. The skewness and kurtosis describe how the waveform differs from that of a Gaussian distribution (Parrish *et al*., 2014 and Adams *et al*., 2011).

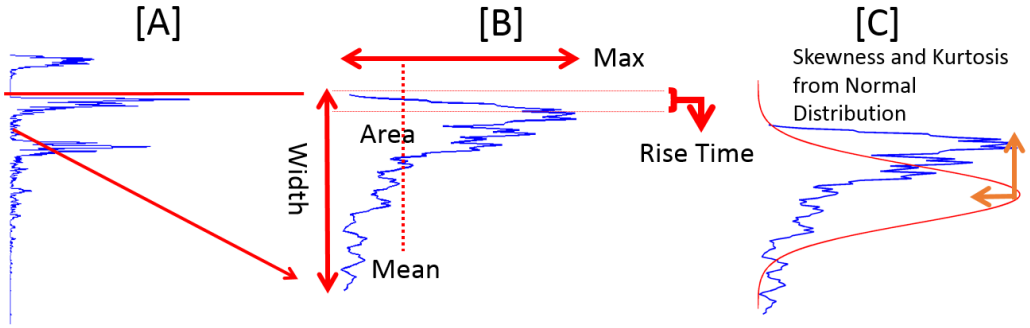

Figure 11 A shows an example of a full 1600 sample return. The original pulse noise, the first return and the second return can be seen. B and C show visual representations of the shape parameters that were extracted from each waveform.

Empirical Orthogonal Function Decomposition

An empirical orthogonal function, or EOF, is an eigenvector based decomposition of a data covariance matrix into separate orthogonal modes. Each mode accounts for a specific amount of the variance, with the first mode accounting for the most variance and each successive mode accounting for progressively less. It is important to note that in this decomposition each mode is constrained to be orthogonal to the other modes, making higher modes more difficult to physically interpret. The modes describe how a certain weighting of the original properties (described by the eigenvectors) varies spatially and is given by (Davis, 2002)

$$X_m(v) = \sum_{k=1\ to\ M} F_k(v) a_k(m) \qquad (1)$$

where $F_k(v)$ is the normalized EOF eigenfunction for mode k as a function of variable v, $a_k(m)$ is the spatial weighting of the k^{th} mode at position m, $X_m(v)$ is the observations of each variable v

at spatial position *m*, and *M* is the total number of EOFs (equal to the number of variables considered). The spatial variation (or weighting) of each EOF mode, $a_k(m)$, is given by

$$a_k(m) = \sum_{v=1\ to\ M} F_k(v) X_k(m) \qquad (2)$$

Waveform properties from all locations were normalized to their respective maximum value prior to decomposition so that each would have equal relative weight independent of their units. Water depth at each location was not included in this analysis. Because of orthogonally constraints, only the first mode was considered in this study.

Modeling Mud Fraction

The spatial values of the first mode were gridded at 10 by 10 *m* intervals and compared to the measured mud fractions at their sampling locations. A simple logarithmic curve was fit to the data. A logarithmic curve was also fit to the relationship between mud fraction and each individual property prior to EOF decomposition. The model can be used to predict mud faction in all areas where acoustic information was available.

Chapter 3

RESULTS

Depth measurements extracted from the full waveform analysis (and after sound speed corrections are applied) were interpolated onto a 10 *m* grid to create a near-continuous bathymetric map of the study area (Figure 122) that served as a base map to plan sediment sampling and interpretation of results.

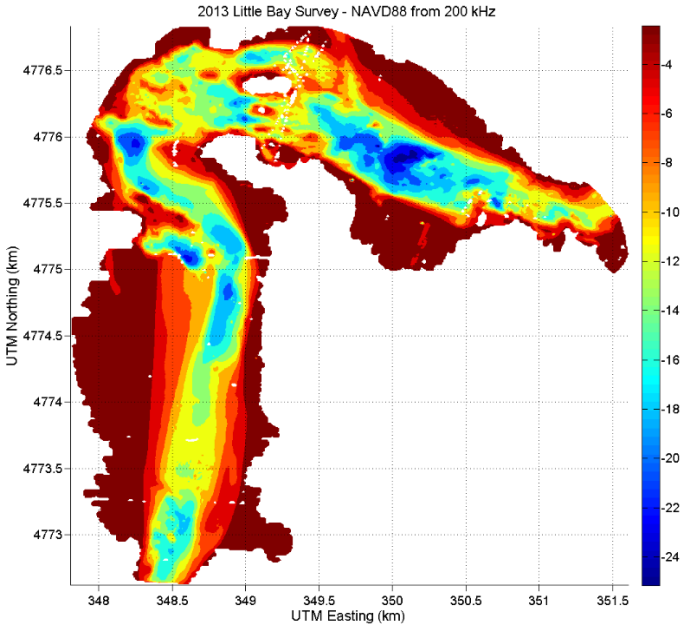

Figure 12 10×10 *m* gridded bathymetric map of the Little Bay, NH. The depth is from the 200 *kHz* signal and relative to the NAVD88 vertical datum. The axis of the map are in Northings and Eastings (*km*) in UTM Zone 19.

The waveform that was extracted from each ping was analyzed to determine the seven shape defining parameters, each separately plotted in Figure 133.

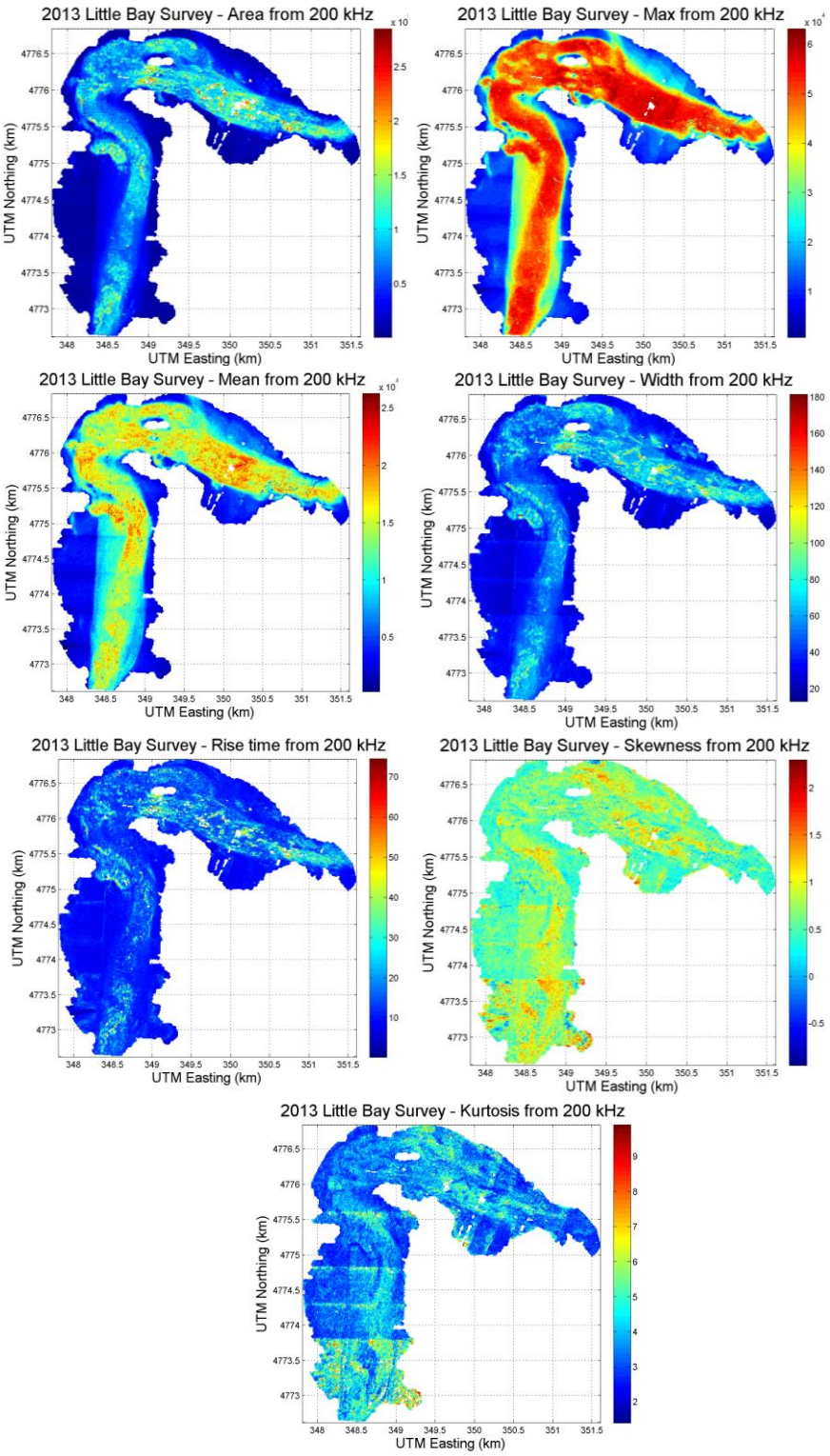

Figure 13 Spatial pattern of the observed distribution from the seven waveform parameters were extracted from each 200 *kHz* ping.

These parameters were decomposed into modes using EOF decomposition (Eq. 1 and 2). Each EOF mode has a normalized weighting corresponding to each variable (upper panels; Figure 144) and a spatial variation at each sonar sampling location in the Little Bay (lower panels; Figure 14). The skill of the first, second, and third modes is 91.1%, 5.98%, and 1.92% respectively. The highest contributor in the first EOF is waveform intensity maximum, and all the other waveform properties positively contribute to the spatial distribution of the variance. The middle panels (Figure 14) show the second mode where the skewness and kurtosis explain the majority of variance. In the following, only the first mode is considered owing to its overwhelming contribution to the variance and the orthogonality constraints on the remaining factors.

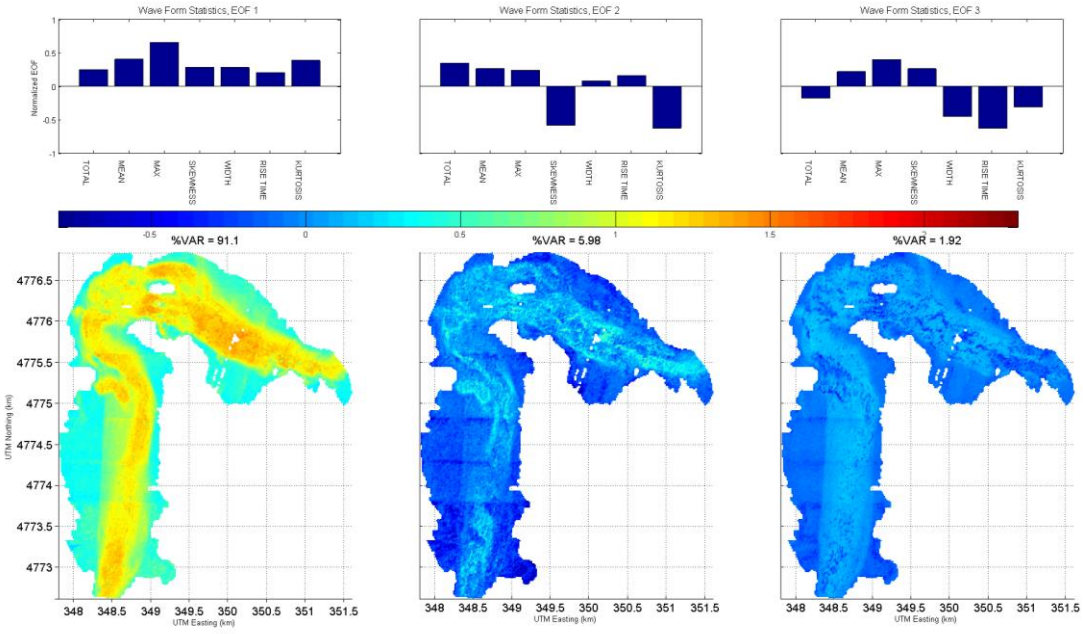

Figure 14 From left to right, the first 3 modes (of 7 total) from the EOF analysis explain 98% of the variance with the respective modes explaining 91.1, 5.98, and 1.92% of the variance. The first mode was used exclusively for further analysis.

Sediment size distributions were obtained from the Mastersizer laser diffraction particle size analyzer (Figure 155 and Appendix B). A mud fraction was obtained from each size distribution by summing the fraction of all size bins below 62 μm and divided by the total.

Although, some of the sediment samples showed evidence of a bimodal distribution in which one mode was primarily sand and the other mode was primarily mud, no further distinction is made to characterize the sediment composition.

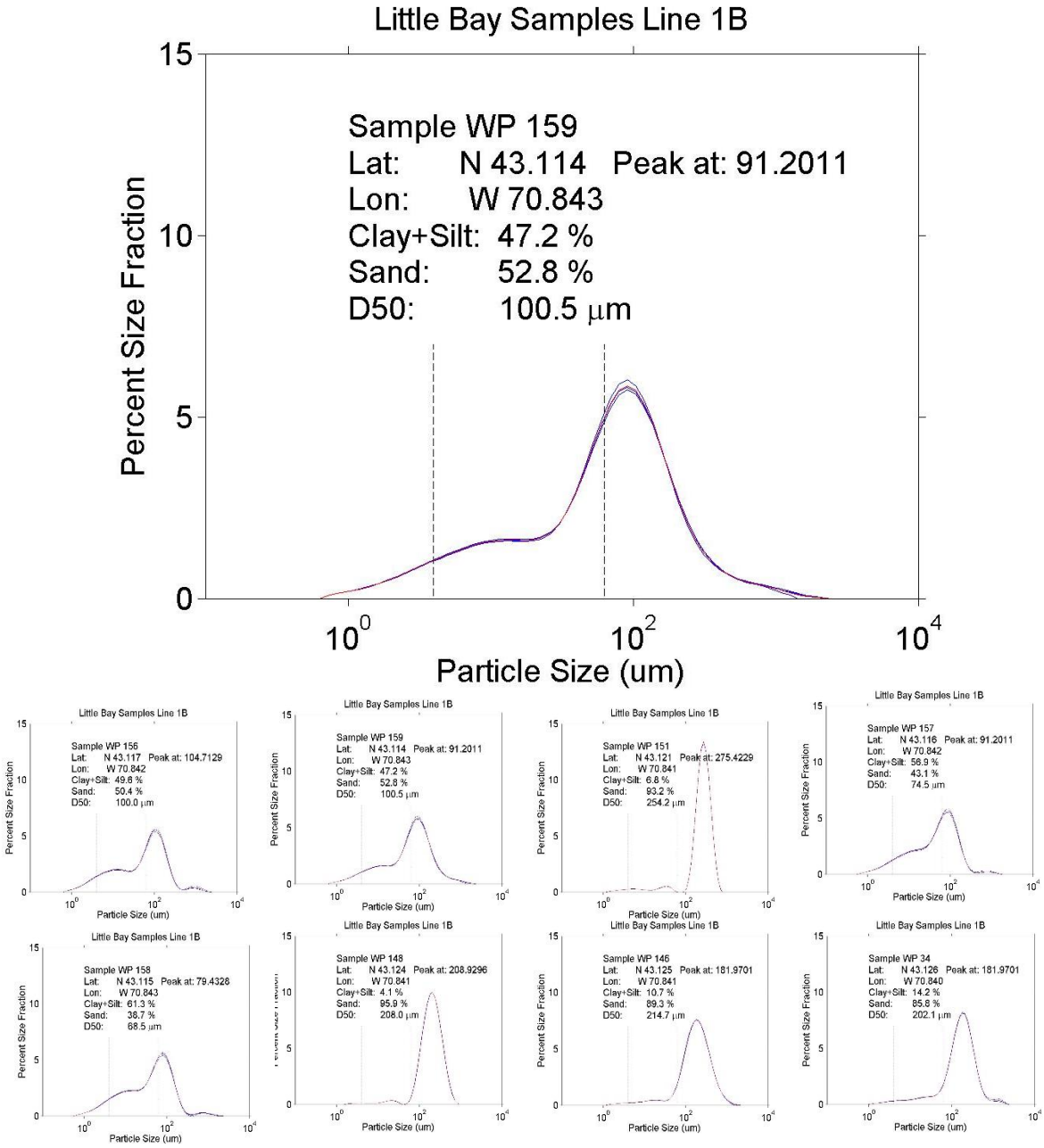

Figure 15 Size distribution of some select bottom samples from Line 1. The vertical lines in the graph represent the threshold between clay and silt (left) and silt and sand (left). The size distribution plots includes results from three separate measurements (blue) as well as an average of the three trials (red). For each sample, the percent clay and silt were combined to obtain a percent mud (a combination of the two size classes of sediment).

Figure 166 shows a comparison between the measured mud fractions and the spatial weighting of the first mode from the EOF analysis at the corresponding location. A simple logarithmic curve was fit to the data which explains approximately 43% percent of the variance of the data, and is given by the equation

$$MF(m)_{Predicted} = \frac{(\log a_k(m) - \alpha_1)}{\alpha_2} \qquad (3)$$

where α_1 and α_2 are the model curve coefficients and are equal to -0.1927 and -0.0109 respectively. The model fit was used to estimate surficial sediment mud fraction throughout the study area where acoustic data was available (Figure 177).

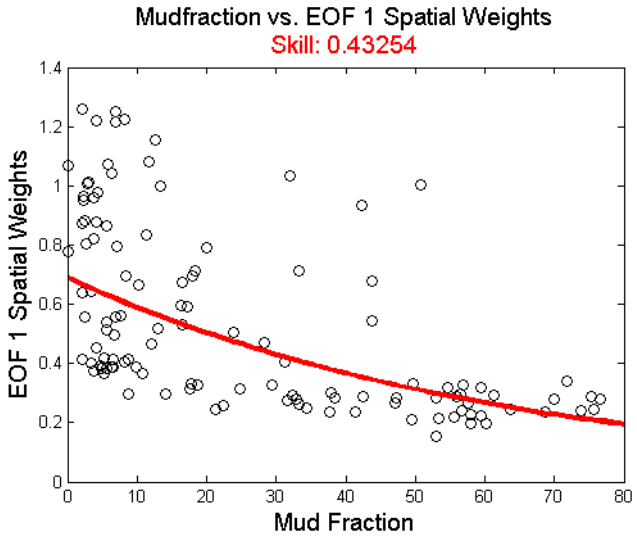

Figure 16 This figure shows a comparison of the measured mud fraction to the scaled spatial value of the first mode of the EOF analysis. The red line is a simple logarithmic curve that was fit to the data and has a skill of approximately 43%.

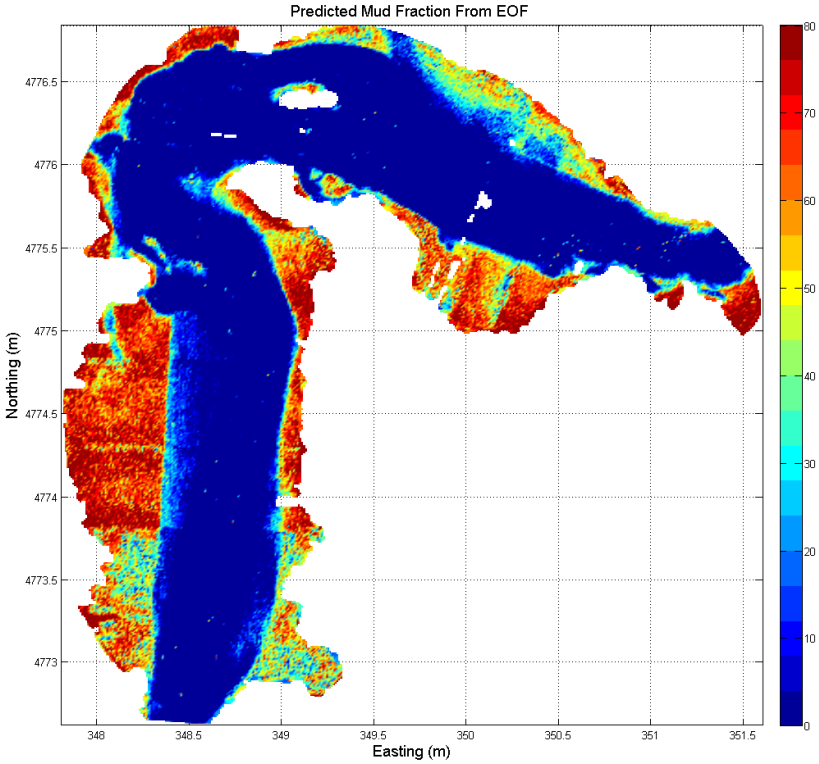

Figure 17 Predicted mud fraction in the Little Bay, NH using the model from the mud fraction-EOF comparison.

The spatial variability of the predicted muds using all sediment samples can be compared to observations along each of the four sampling lines separately. Figure 188 shows observed mud fractions as a function of distance along each transect line and in relation to the bathymetric profile. Also shown are the modeled predictions based on the individual waveform parameters independently, and the first EOF mode that objectively combines all the properties. This comparison suggests that – although the details of the variability are not precisely modeled – the gross spatial variability of the mud distribution is well represented by the EOF logarithmic model, and that the EOF model much better identifies the spatial characteristics of the spatial variation in mud fraction than the other properties independently.

It should be noted that the sediment samples near Bellamy River on the northern end of the Bay (lines 4, 5, and 6) show lower mud fraction than would be predicted by the simple logarithmic model. It may be that the bottom itself is smoother (less rough) in this region than in other regions of the Bay with similar material (Ferrini and Flood, 2006). This assertion, although

plausible, is not borne out with video samples of the region. It is clear that these data do not follow a similar pattern as the other data used in this report.

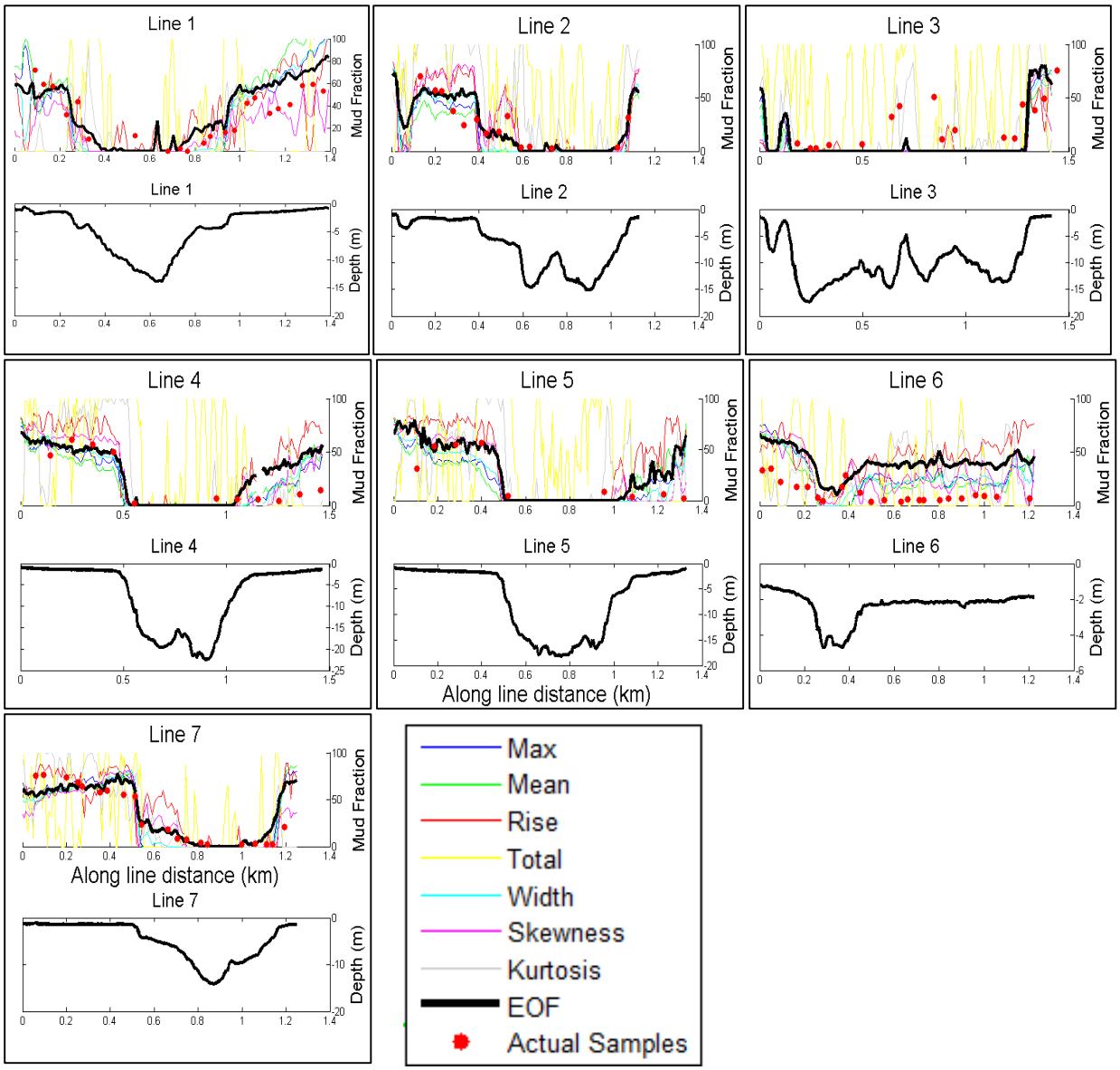

Figure 18 Predicted mud fraction along lines 1 through 7 with the prediction based on the EOF analysis shown by the thick black line. Depths profiles for each line are shown on the bottom.

Up to this point the relationship of the acoustic backscatter has been assumed to be only a function of the unconsolidated makeup of the surficial sediments. The mixture of grain sizes creates a variation in interstitial pore spaces that defines the porosity and bulk density of the

substrate, properties that are more directly related to the acoustic impedance that determines the nature of the acoustic backscatter properties. Bulk density (and hence porosity) was sampled along Line 4 from eight undisturbed diver-obtained core samples. Comparison of the wet bulk density and porosity determined from the upper 2 *cm* of the core and the acoustic backscatter for Line 4 is shown in (Figure 19). Two methods were used to calculate the wet bulk density. The 2 methods for calculating the wet bulk density (WBD) can be described by the equations:

$$\rho_b = \rho_w n + \rho_g(1-n) \qquad (4)$$

and

$$\rho_b = \frac{M_{wet}}{V_t} \qquad (5)$$

where ρ_b is the wet bulk density, M_{wet} is the wet sample mass, V_t is the sample volume, ρ_w is the density of water, ρ_g is the grain density (assumed to be quarts: 2.65 g/cm^3), and n is the porosity. In this study, the method shown by equation 4 is the preferred method for calculating bulk density since it calculates density independent of a measured volume which is believed to have high uncertainty. Instead, equation 4 uses porosity, determined using the fractional loss of water, a relative and more precise value. Some error is introduced by assuming homogeneously quartz sediment, but this error is relatively small compared to those associated with the volume measurements.

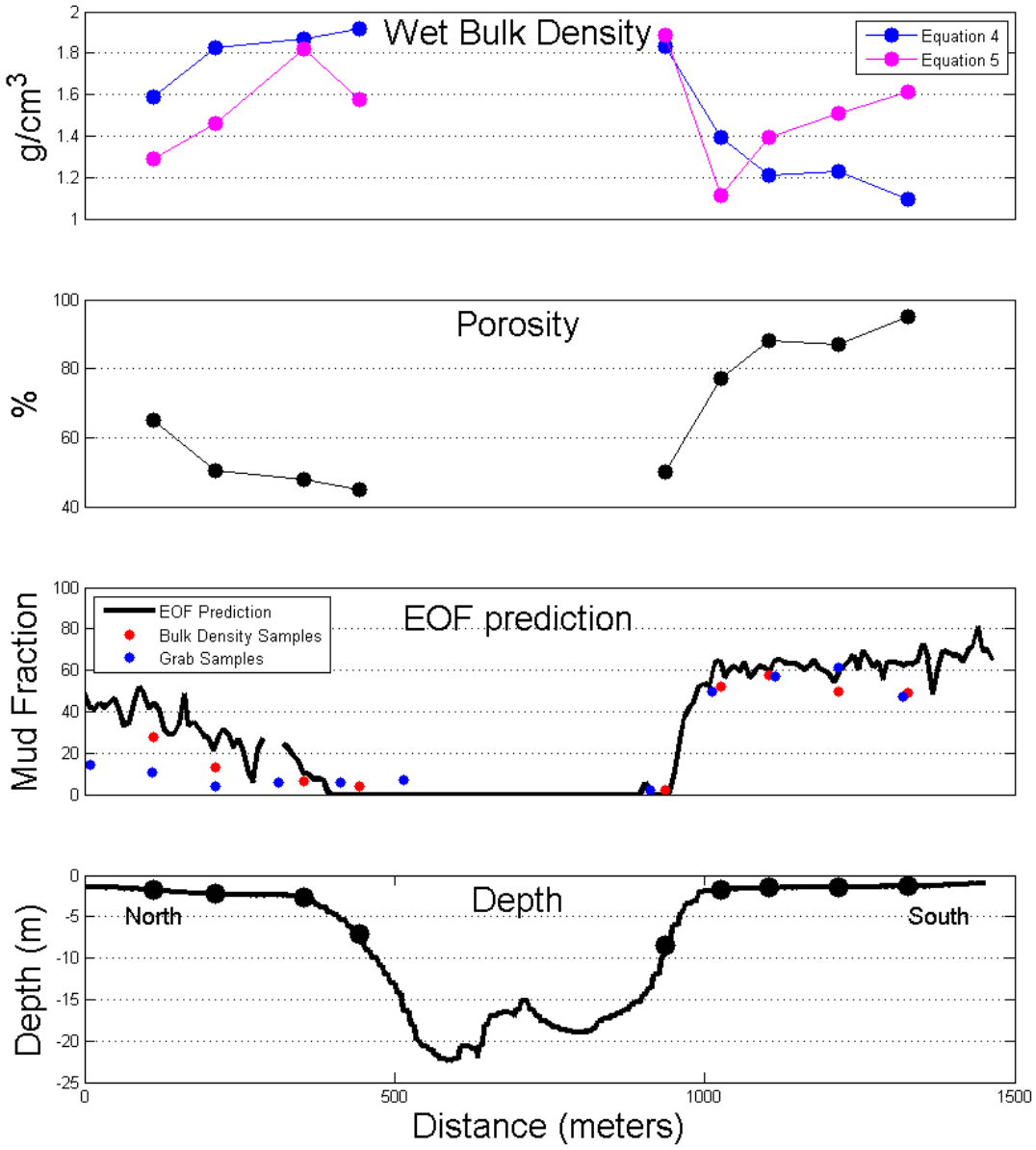

Figure 19 Bulk density was measured along line 4. The 4 panels from top to bottom show the measured wet bulk density, the calculated porosity, the measured and predicted mud factions (red dots show measured mud fractions from the bulk density sample and the blue dots show the measured mud fractions from prior sampling), and the depth along that line with the sample locations marked.

Acoustic data was collected along four lines in the Great Bay, NH (Figure 20) with the sonar settings described in the table below.

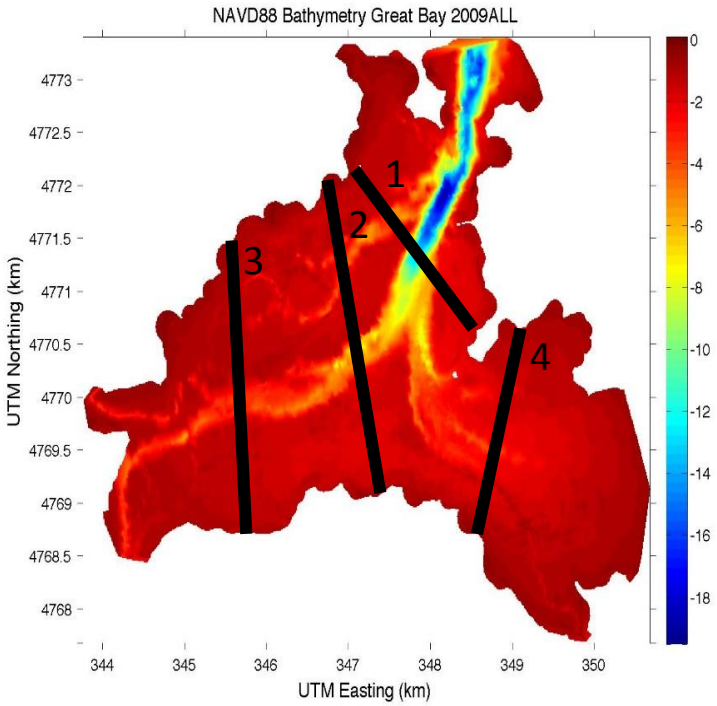

Sonar Setting	Lines 1 & 4 (same as LB)	Lines 2 & 3
Transmit Power:	11	4
Gain:	45	81
Pulse Width:	6	20

Figure 20 The locations of the 4 surveyed lines in the Great Bay, NH and their corresponding sonar settings relative to those used in the Little Bay.

The model created in the Little Bay was applied to the acoustic data from the Great Bay to predict mud fraction along the four sampled lines. Sediment samples were collected after the acoustic survey to test the accuracy of the applied model. Figure 21 shows the depth profiles, the predicted mud faction, and the measured mud fraction for lines 1 and 4 in the Great Bay which were collected using the same sonar settings used in the Little Bay survey. The RMS error of the predicted mud fraction is 11.9% for line 1 and 13.2% for line 4.

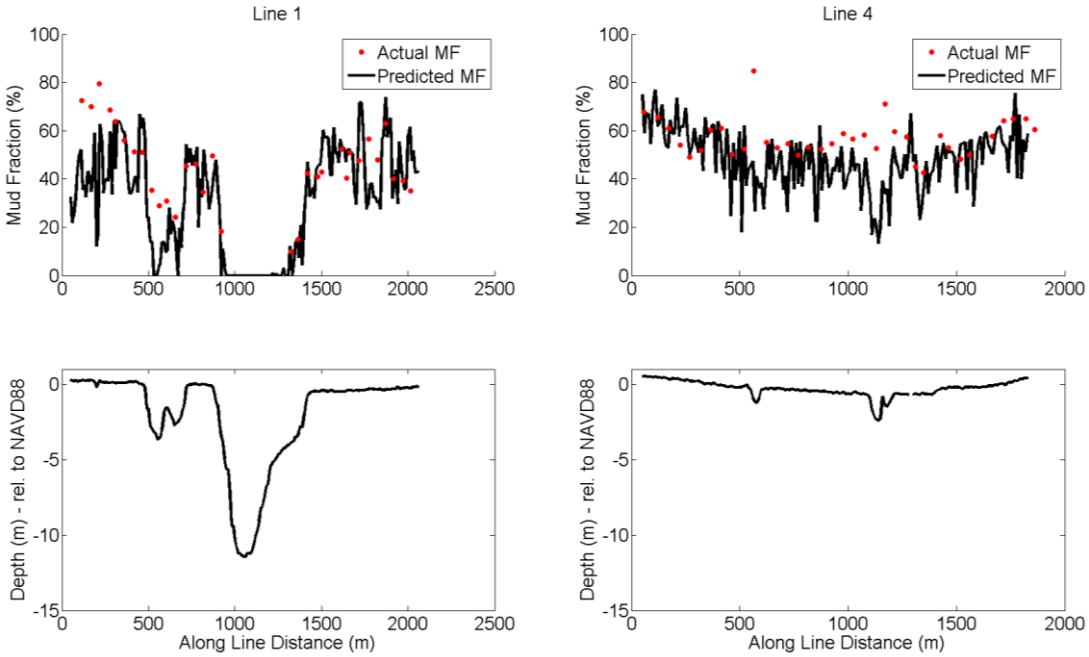

Figure 21 The predicted mud fraction for lines 1 and 4 is shown in black and the measured mud fraction is shown in red in the top panel for each line. The corresponding depth profile is shown below. The RMS error for lines 1 and 4 is 11.9% and 13.2 percent respectively.

The same methodology was applied to lines 2 and 3 in the Great Bay which were collected using different sonar settings. The depth profile, predicted mud fraction, and measured mud fraction for these lines are shown in Figure 22. The RMS error for the predicted mud fraction is 50.6% for line 2 and 57.9% for line 3.

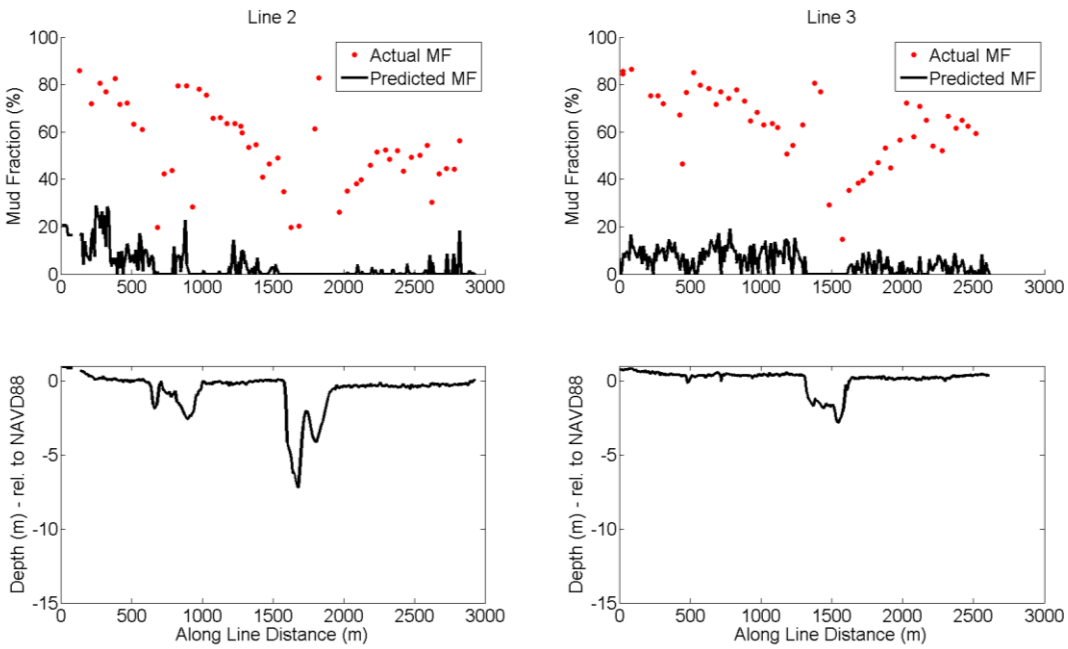

Figure 22 The predicted mud fraction for lines 2 and 3 is shown in black and the measured mud fraction is shown in red in the top panel for each line. The corresponding depth profile is shown below. The RMS error for lines 1 and 4 is 11.9% and 13.2 percent respectively.

Chapter 4

DISCUSSION

The results of the acoustic survey revealed the expected complicated bathymetry of the Little Bay, NH. The shallow banks of the estuary, which have been excluded from previous multi-beam surveys due to depth limitations, extend landward from the edges of the main channel at a relatively constant depth. In the shallows, ringing of the initial ping and reverberations from volume scattering of the 24 *kHz* signal distorted the first bottom return to such an extent that coherent waveform analysis was rendered unusable. However, the 200 *kHz* signal generally appeared qualitatively undistorted and was unsaturated in all parts of the bay, including both shallow and deep water regions (Figure 23).

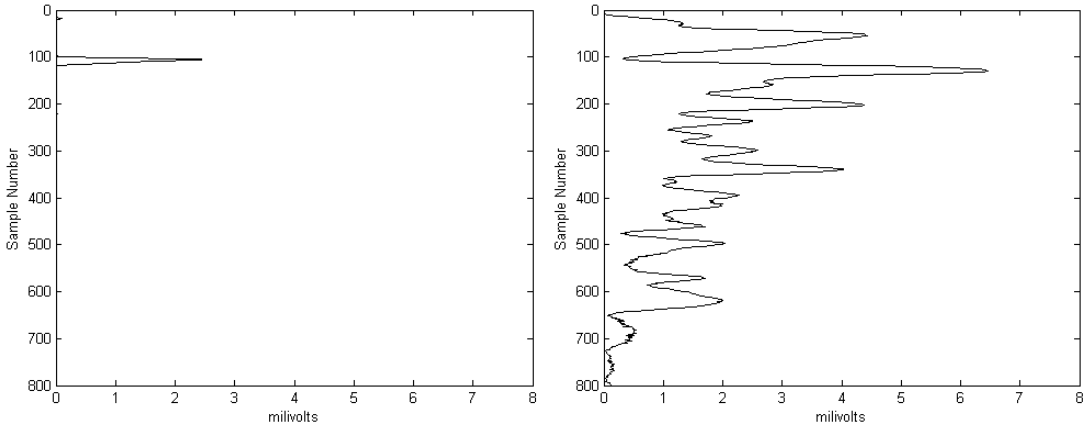

Figure 23 An example of a 200 *kHz* signal (left) and a 24 *kHz* signal (right) collected in a shallow dominantly mud area. Sample number, which can be converted to time and then depth, is on the y-axis. The magnitude of the measured return is shown on the x-axis. It can be seen that while the 200 *kHz* signal is a coherent and independent waveform, the 24 *kHz* signal is a fusion of numerous reflections and volume scattering which distorts the first return, making an accurate shape analysis difficult and introducing significant error.

Analysis of the 200 *kHz* waveforms provided an adequate measure of acoustic differences due to bottom composition. A range dependent gain was applied to the signals to remove the effects of spherical spreading (as previously discussed). Differences in absorption and volume scattering were assumed to be negligible. Szalay and Mcconnaughey (2002) suggested that slope can have an adverse effect on single beam seafloor classification work. In this study, slope did not seem to largely effect acoustic measurements, however, observed waveform widths suggests

that the steep slopes of the main channel may have effected some of the waveforms responses as illustrated in **Error! Reference source not found.**4. When a spreading acoustic signal reaches a loping bottom, it is reflected at varying depths, causing an increase in the width of the resulting measured waveform. A map showing the width of the measured waveforms suggests this type of spreading of the signal occurred along the sides of the main channel (Figure 25). The variance associated with these patterns does not appear to be present in the first mode of the EOF decomposition, but instead appears more prevalently in the second mode suggesting that slope effects are of higher order.

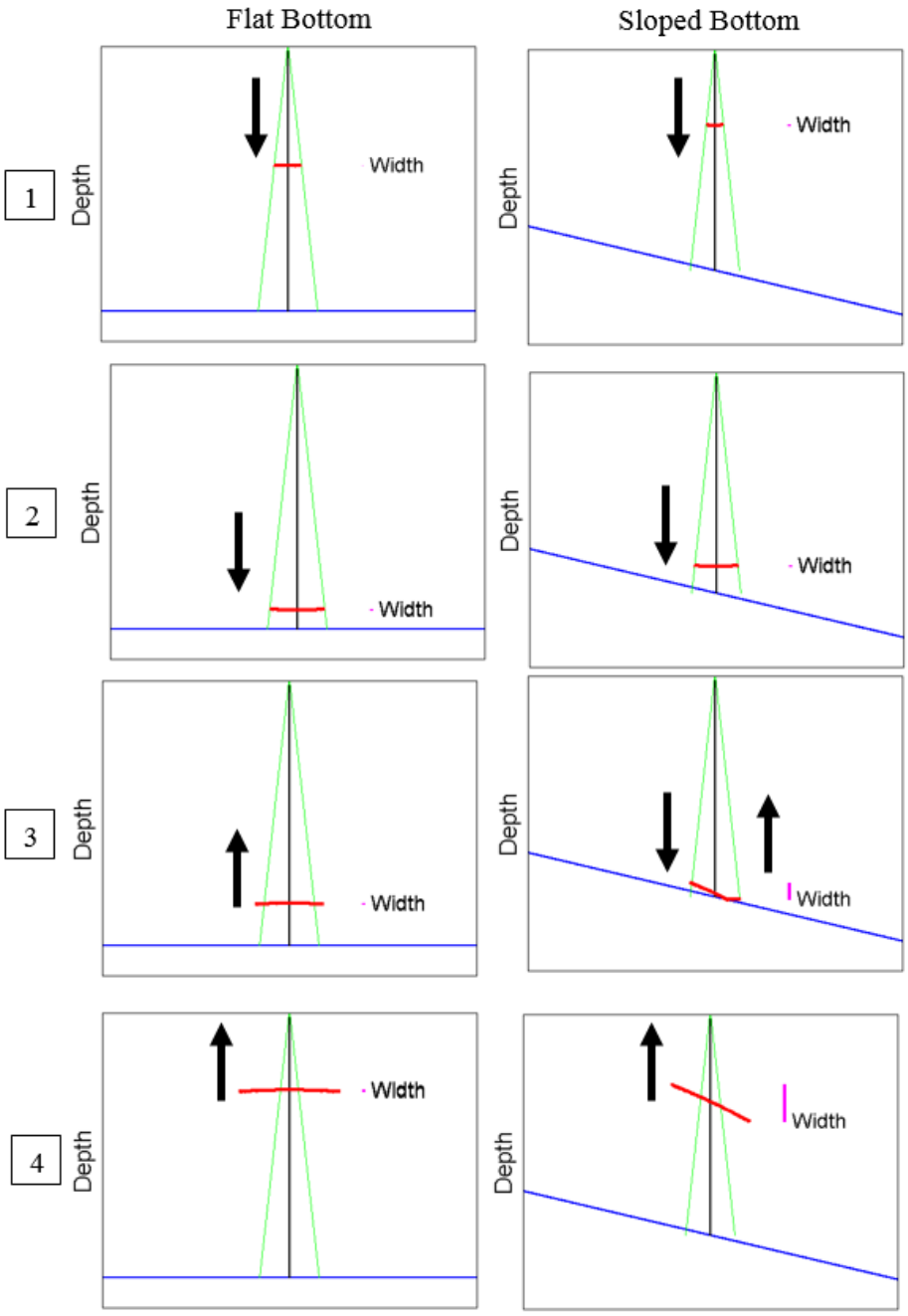

Figure 24 On the left, the four vertical pains show an example of an acoustic signal responding to a flat bottom. On the right, the four vertical pains show an example of an acoustic signal responding to a sloped bottom. In panel 3 of the sloped bottom example, it can be seen that the sloped bottom causes as spreading out of the return due to different ranges. This increases the width of the return waveform.

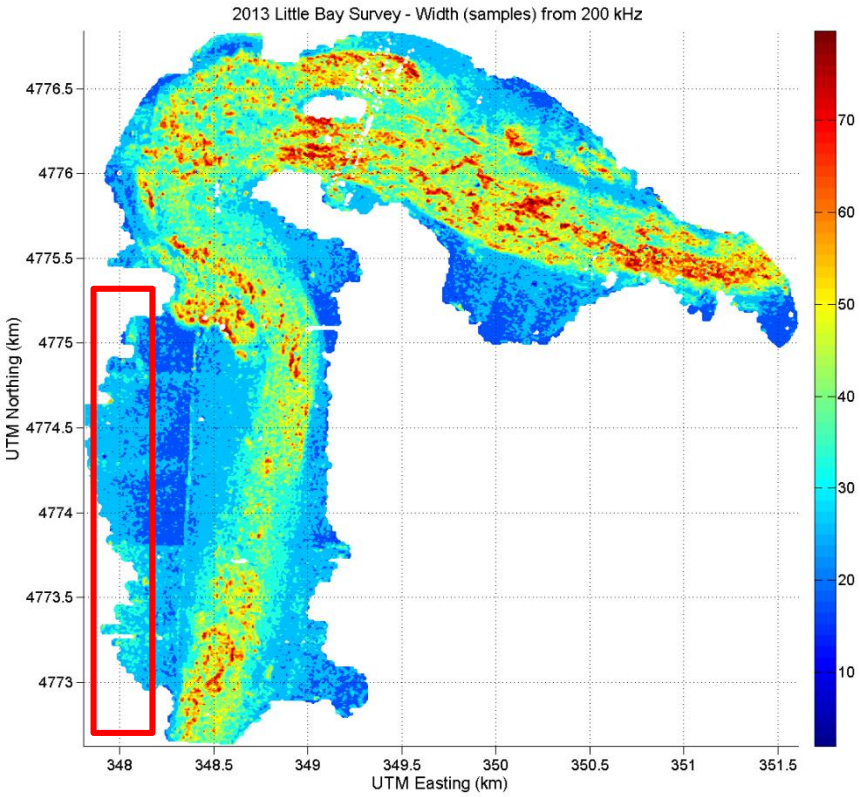

Figure 25 Along the steep bank (marked by the red box), a slight increase can be seen in the measured width of the waveform.

The first mode describes a 91% of the spatial variance of the different waveform properties (Figure 26). Differences in the weighting of the different waveform properties suggests there is a more coherent spatial distribution of variance for some properties (e.g., maximum intensity, mean intensity, and width) than there is for others, but that all properties contribute positively to the first mode. The model (Figure 16; Eq. 3) well estimates the spatial variation in mud fraction (Figures 17 and 18), except where the Bellamy river flows into the Little Bay and modifies the porosity of the sediment layers (and hence the impedance of the acoustic signal; Figure 19).

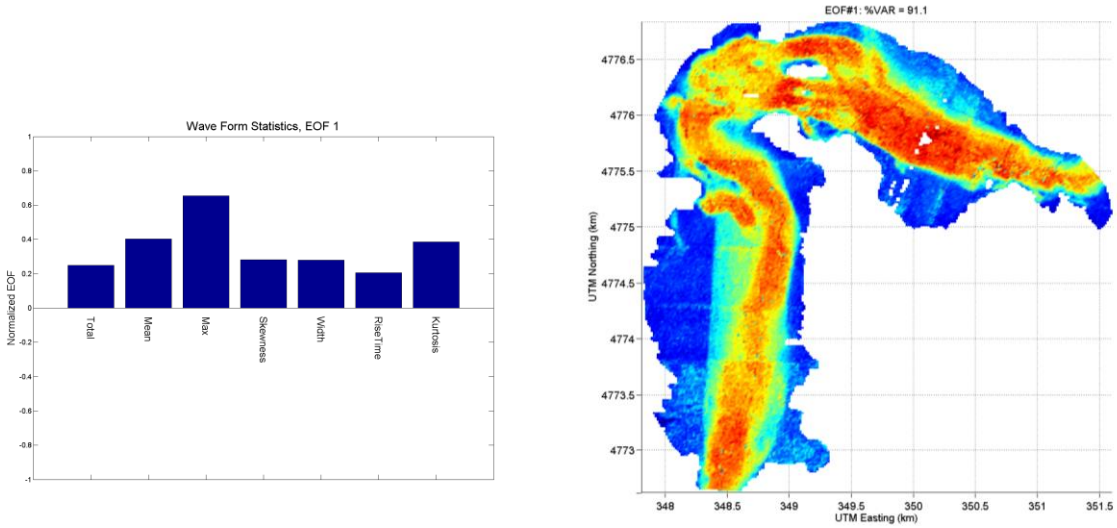

Figure 26 First mode from the EOF decomposition of the waveform properties. The waveform maximum, width, and mean contribute the most to the first mode, but all properties are important to the distribution of variance in this mode.

The spatial variation in the predicted mud fraction (Figure 17) based on the EOF model closely follows water depth variations (Figure 12). This is perhaps not surprising considering the effect of depth on tidal currents in the bay. During flood and ebb tides the currents in the deeper main channel are quite strong (up to several knots) and act to remove much of the unconsolidated sand, silt, and clay, leaving behind coarser gravel and rocks. These sediments are swept downstream and also transported laterally to the sides of the estuary where they settle out in the lower flows near the banks and over the mudflats.

However, since both depth and sediment type vary in similar patterns in many environments, it can be difficult to determine which factor is dominating the return acoustic signature. Two simple checks were done to insure that the acoustics were responding to sediment properties, not just depth variations. First, rise times were calculated to vary by just 3 or 4 samples based on depth variations alone, but instead varied more typically by 10 to 20 samples. Secondly, depth was plotted against the independent variables to see if they were totally correlated (Figure 27). Despite significant variability, no property showed a strict correlation to depth; the maximum shows this well. The maximum return increases with depth to about 12

meters depth but then varies little in areas where typically no sediment exists. There is practically no change in the maximum return in the deepest 10 meters of the surveyed area, demonstrating that the acoustic response is more correlated to sediment variations than to depth. This is supported by video work which shows a gradation in sediment time in shallower waters, but essentially no variation below 10 to 15 meters.

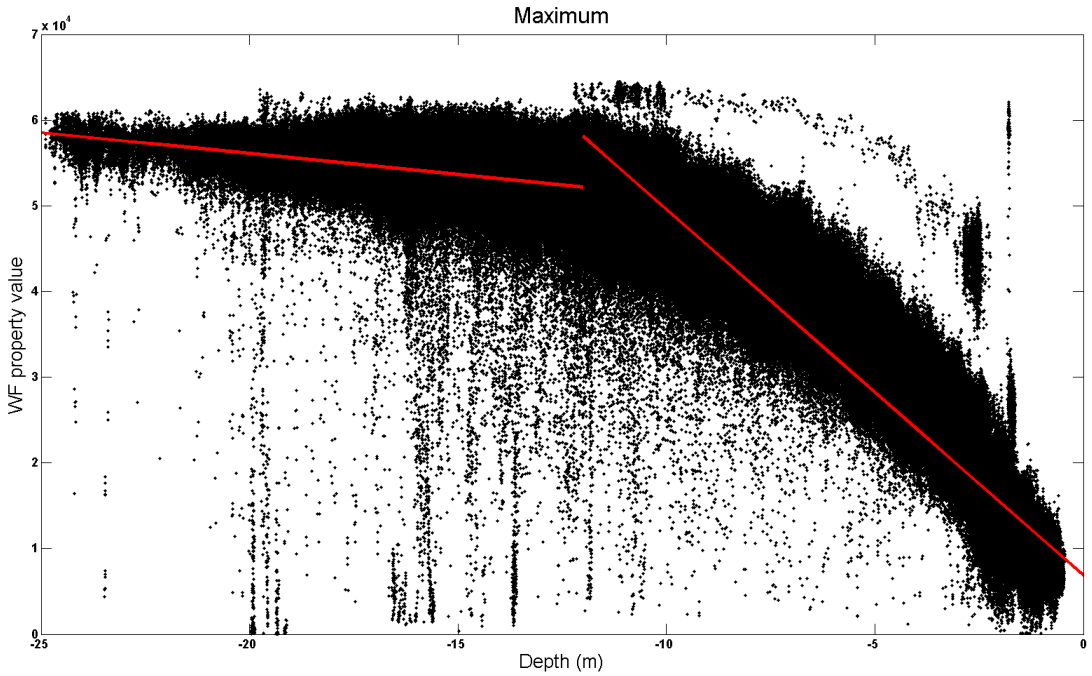

Figure 27 Individual maximum returns are plotted against their corresponding depth values. The red lines show a linearly fit line from 0 to 12 *m* and 12 to 25 *m* to demonstrate how the maximum response is not correlated to depth, particularly in the deeper areas of the estuary where most sediment has been windowed away and only rock remains, unvarying in the deepest 10 meters.

The model (Eq. 3) created using the first mode of the EOF decomposition can be used to directly estimate surficial mud fraction in the shallow and highly variable Little Bay, NH. There are strengths and weaknesses to this type of model. The model explains approximately 43 percent of the variance of the mud fraction measured from bottom samples. This skill may be lower than expected due to small scale variability and model resolution which limits the model

from predicting mud fractions at single point locations such as those measured with the bottom sampling methods. There are also uncertainties associated with the estimated location where the sediment samples were collected due to tidal currents, the motion of the vessel relative to the currents and ground, and the inaccuracies in the hand-held (autonomous) GPS used to record the sample location (schematically shown in Figure 288). Often the grab sampler would be moved away from the recorded location by tidal currents present in the little bay and there was visible bowing of the line during bottom sampling and drop camera work. GPS locations were recorded at the boat's position creating a discrepancy between the measured and actual location of samples, potentially contributing to errors associated with the model. Sampling position uncertainties are difficult to quantify are likely on the order of 10 meters.

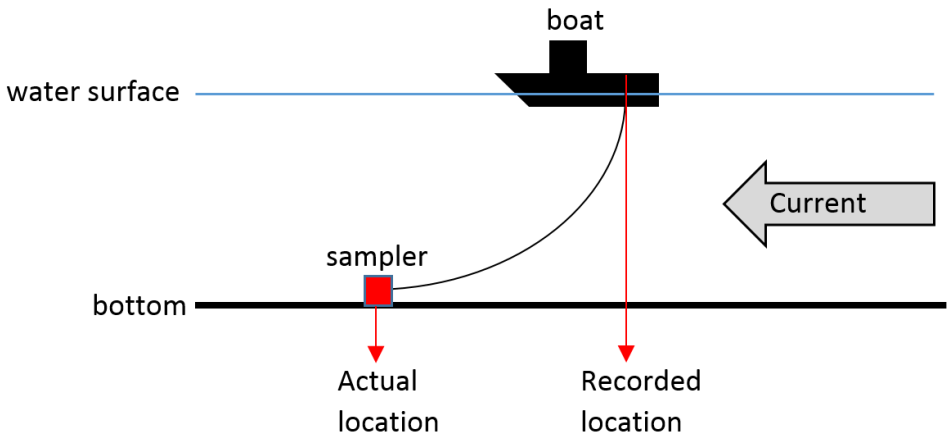

Figure 28 Schematic showing the displacement of the grab sampler relative to the vessel location and the recorded position due to tidal currents.

Model results are well suited to estimate an average mud fraction within each 10 by 10 *m* cell where small scale variations are smoothed out. While this decreases the resolution of the model, it also reduces the effect of small scale variability and the errors associated with sampling locations. There were some variations in bottom type observed in the video data over only a few meters. These variations were sometimes due to biological material and sometimes due to an actual change in sediment composition. In some of these images, plant growth (Figure 29) changes the character of the bottom, despite a similar sediment type observed nearby.

Figure 29 Example video images showing aquatic plants (top image) within a couple meters of bare sediment areas (bottom image) but with similar visual bed characteristics.

On a larger scale, the model successfully predicts spatial patterns in the mud fraction, particularly the high mud fractions on the flats and decreased mud fraction nearing the main channel. These types of predictions are useful for estimates of nutrient fluxes and potential habitats which frequently use more robust measures of sediment type such as the dominant sediment component (e.g. sand or mud) (Dyer, 1994 and Sakamaki, 2006) (Figure 30).

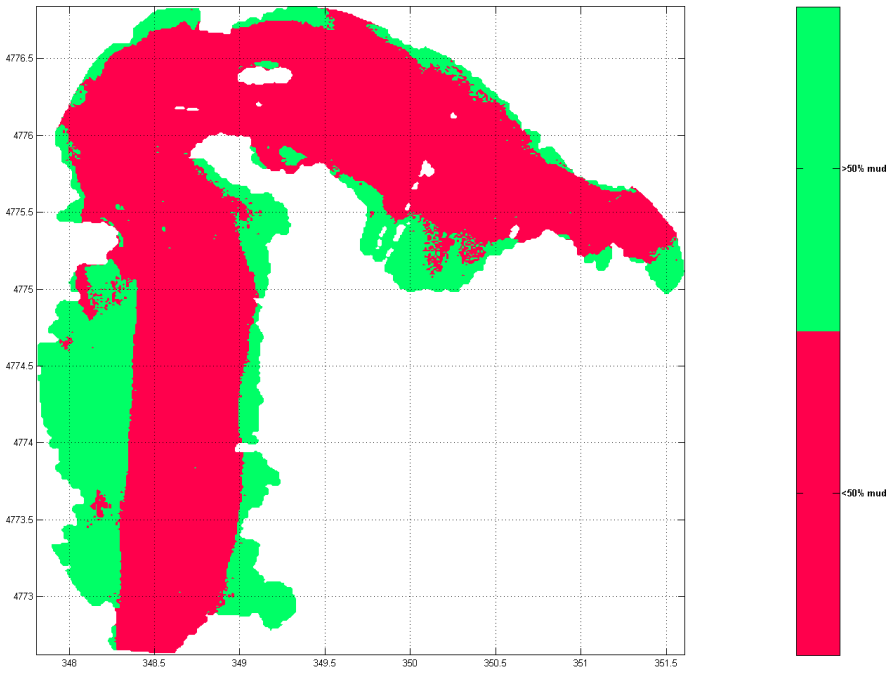

Figure 30 Modeled mud fraction partitioned into areas exceeding a 50% threshold (green) and areas below that threshold (red).

A potential weakness of this model is the direct relationship formed between mud fraction and the acoustic response. Mud fraction is a valuable geologic property of sediment that can be used in numerous fields of study, but there is not a well-defined direct relationship between mud fraction and acoustic backscatter which can be more directly related to the acoustic impedance of the target (Kinsler, 2000). Sediment size distribution is one property of the sediment that contributes to the impedance of the acoustic return, and in this study well predicts the spatial distribution of the mud about the bay. However, the compactness and roughness of the surficial sediments can greatly affect the acoustic response. Observations of bulk density along line 4 show large variations in bulk density and porosity between the northern and southern banks (Figure 19).

Bulk density measurements fit the data from the grain size analysis; there is sandier and consequently denser sediment on the northern bank than the southern bank. The porosity is also

notably lower on the northern bank. This suggests that the Bellamy River may be a source of sandy sediment which rapidly settles onto the relatively shallow Northern bank once the fluvial input reaches the less constricted bay environment. Previous work (LeBlanc *et al.*, 1992) has shown a strong inverse relationship between porosity and acoustic impedance and a strong positive relationship between seafloor density and acoustic impedance. Variations in porosity can result from both variations in grain size distribution and from the compactness of the surficial sediments. Following the relationship described by LeBlanc *et* al (1992), it is understood that while the increased porosity on the Northern bank decreases the acoustic impedance and reflectivity of that sediment, the increased density of the sediment on that bank has opposing effects on the acoustic response. The acoustic properties consequently only partially represent the variation in sediment type. It is clear that the relationship between grain size, porosity, and wet bulk density is complex and not fully captured by the measured acoustic properties. The final mud fraction prediction from acoustic properties is thus distorted by the porosity and density anomalies on the northern bank. The sandy sediment near the Bellamy river mouth could not be fully differentiated from more muddy sediment which produces similar acoustic properties (Figure 31).

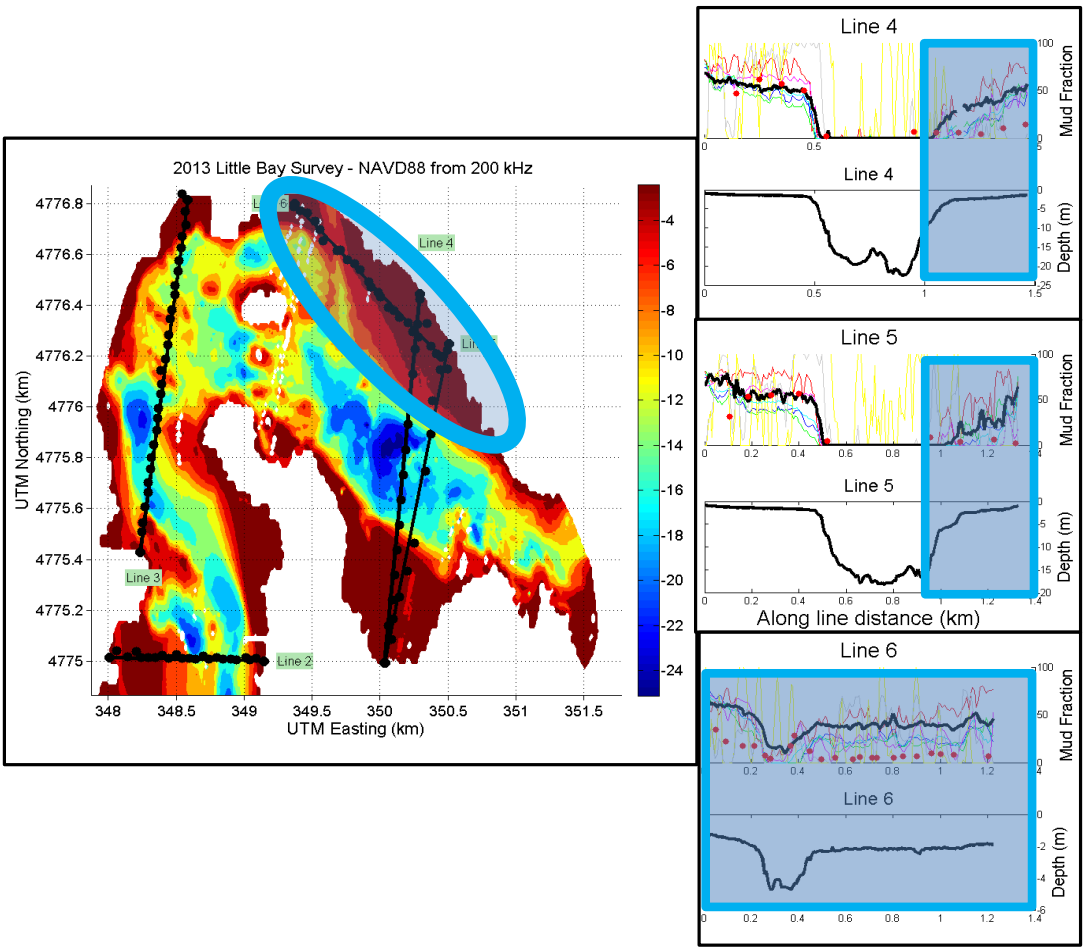

Figure 31 The modeled mud fraction from the EOF decomposition (thick black in cross sectional plots on right) predicts a higher mud fraction on the shallow bank near the Bellamy River mouth than actually exists. The area within the blue circle correlates to the cross section areas marked by blue squares.

It is also worth considering the possibility of temporal variation in surficial sediment in this area due to fluvial currents sediment inputs. Differences in mud fraction measurements between the initial grab samples and the bulk density samples suggests a possible increase in mud fraction on this northern bank during the intervening time period. It should then be considered plausible that the surficial sediment composition could have also varied in this area during the period between acoustic sampling and grab sampling. To eliminate the uncertainties

arising from temporal variability of the sediment composition, samples would need to be collected during the acoustic survey.

Selectively eliminating sediment samples from the area near the mouth of the Bellamy River increases the skill of the model to 61% (Figure 3232). In this newly fit line, α_1 = -0.13917 and α_1 = -0.021526. However, using the current analytical techniques and without consideration of sediment samples, this area appears acoustically similar to other areas and cannot be differentiated from other less sandy areas without additional information.

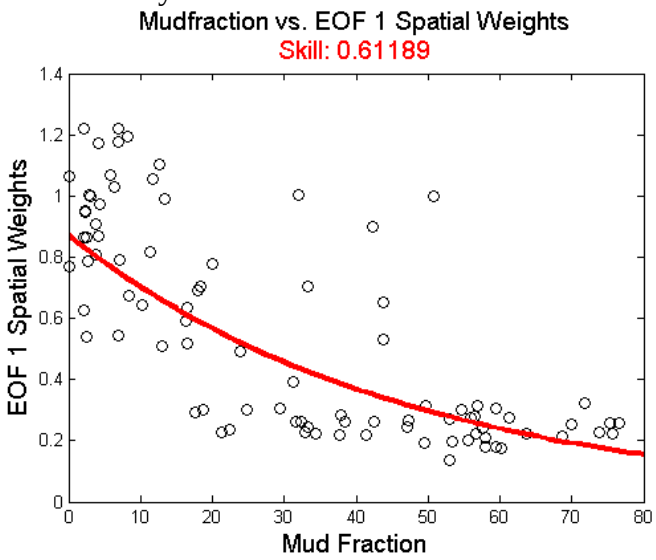

Figure 32 A curve fit to mud fraction and EOF data excluding data points from near the Bellamy River mouth. The skill of the model is increased to 61%.

There were multiple advantages to using this methodology and model for predicting mud fraction in the Little Bay which can hopefully be extended to other shallow water environments using combined acoustic and sediment sampling. The 10 *m* gridded model provides a substantially more comprehensive and higher resolution map of mud fraction than any direct sampling method, and in far less time both in the field and in the lab. The process additionally produces a bathymetric map for the area, another important tool for most scientific studies.

The model developed in the Little Bay was tested by applying it to a new area, the Great Bay, NH. Of the four lines surveyed, two were collected using intentionally varied sonar settings to explore the models robustness to changes in the sonar's transmit power, gain, and pulse width.

The Great Bay is connected to the Little Bay, but differs in fluvial inputs, depth, plant growth, and exposure to air. The Great Bay is generally very shallow with significant portions of the bay exposed during low tide. Increased eel grass growth was observed in several areas of the Great Bay. The main channels of the Great Bay are deeper than the surrounding mud flats, but are still significantly shallower than the main channel of the Little Bay.

The predicted mud fraction along lines 1 and 4, those collected using the same sonar settings used in the Little Bay, showed a strong correlation to the measured mud fractions. There was an increase in the variability of the predicted mud fraction relative that found in the Little Bay, but the model was still quite accurate with RMS errors just over 10% for these lines. Variations in mud fraction relating to the currents in the main channels were generally well captured by the model.

Predictions for lines 2 and 3 were less accurate. RMS errors surpassing 50% suggest that by varying the sonar setting, the original model was rendered obsolete. Therefore, for this particular model, the sonar and sonar settings must be kept the same as those used in the Little Bay. Fortunately, the sonar used is of high quality (Q=1) and the optimal sonar settings for most shallow water environments were used.

Chapter 5

CONCLUSIONS

Empirical Orthogonal Functions were utilized as an objective method to determine patterns of spatial variability from an ensemble of 7 different properties of acoustic waveforms. The first EOF was compared with measured mud fractions and provided a means to objectively estimate the spatial distribution of surficial mud fractions in the Little Bay from acoustic backscatter properties. This method increases both the coverage and resolution of mud fraction measurements compared to sediment sampling techniques. The model's skill varied based on waveform properties and samples included in the analysis, ranging from 43 to 61%. The skills of the modes were subject to the direct comparison of smoothed acoustic responses with discrete samples of mud fractions, and were therefore subject to an inherent uncertainty associated with small scale variability not quantified. Still, applying the model to acoustic data collected in a new area with the same sonar and sonar settings showed promising results. The RMS error of the predicted mud fraction using the Little Bay model fell below 15% for the two surveyed lines in the Great Bay.

In general, EOF mode one spatial variation based on 7 acoustic waveform properties can be used to estimate surficial mud fraction on spatial grid scales of order 10 *m*. Finer scale resolution is not easily modeled owing to the uncertainty in the sediment grain size sampling locations and the unresolved small scale sediment variability. Sediment characteristics considered in this study are focused mainly on surficial mud fractions, with some consideration of acoustic response to sediment compactness quantified with observations of bulk density and porosity. Results from the bulk density work were encouraging, but further work is needed on a broader scale, a difficult task considering the laborious efforts required to obtain undisturbed sediment cores over larger scales. Recent advancements in sediment load strength obtained with easily (and rapidly) deployed (from surface vessels) seabed penetrometers (Stark *et al*., 2010) would be particularly useful in comparing to both surficial sediment grain size distributions and bulk density.

Methods for remote and objective estimation of seafloor sediment properties are important to aiding further scientific research and policy decisions. Remote acoustic methods for determining sediment properties are advantageous compared to traditional methods in terms of

speed and spatial coverage. Whereas specific measurements of sediment properties are needed at a specific points, sample collection and laboratory work are still preferred, but where general predictions over a large area will suffice, remote methods are becoming favorable. Remote acoustic measurements of surficial seafloor sediment properties looks to be a promising path for providing scientists and policy makers with the necessary information to make more educated decisions.

REFERENCES

Adams, T., Beets, P., & Parrish, C. E. (2011). "Another dimension from LiDAR–Obtaining foliage density from full waveform data". In *SilviLaser Conference Proceedings*.

Airoldi L., Abbiati M., Beck M. W., Hawkins S.J., Jonsson P.R., Martin D., Moschella P. S., Sundelöf A., Thompson R. C., Åberg P. (2005) An ecological perspective on the deployment and design of low-crested and other hard coastal defense structures. *Coastal Engineering* (Amsterdam). 52(10), 1073. doi: 10.1016/j.coastaleng.2005.09.007

Alexandrou, D., & Pantzartzis, D. (1993). A methodology for acoustic seafloor classification. *IEEE Journal of Oceanic Engineering*, *18*(2), 81–86. doi:10.1109/48.219527

Amiri-simkooei, A. R., Snellen, M., & Simons, D. G. (2011). Principal Component Analysis of Single-Beam Echo-Sounder Signal Features for Seafloor Classification, *36*(2), 259–272.

Anderson, A. L. (1992, January). Remote acoustic characterization of the seafloor including gassy and hydrated sediment regions. In *The Second International Offshore and Polar Engineering Conference*. International Society of Offshore and Polar Engineers.

Atema, J., & Stenzler, D. (1977). Alarm substance of the marine mud snail, Nassarius obsoletus: biological characterization and possible evolution. *Journal of Chemical Ecology*, *3*(2), 173-187.

Anderson, J. T., Holliday, D. Van, Kloser, R., Reid, D. G., & Simard, Y. (2008). Acoustic seabed classification : current practice and future directions, 1004–1011.

Botto, F and Iribarne, O. (2000), Contrasting Effects of Two Burrowing Crabs (‹ i› Chasmagnathus granulata‹/i› and‹ i› Uca uruguayensis‹/i›) on Sediment Composition and Transport in Estuarine Environments. *Esuarine, coastal and shelf science*. 51(2) 141. doi: 10.1006/ecss.2000.0642

Brown, C. J., Smith, S. J., Lawton, P., & Anderson, J. T. (2011). Benthic habitat mapping: A review of progress towards improved understanding of the spatial ecology of the seafloor using acoustic techniques. *Estuarine, Coastal and Shelf Science*, *92*(3), 502–520. doi:10.1016/j.ecss.2011.02.007

Clarke, J. (1994). Toward remote seafloor classification using the angular response of acoustic backscattering: a case study from multiple overlapping GLORIA data. *IEEE Journal of Oceanic Engineering*, *19*(1), 112–127. doi:10.1109/48.289456

Cogan, C. B., Todd, B. J., Lawton, P., & Noji, T. T. (2009). The role of marine habitat mapping in ecosystem-based management. *ICES Journal of Marine Science: Journal du Conseil*, *66*(9), 2033-2042.

Correll, D. L., Jordan, T. E., & Weller, D. E. (1992). Nutrient flux in a landscape: effects of coastal land use and terrestrial community mosaic on nutrient transport to coastal waters. *Estuaries*, *15*(4), 431-442.

Dadey, K. A., Janecek, T., & Klaus, A. (1992). Dry-bulk density: its use and determination. In Proceedings of the Ocean Drilling Program, Scientific Results (Vol. 126, pp. 551-554). College Station, TX.

Davis, J. C., & Sampson, R. J. (2002). *Statistics and data analysis in geology*(Vol. 3). New York: Wiley.

De, C., Chakraborty, B., House, M., & Paula, D. (2010). Preference of echo features for classification of seafloor sediments using neural networks, *31*(3).

Dijkstra, Semme J., and Mayer, Larry A., (2000), TracEd: A Remote Acoustic Seafloor Characterization System for Use with Vertical Incidence Echosounders, IEEE Oceans, p.1211-1217. Journal Article

Dronkers, J. (1986). Tidal asymmetry and estuarine morphology. *Netherlands Journal of Sea Research*, *20*, 117–131.

Dyer, K. R., Cornelisse, J., Dearnaley, M. P., Fennessy, M. J., Jones, S. E., Kappenberg, J., & Wolfstein, K. (1996). A comparison of< i> in situ</i> techniques for estuarine floc settling velocity measurements. Journal of Sea Research, 36(1), 15-29.

Fairbridge, R. W. (1980). The estuary: its definition and geodynamic cycle. Chemistry and biogeochemistry of estuaries, 1136.

Ferrini, V. L., & Flood, R. D. (2006). The effects of fine-scale surface roughness and grain size on 300 kHz multibeam backscatter intensity in sandy marine sedimentary environments. *Marine Geology*, *228*(1-4), 153–172. doi:10.1016/j.margeo.2005.11.010

Flaim, B. K., Stark, N., Moon, V., De Lange, W., Healy, T, & Kopf, A. (2011). Monitoring a dredged material disposal site on the continental shelf using the dynamic penetrometer Nimrod. In Proceedings of the Coastal Sediments' 11 Conference in Miami, USA (pp. 628-641).

Fonseca, L., & Calder, B. (2005, March). Geocoder: an efficient backscatter map constructor. In Proceedings of the US Hydrographic Conference.Fonseca, L., & Mayer, L. (2007). Remote estimation of surficial seafloor properties through the application Angular Range Analysis to multibeam sonar data. *Marine Geophysical Researches*, *28*(2), 119–126. doi:10.1007/s11001-007-9019-4

Freitas, R., Rodrigues, A. M., Morris, E., Perez-Llorens, J. L., & Quintino, V. (2008). Single-beam acoustic ground discrimination of shallow water habitats: 50kHz or 200kHz

frequency survey? *Estuarine, Coastal and Shelf Science*, *78*(4), 613–622. doi:10.1016/j.ecss.2008.02.007

Greenstreet, I.D. Tuck, G.N. Grewar, E. Armstrong, D.G. Reid, P.J. Wright An assessment of the acoustic survey technique, RoxAnn, as a means of mapping seabed habitat. ICES Journal of Marine Science, 54 (1997), pp. 939–959

Haris, K., Chakraborty, B., Ingole, B., Menezes, A., & Srivastava, R. (2012). Seabed habitat mapping employing single and multi-beam backscatter data: A case study from the western continental shelf of India. *Continental Shelf Research*, *48*, 40–49. doi:10.1016/j.csr.2012.08.010

Hasegawa, Natsuki, Hori, Masakaxu, and Mukai, Hiroshi (2008). Seasonal changes in eelgrass functions: current velocity reduction, prevention of sediment resuspension, and control of sediment–water column nutrient flux in relation to eelgrass dynamics. *Hydrobiologia*, 387 – 399. doi: 10.1007/s10750-007-9111-4

Heggen, A. (2010). On correction of depth dependence for normal incidence echosounders. 7–10.

Hobæk, H. (2011). On vertical echo sounder bottom echoes, 1–10.

Jackson, D. R., & Briggs, K. B. (2013). High-frequency bottom backscattering : Roughness versus sediment volume scattering, *92*(August 1992).

Kinsler, Lawrence; Frey, Austin; Coppens, Alan; Sanders, James (2000), *Fundamentals of Acoustics*, New York: John Wiley & Sons, Inc., ISBN 0-471-84789-5.

Leblanc, L. R., May, L., Schock, S. G., & King, J. (1992). Marine sediment classification using the chirp sonar in Narragansett, *9*,107–115.

Lurton, X. (2002). *An introduction to underwater acoustics: principles and applications*. springer.

Lyons, A. P., & Abraham, D. a. (1999). Statistical characterization of high-frequency shallow-water seafloor backscatter. *The Journal of the Acoustical Society of America*, *106*(3), 1307. doi:10.1121/1.428034

Mayer, L. a. (2006). Frontiers in Seafloor Mapping and Visualization. *Marine Geophysical Researches*, *27*(1), 7–17. doi:10.1007/s11001-005-0267-x

Milligan, S. D., Leblanc, L. R., & Middleton, F. H. (1978). Statistical grouping of acoustic reflection profiles, *64*(3), 795–807.

Parrish, C., Rogers, J, and Calder, B. (2014) “Assesstment of Waveform Features for Lidar Uncertainty Modeling in a Coastal Salt Marsh Enivronment.” IEEE Geoscience and Remote Senesing Letters: 11(2), 569-573.

Pe'eri, Shachak, and Bernard Long. "LIDAR technology applied in coastal studies and management." *Journal of Coastal Research* (2011): 1-5.

Preston, J. M., Rosenberger, A., & Collins, W. T. (2000). Bottom classification in very shallow water. In *OCEANS 2000 MTS/IEEE Conference and Exhibition*(Vol. 3, pp. 1563-1567). IEEE.

Sakamaki, T., Nishimura, O., & Sudo, R. (2006). Tidal time-scale variation in nutrient flux across the sediment–water interface of an estuarine tidal flat. Estuarine, Coastal and Shelf Science, 67(4), 653-663.

Snellen, M., Siemes, K., & Simons, D. G. (2011). Model-based sediment classification using single-beam echosounder signals. *The Journal of the Acoustical Society of America*, *129*(5), 2878–88. doi:10.1121/1.3569718

Sternlicht, D. D., & de Moustier, C. P. (2003). Remote sensing of sediment characteristics by optimized echo-envelope matching. *The Journal of the Acoustical Society of America*, *114*(5), 2727. doi:10.1121/1.1608019

Systems, S. (2008). Seafloor classification using a single beam echosounder.

Szalay, P. G. Von, & Mcconnaughey, R. A. (2002). The effect of slope and vessel speed on the performance of a single beam acoustic seabed classification

Tsemahman, A. S., Collins, W. T., & Prager, B. T. (1997, October). Acoustic seabed classification and correlation analysis of sediment properties by QTC VIEW. In *OCEANS'97. MTS/IEEE Conference Proceedings* (Vol. 2, pp. 921-926). IEEE.

Weston, D. E., Horrigan, A. A., Thomas, S. J. L., & Revie, J. (1969). Studies of sound transmission fluctuations in shallow coastal waters. *Philosophical Transactions for the Royal Society of London. Series A, Mathematical and Physical Sciences*, 567-606.

Chapter 6

Appendices

A - Videography

A significant amount of bottom video was collected to explore the *in situ* appearance and characteristics of bottom sediment along the sampling lines. The video was not used in a qualitative analysis, but does serve as a visual affirmation of the acoustic, sediment size, and bulk density data. The following pictures are extracted from the videos collected at the designated lines. Time of collection and GPS coordinates of the boat at the time of collection are included in the upper right hand corner of each picture.

Line 1:

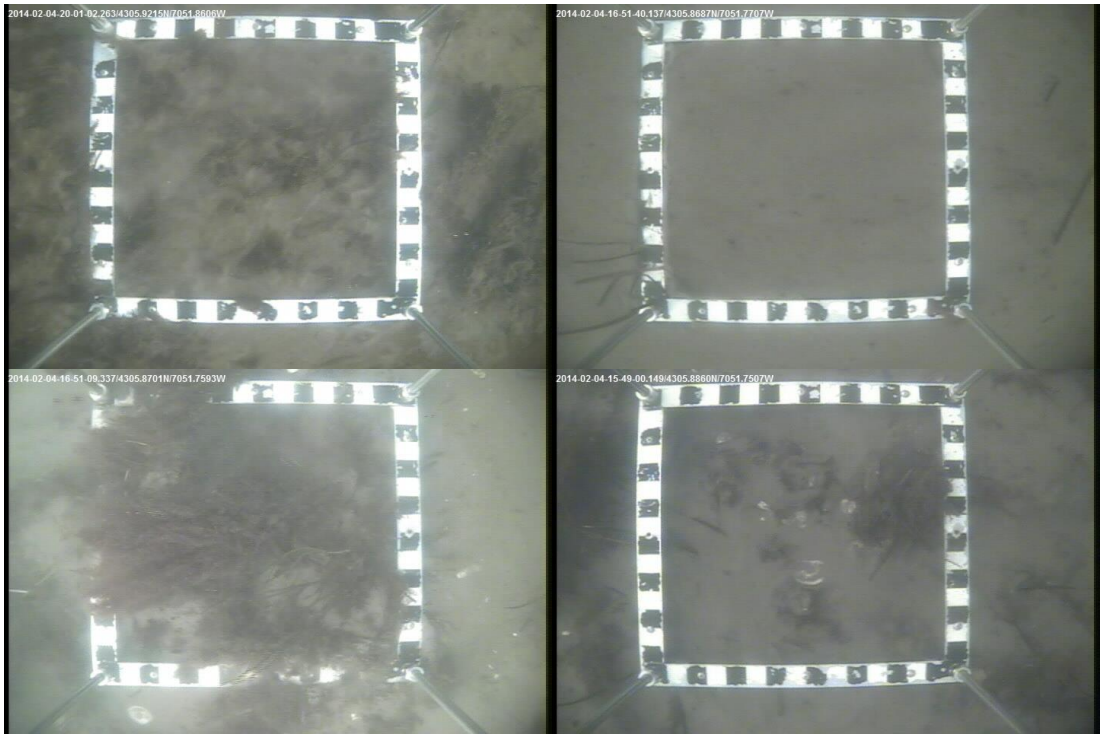

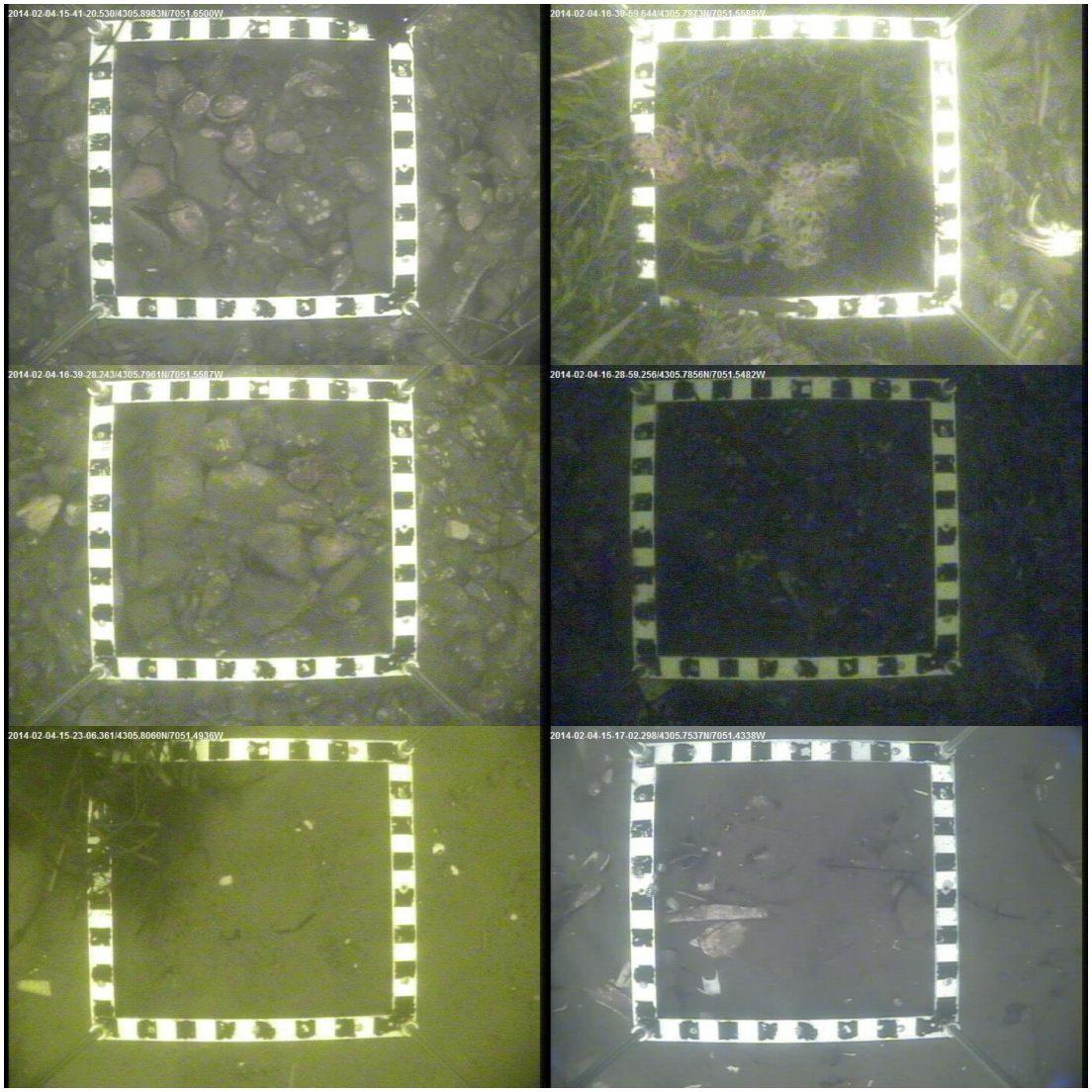
2014-02-04-15-41-20.530/4305.8983N/7051.6500W
2014-02-04-16-39-28.243/4305.7961N/7051.5587W
2014-02-04-16-28-59.256/4305.7856N/7051.5482W
2014-02-04-15-23-06.361/4305.8060N/7051.4936W
2014-02-04-15-17-02.298/4305.7537N/7051.4338W

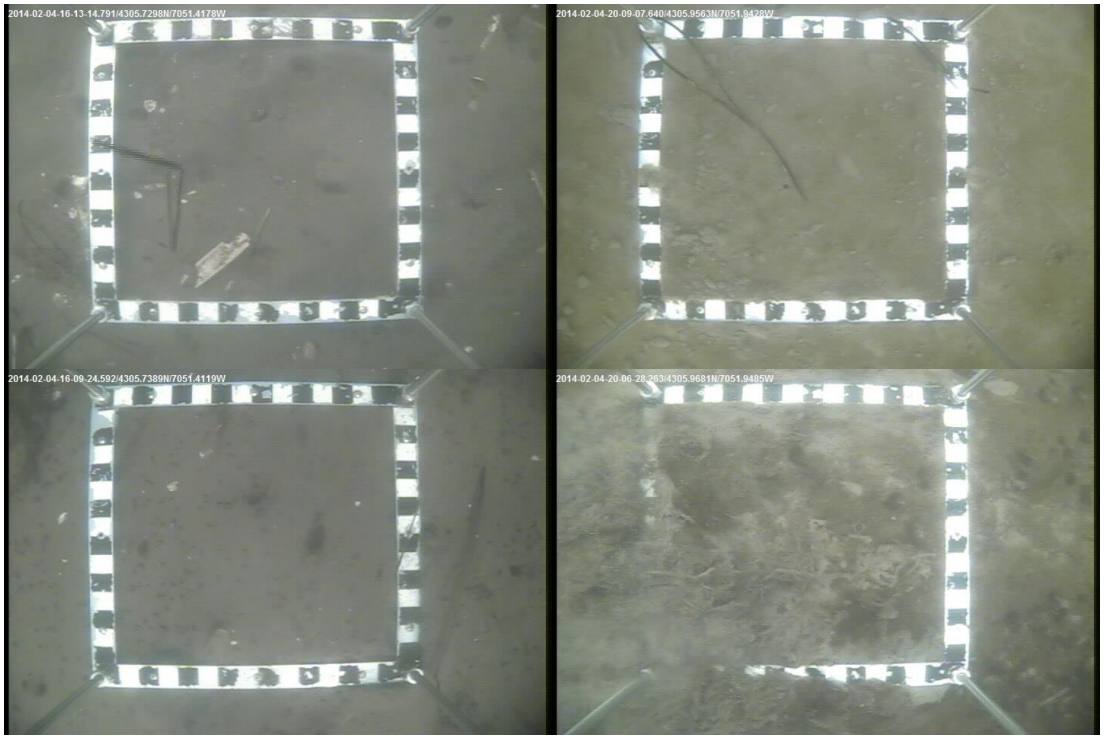

Line 2:

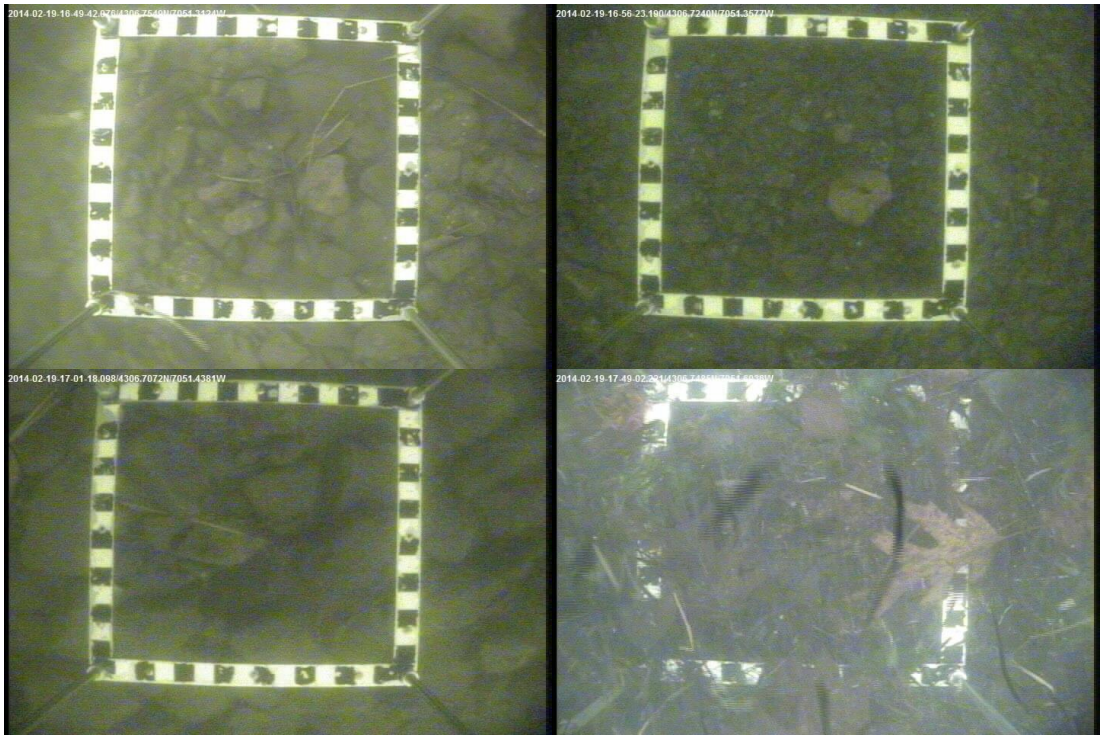

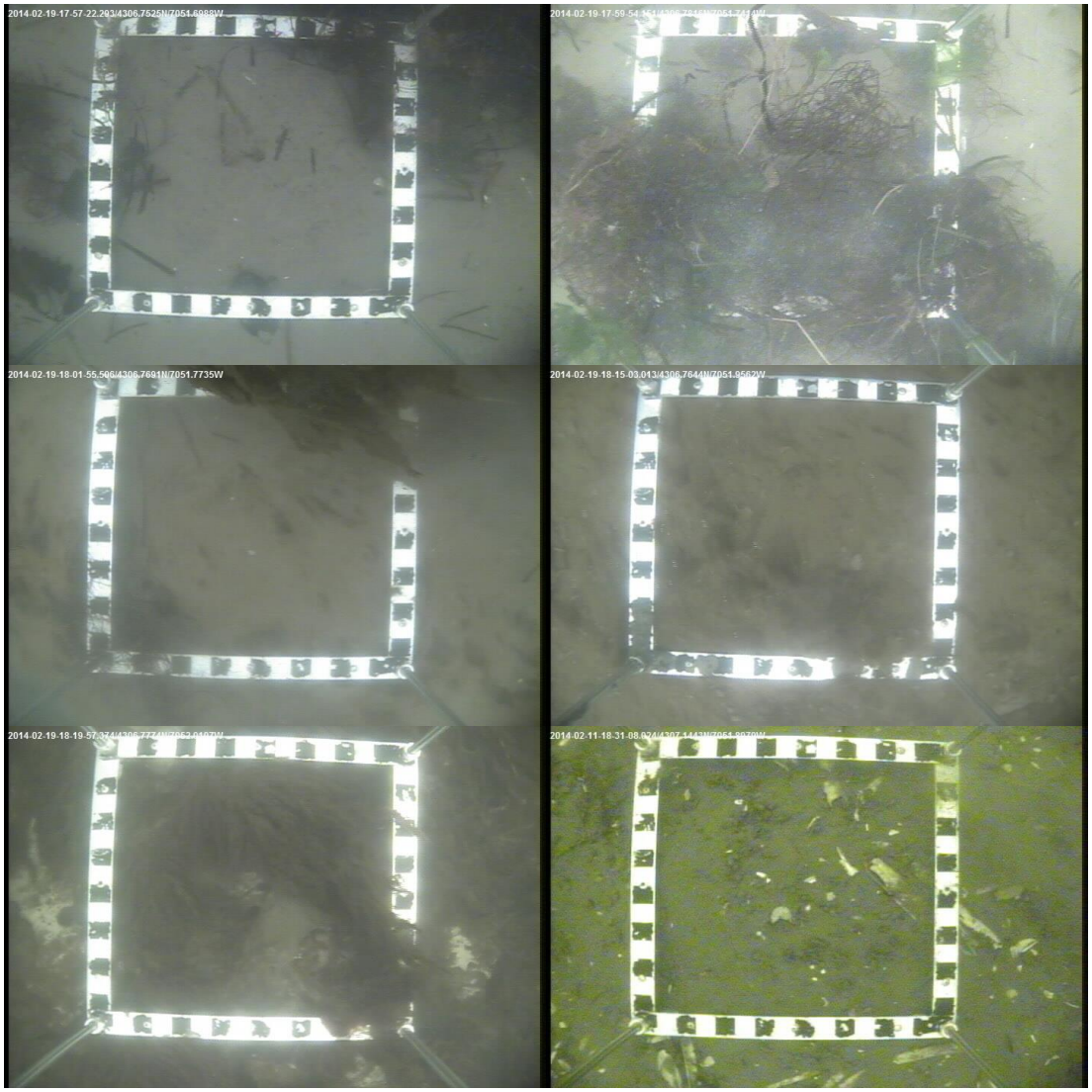

Line 3:

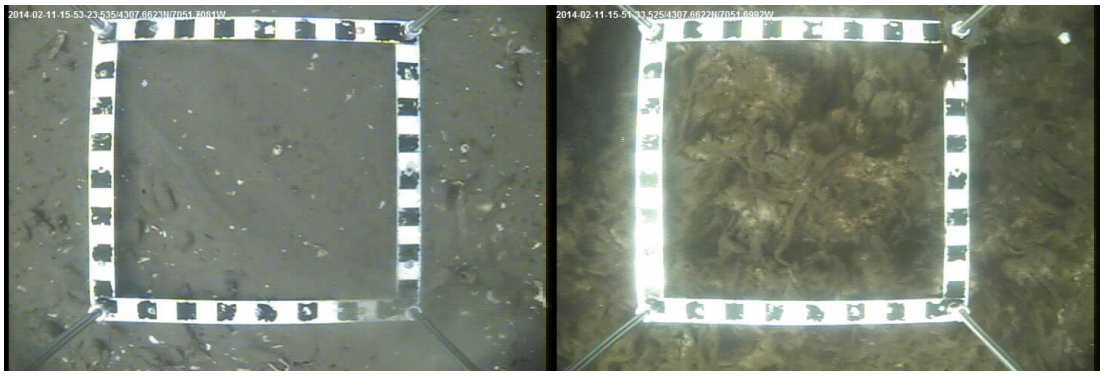

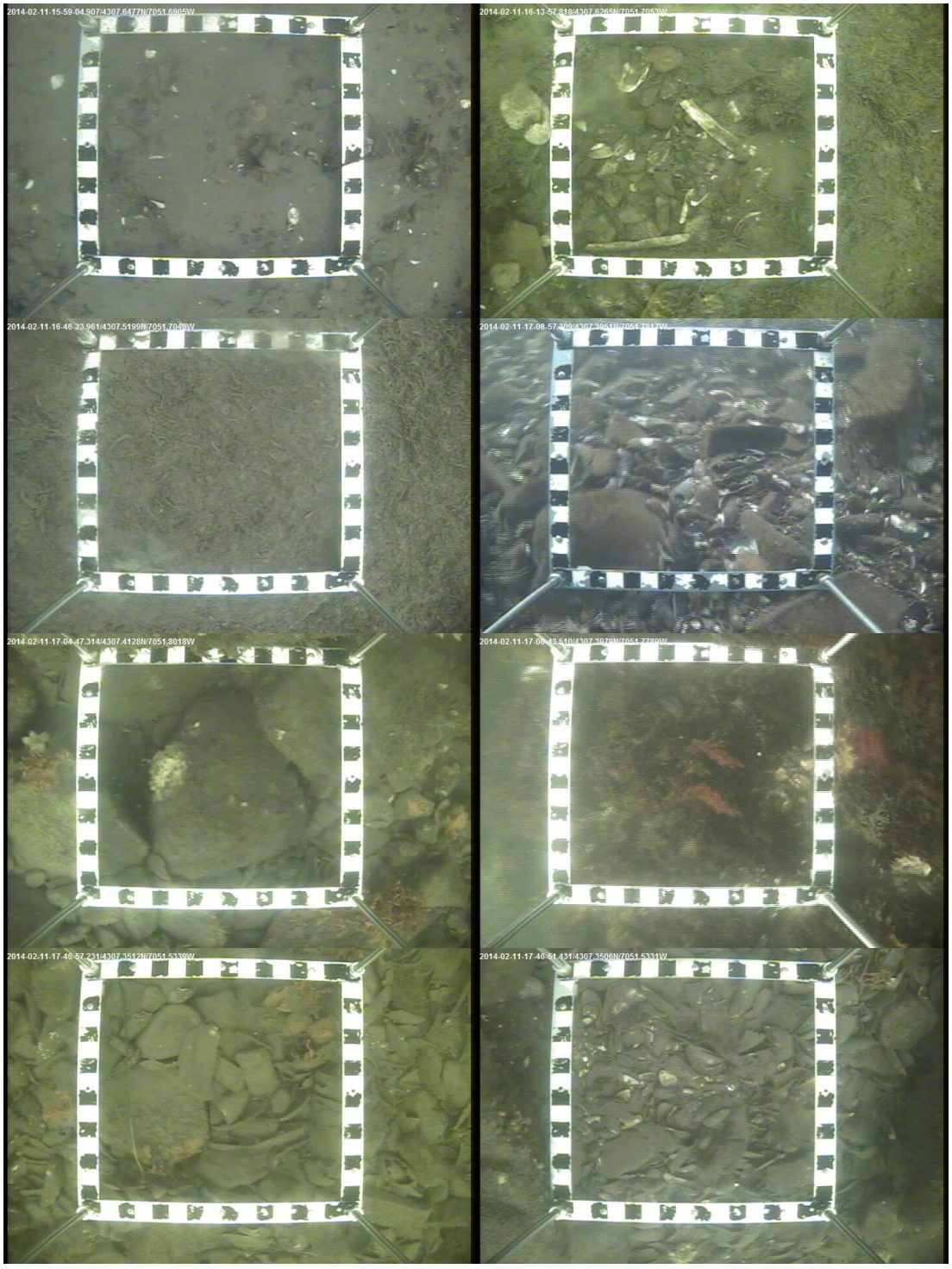
2014-02-11-15-59-04.907/4307.6477N/7051.6905W
2014-02-11-16-13-57.818/4307.6255N/7051.7053W
2014-02-11-16-46-23.961/4307.5199N/7051.7040W
2014-02-11-17-08-57.200/4307.3954N/7051.7317W
2014-02-11-17-04-47.314/4307.4128N/7051.8018W
2014-02-11-17-46-57.231/4307.3512N/7051.5339W
2014-02-11-17-46-51.431/4307.3506N/7051.5331W

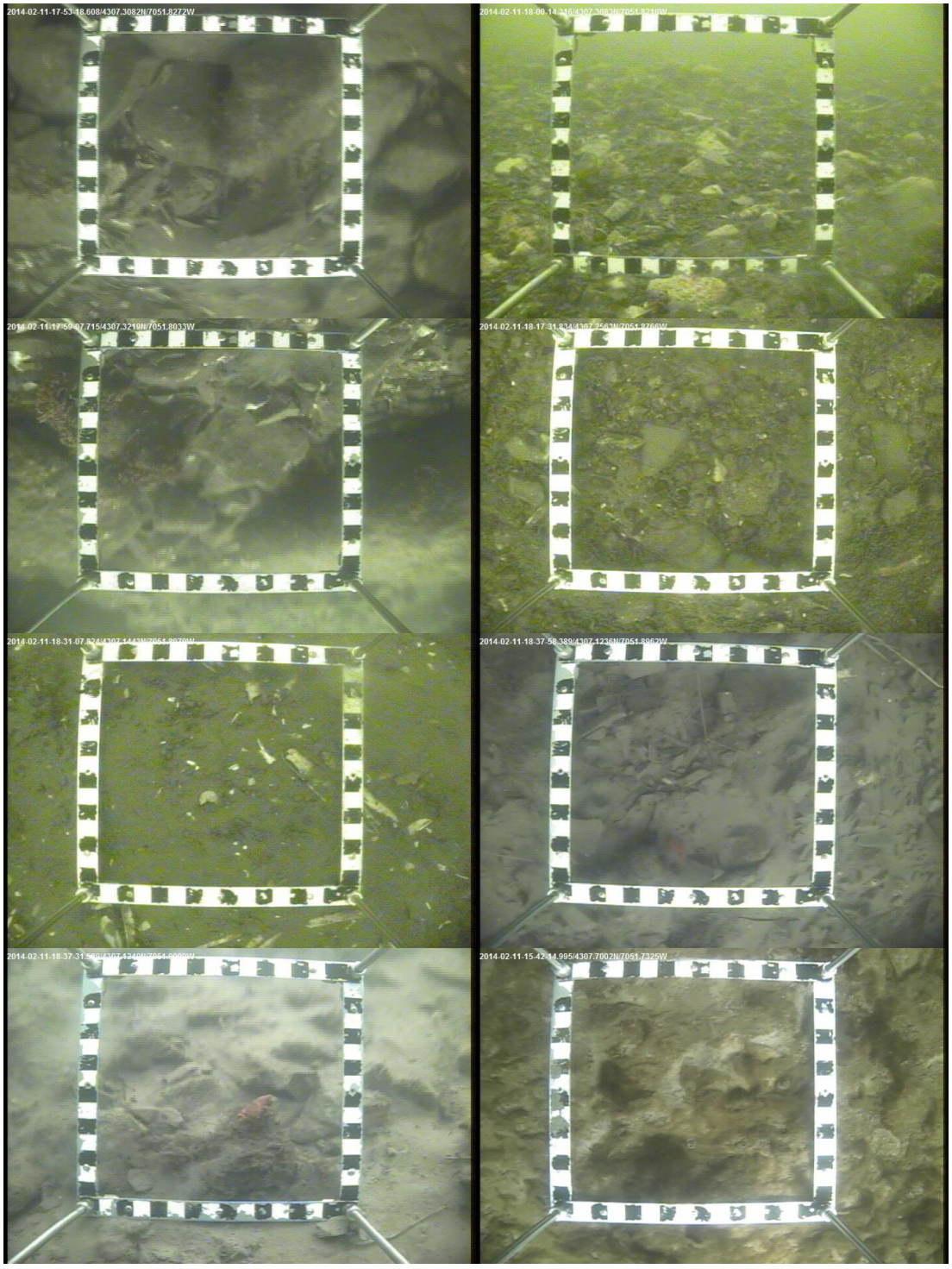
2014-02-11-17-53-18.608/4307.3082N/7051.8272W
2014-02-11-18-00-14.316/4307.3083N/7051.8218W
2014-02-11-17-59-07.715/4307.3219N/7051.8033W
2014-02-11-18-17-31.834/4307.2563N/7051.8768W
2014-02-11-18-31-07.824/4307.1443N/7054.4979W
2014-02-11-18-37-58.389/4307.1236N/7051.8962W
2014-02-11-18-37-31.589/4307.1240N/7054.4989W
2014-02-11-15-42-14.995/4307.7002N/7051.7325W

Line 4:

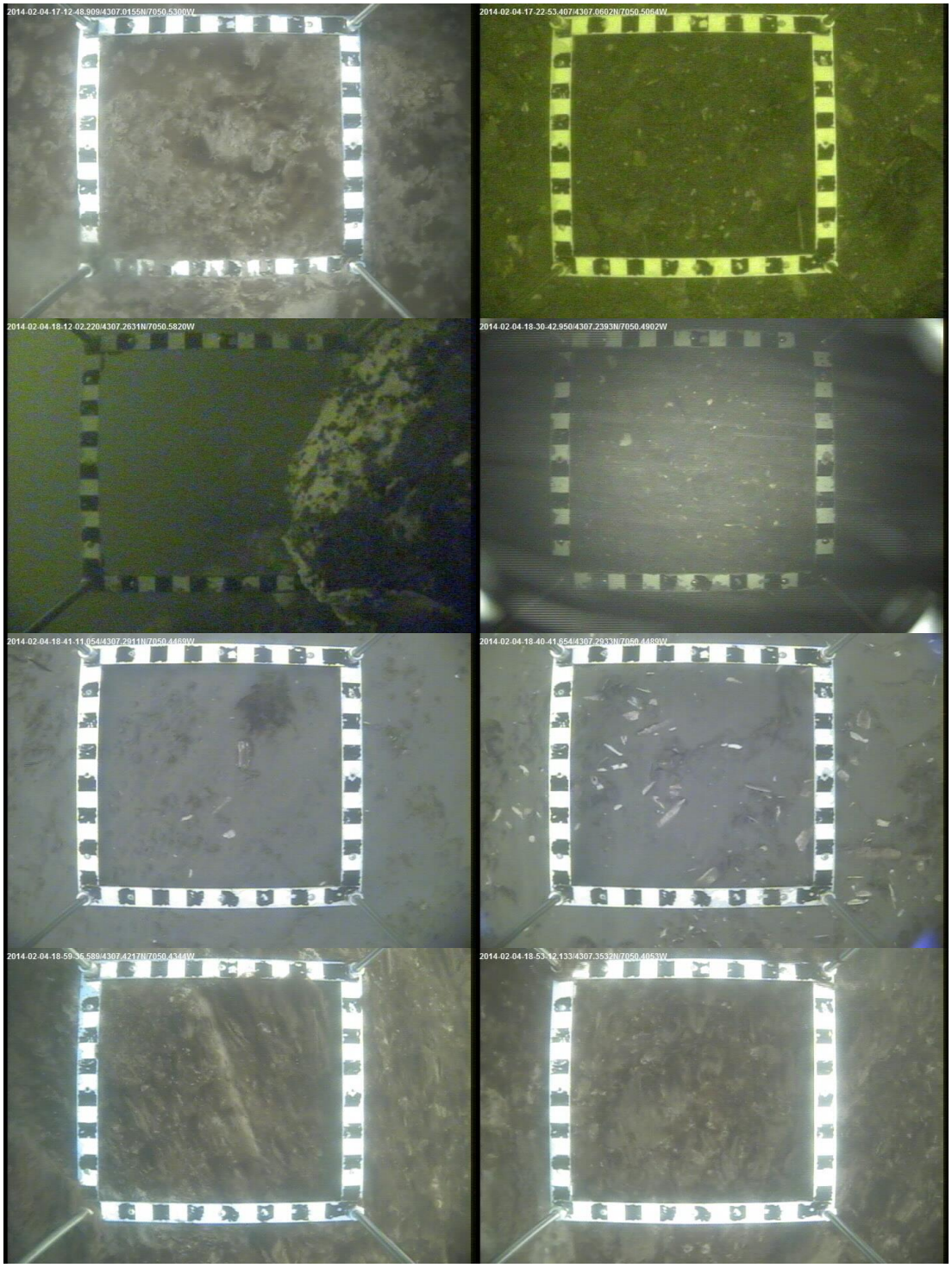
2014-02-04-17-12-48.909/4307.0155N/7050.5300W
2014-02-04-17-22-53.407/4307.0602N/7050.5064W
2014-02-04-18-12-02.220/4307.2631N/7050.5820W
2014-02-04-18-30-42.950/4307.2393N/7050.4902W
2014-02-04-18-41-11.054/4307.2911N/7050.4168W
2014-02-04-18-40-41.654/4307.2933N/7050.4189W
2014-02-04-18-59-35.589/4307.4217N/7050.4344W
2014-02-04-18-53-12.133/4307.3532N/7050.4053W

Video data from Line 6 and 7 is unavailable because of high turbidity in the water during the time of collection (see below).

B – Additional Models and Mud Fraction Predictions

Waveform data and EOF data was produced and analyzed in a few different ways by averaging waveforms and using different properties for the EOF analysis. Ultimately, in an effort to remove any bias from the analysis, individual waveform properties were used and all properties were included in the EOF analysis. However, some of the other approaches suggest ignoring the non-linear wave form properties produce a better model. Also, trials averaging 2, 5, 10, and 20 pings produced more spatially consistent waveform properties. The results of some of these different trials are presented below.

Model and Specifications	Predicted Mud Fraction
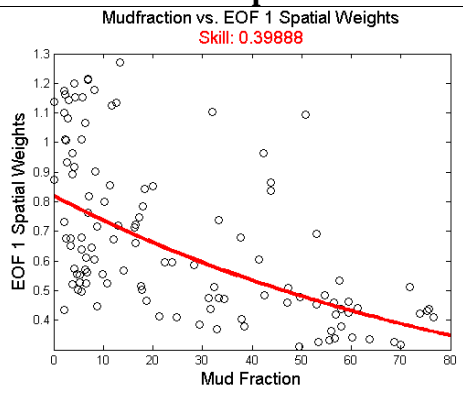 2 Waveforms Averaged	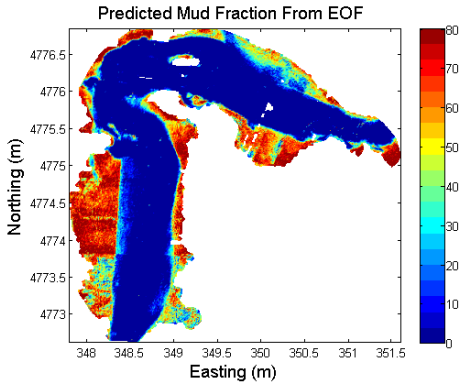
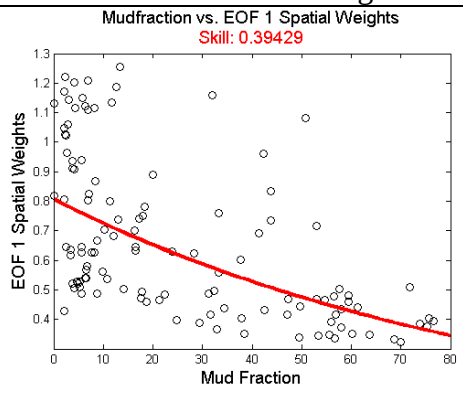 5 Waveforms Averaged	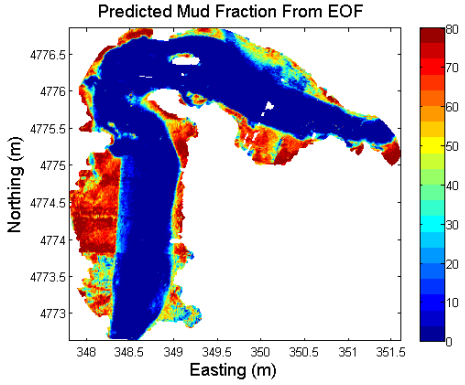
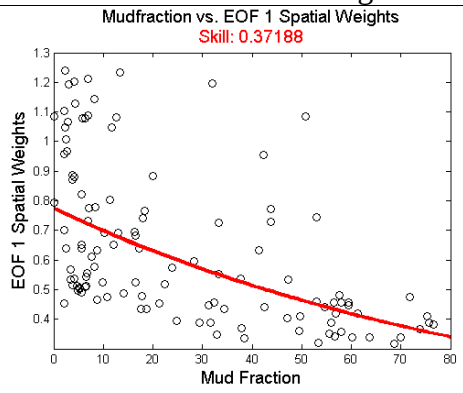 10 Waveforms Averaged	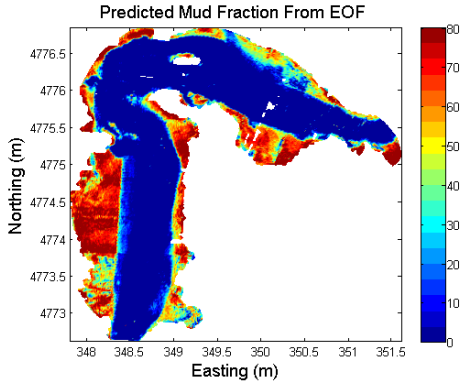

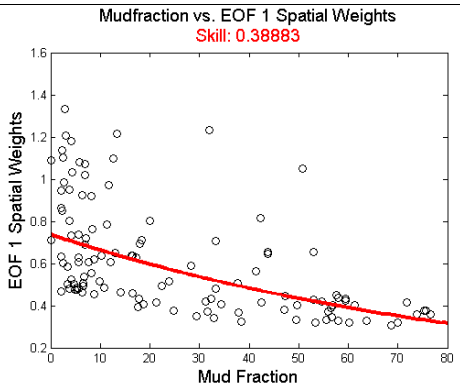

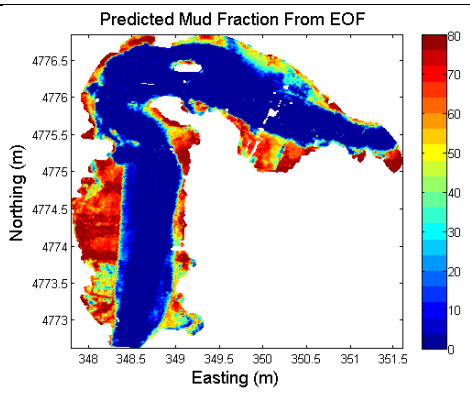

20 Waveforms Averaged

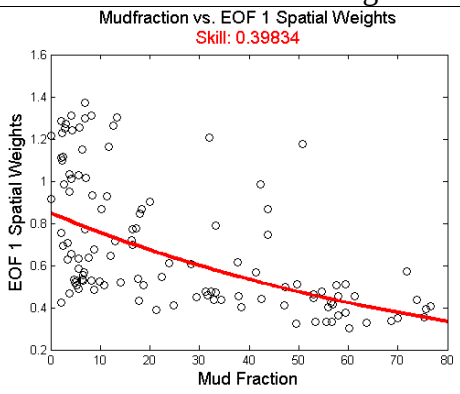

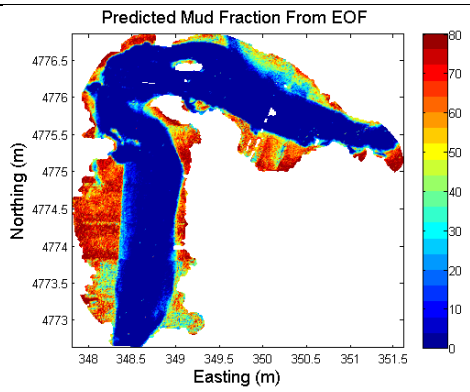

Individual Waveform Properties

Depth included

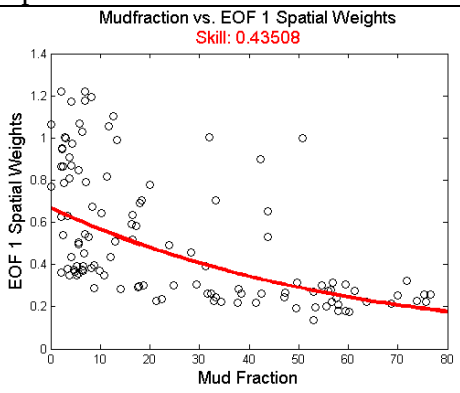

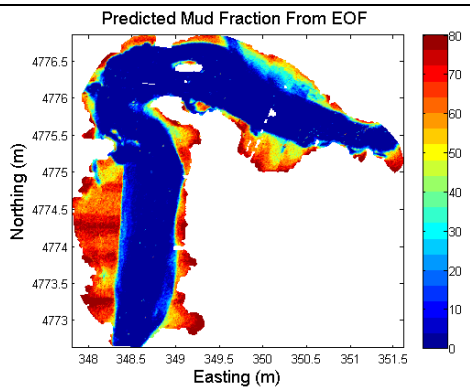

Individual Waveform Properties

Linear Properties only (Maximum, Mean, Width, Rise Time)

C – Sediment Size Distributions

A sediment size distribution was obtained for ever grab sample. All of the size distributions for every sample that could be run through the Mastersizer are presented below and identified by Line number and Latitude and Longitude.

Line 1:

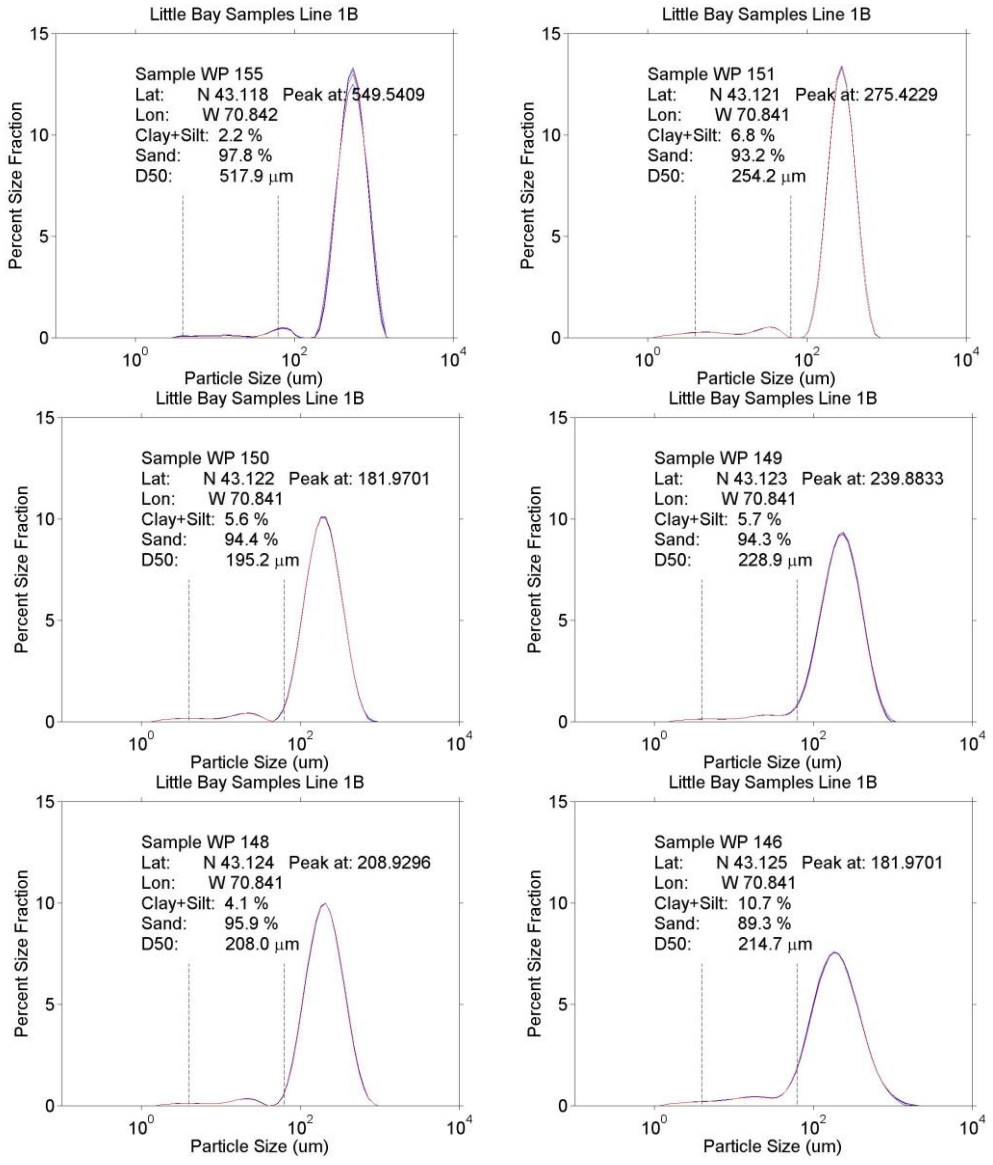

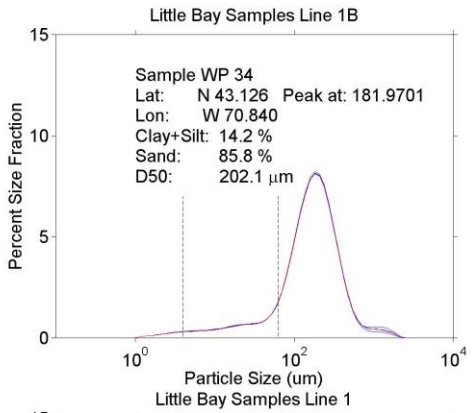
Little Bay Samples Line 1B
Sample WP 34
Lat: N 43.126 Peak at: 181.9701
Lon: W 70.840
Clay+Silt: 14.2 %
Sand: 85.8 %
D50: 202.1 μm
Percent Size Fraction
Particle Size (um)

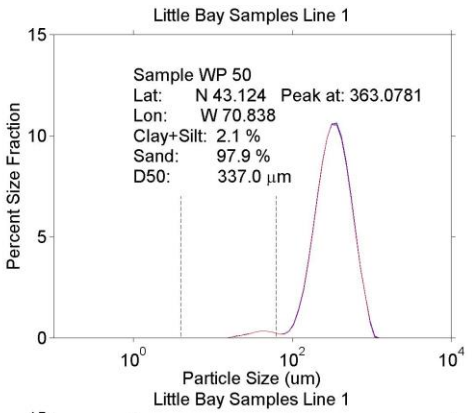
Little Bay Samples Line 1
Sample WP 50
Lat: N 43.124 Peak at: 363.0781
Lon: W 70.838
Clay+Silt: 2.1 %
Sand: 97.9 %
D50: 337.0 μm
Percent Size Fraction
Particle Size (um)

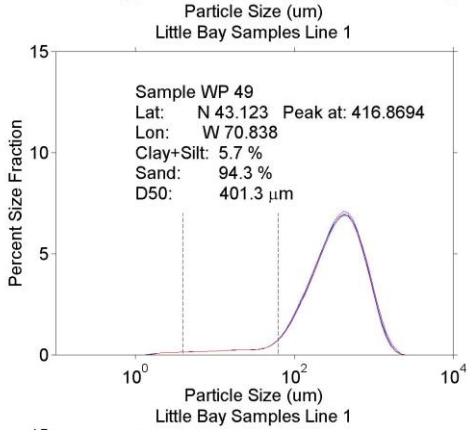
Little Bay Samples Line 1
Sample WP 49
Lat: N 43.123 Peak at: 416.8694
Lon: W 70.838
Clay+Silt: 5.7 %
Sand: 94.3 %
D50: 401.3 μm
Percent Size Fraction
Particle Size (um)

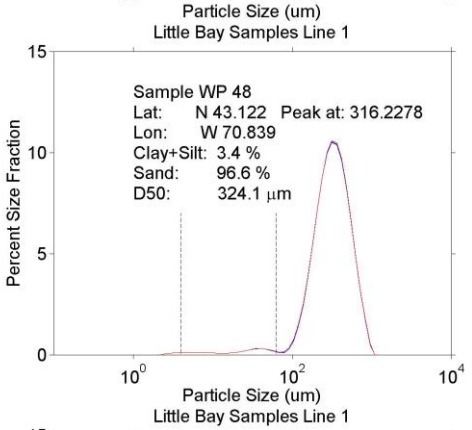
Little Bay Samples Line 1
Sample WP 48
Lat: N 43.122 Peak at: 316.2278
Lon: W 70.839
Clay+Silt: 3.4 %
Sand: 96.6 %
D50: 324.1 μm
Percent Size Fraction
Particle Size (um)

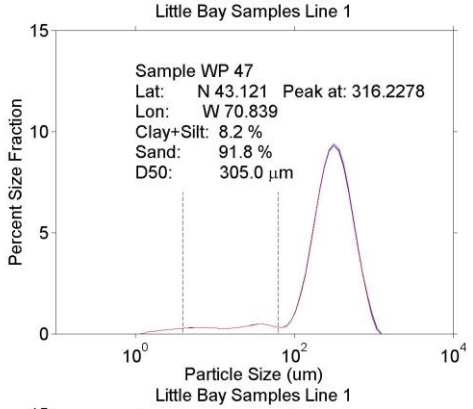
Little Bay Samples Line 1
Sample WP 47
Lat: N 43.121 Peak at: 316.2278
Lon: W 70.839
Clay+Silt: 8.2 %
Sand: 91.8 %
D50: 305.0 μm
Percent Size Fraction
Particle Size (um)

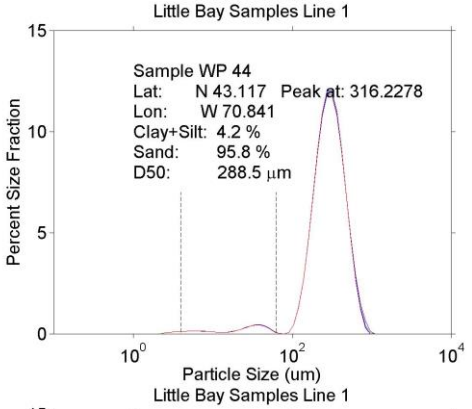
Little Bay Samples Line 1
Sample WP 44
Lat: N 43.117 Peak at: 316.2278
Lon: W 70.841
Clay+Silt: 4.2 %
Sand: 95.8 %
D50: 288.5 μm
Percent Size Fraction
Particle Size (um)

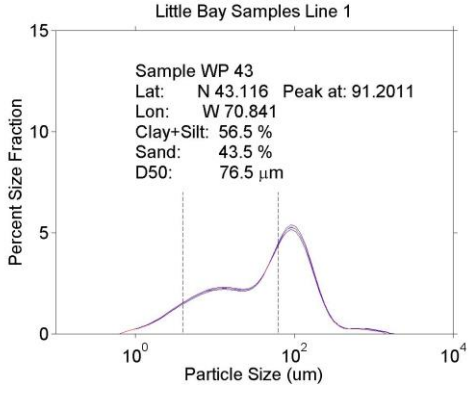
Little Bay Samples Line 1
Sample WP 43
Lat: N 43.116 Peak at: 91.2011
Lon: W 70.841
Clay+Silt: 56.5 %
Sand: 43.5 %
D50: 76.5 μm
Percent Size Fraction
Particle Size (um)

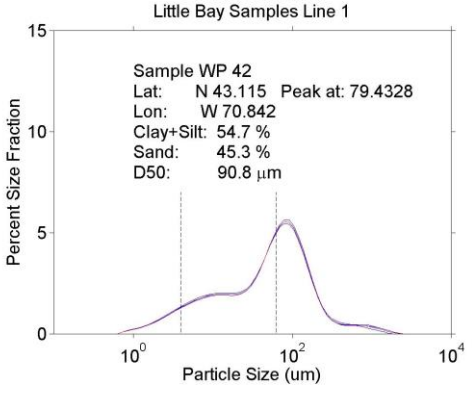
Little Bay Samples Line 1
Sample WP 42
Lat: N 43.115 Peak at: 79.4328
Lon: W 70.842
Clay+Silt: 54.7 %
Sand: 45.3 %
D50: 90.8 μm
Percent Size Fraction
Particle Size (um)

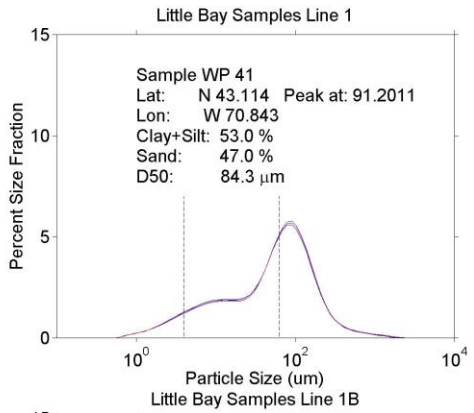
Little Bay Samples Line 1
Sample WP 41
Lat: N 43.114 Peak at: 91.2011
Lon: W 70.843
Clay+Silt: 53.0 %
Sand: 47.0 %
D50: 84.3 μm
Percent Size Fraction
Particle Size (um)

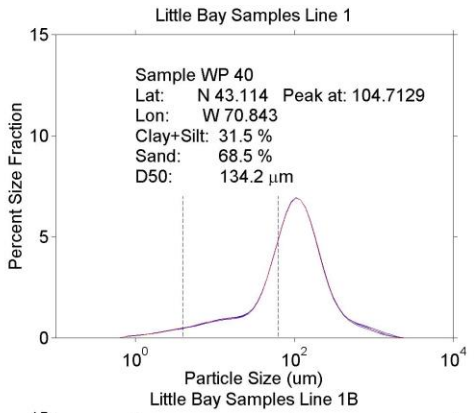
Little Bay Samples Line 1
Sample WP 40
Lat: N 43.114 Peak at: 104.7129
Lon: W 70.843
Clay+Silt: 31.5 %
Sand: 68.5 %
D50: 134.2 μm
Percent Size Fraction
Particle Size (um)

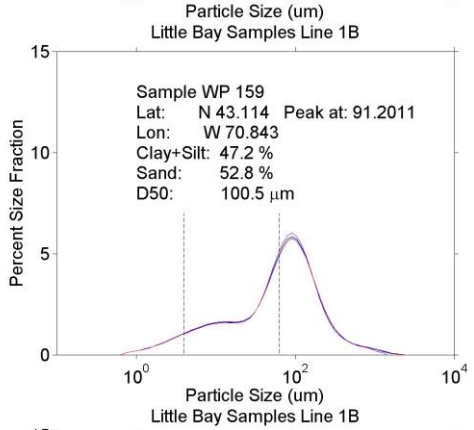
Little Bay Samples Line 1B
Sample WP 159
Lat: N 43.114 Peak at: 91.2011
Lon: W 70.843
Clay+Silt: 47.2 %
Sand: 52.8 %
D50: 100.5 μm
Percent Size Fraction
Particle Size (um)

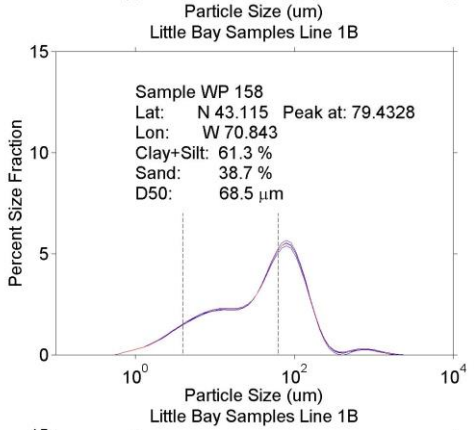
Little Bay Samples Line 1B
Sample WP 158
Lat: N 43.115 Peak at: 79.4328
Lon: W 70.843
Clay+Silt: 61.3 %
Sand: 38.7 %
D50: 68.5 μm
Percent Size Fraction
Particle Size (um)

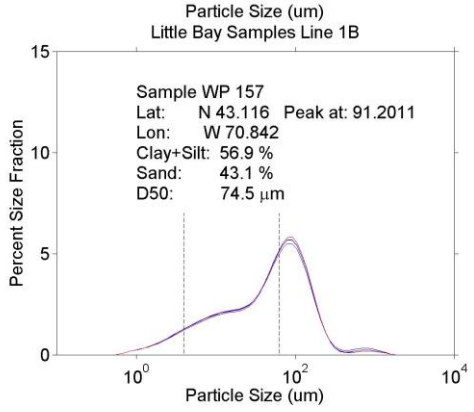
Little Bay Samples Line 1B
Sample WP 157
Lat: N 43.116 Peak at: 91.2011
Lon: W 70.842
Clay+Silt: 56.9 %
Sand: 43.1 %
D50: 74.5 μm
Percent Size Fraction
Particle Size (um)

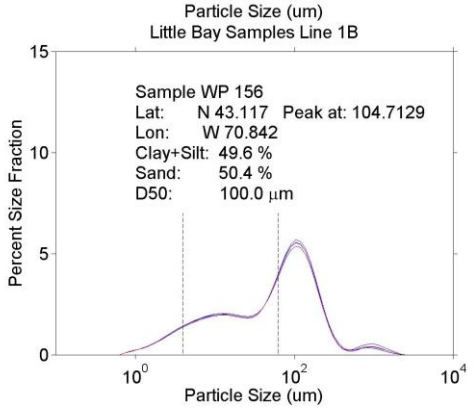
Little Bay Samples Line 1B
Sample WP 156
Lat: N 43.117 Peak at: 104.7129
Lon: W 70.842
Clay+Silt: 49.6 %
Sand: 50.4 %
D50: 100.0 μm
Percent Size Fraction
Particle Size (um)

Line 2:

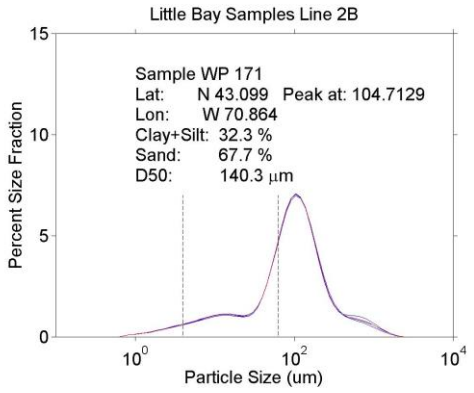
Little Bay Samples Line 2B
Sample WP 171
Lat: N 43.099 Peak at: 104.7129
Lon: W 70.864
Clay+Silt: 32.3 %
Sand: 67.7 %
D50: 140.3 μm
Percent Size Fraction
Particle Size (um)

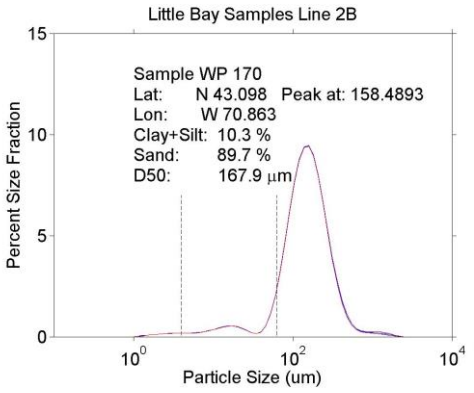
Little Bay Samples Line 2B
Sample WP 170
Lat: N 43.098 Peak at: 158.4893
Lon: W 70.863
Clay+Silt: 10.3 %
Sand: 89.7 %
D50: 167.9 μm
Percent Size Fraction
Particle Size (um)

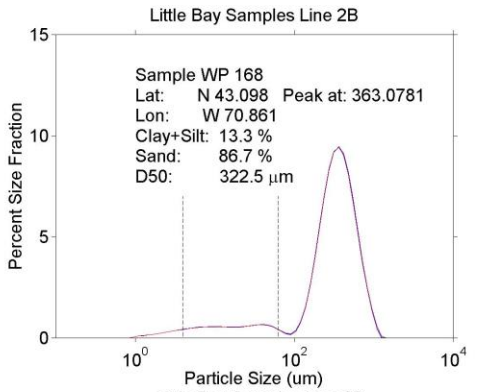
Little Bay Samples Line 2B
Sample WP 168
Lat: N 43.098 Peak at: 363.0781
Lon: W 70.861
Clay+Silt: 13.3 %
Sand: 86.7 %
D50: 322.5 μm
Percent Size Fraction
Particle Size (um)

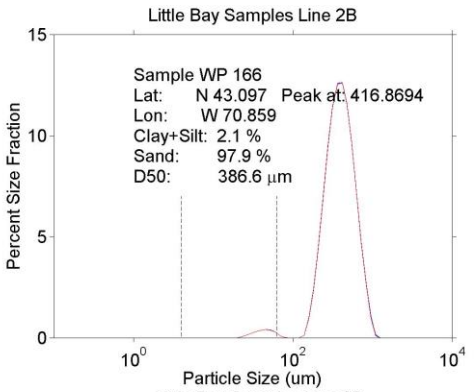
Little Bay Samples Line 2B
Sample WP 166
Lat: N 43.097 Peak at: 416.8694
Lon: W 70.859
Clay+Silt: 2.1 %
Sand: 97.9 %
D50: 386.6 μm
Percent Size Fraction
Particle Size (um)

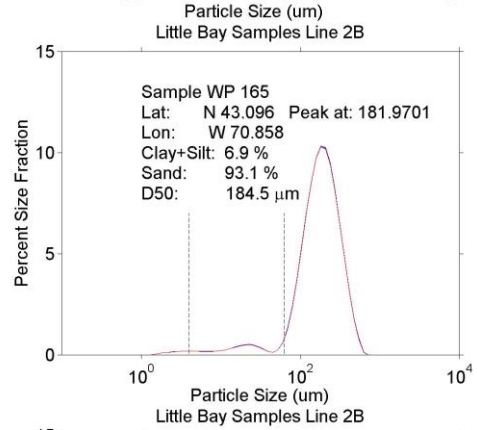
Little Bay Samples Line 2B
Sample WP 165
Lat: N 43.096 Peak at: 181.9701
Lon: W 70.858
Clay+Silt: 6.9 %
Sand: 93.1 %
D50: 184.5 μm
Percent Size Fraction
Particle Size (um)

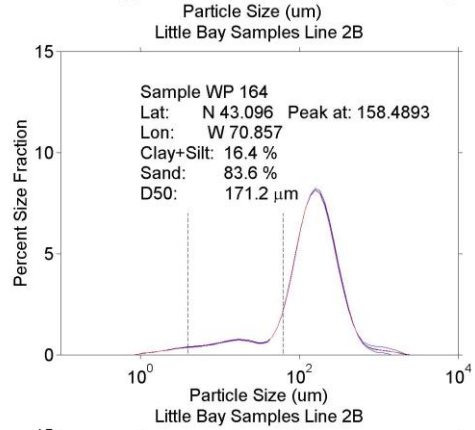
Little Bay Samples Line 2B
Sample WP 164
Lat: N 43.096 Peak at: 158.4893
Lon: W 70.857
Clay+Silt: 16.4 %
Sand: 83.6 %
D50: 171.2 μm
Percent Size Fraction
Particle Size (um)

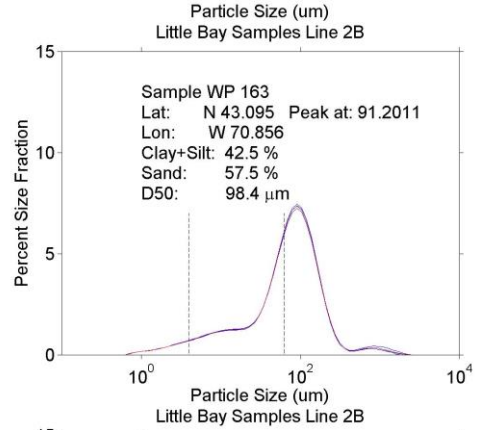
Little Bay Samples Line 2B
Sample WP 163
Lat: N 43.095 Peak at: 91.2011
Lon: W 70.856
Clay+Silt: 42.5 %
Sand: 57.5 %
D50: 98.4 μm
Percent Size Fraction
Particle Size (um)

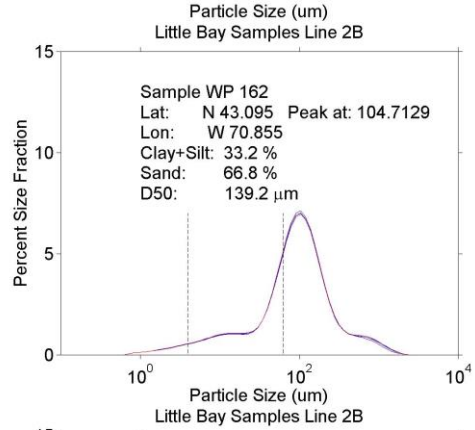
Little Bay Samples Line 2B
Sample WP 162
Lat: N 43.095 Peak at: 104.7129
Lon: W 70.855
Clay+Silt: 33.2 %
Sand: 66.8 %
D50: 139.2 μm
Percent Size Fraction
Particle Size (um)

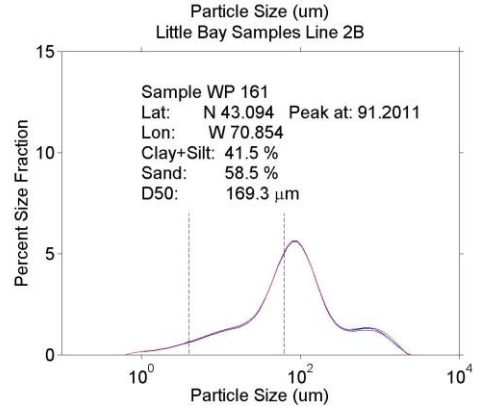
Little Bay Samples Line 2B
Sample WP 161
Lat: N 43.094 Peak at: 91.2011
Lon: W 70.854
Clay+Silt: 41.5 %
Sand: 58.5 %
D50: 169.3 μm
Percent Size Fraction
Particle Size (um)

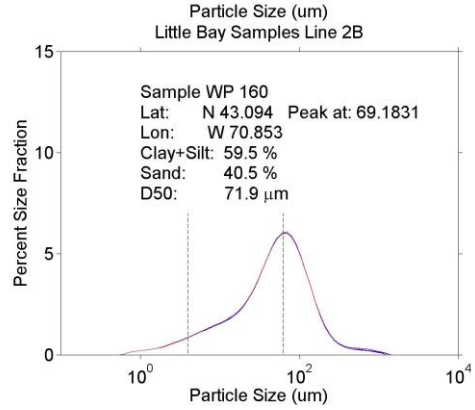
Little Bay Samples Line 2B
Sample WP 160
Lat: N 43.094 Peak at: 69.1831
Lon: W 70.853
Clay+Silt: 59.5 %
Sand: 40.5 %
D50: 71.9 μm
Percent Size Fraction
Particle Size (um)

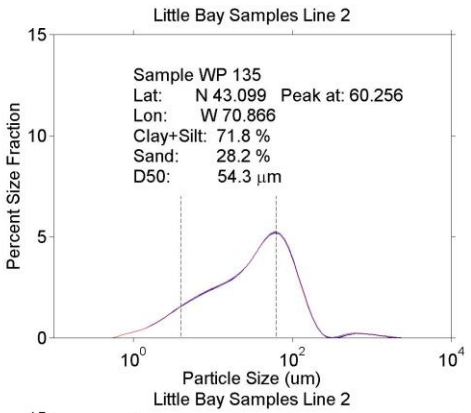
Little Bay Samples Line 2
Sample WP 135
Lat: N 43.099 Peak at: 60.256
Lon: W 70.866
Clay+Silt: 71.8 %
Sand: 28.2 %
D50: 54.3 μm
Percent Size Fraction
Particle Size (um)

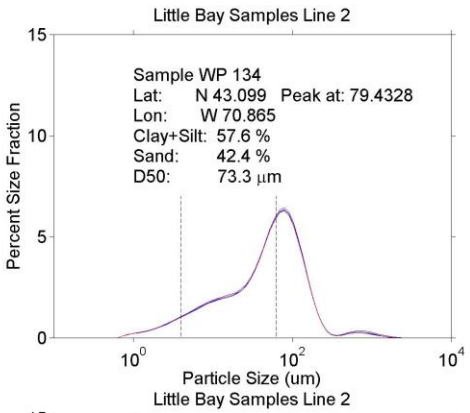
Little Bay Samples Line 2
Sample WP 134
Lat: N 43.099 Peak at: 79.4328
Lon: W 70.865
Clay+Silt: 57.6 %
Sand: 42.4 %
D50: 73.3 μm
Percent Size Fraction
Particle Size (um)

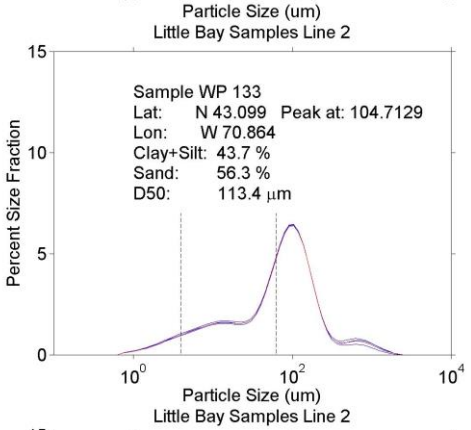
Little Bay Samples Line 2
Sample WP 133
Lat: N 43.099 Peak at: 104.7129
Lon: W 70.864
Clay+Silt: 43.7 %
Sand: 56.3 %
D50: 113.4 μm
Percent Size Fraction
Particle Size (um)

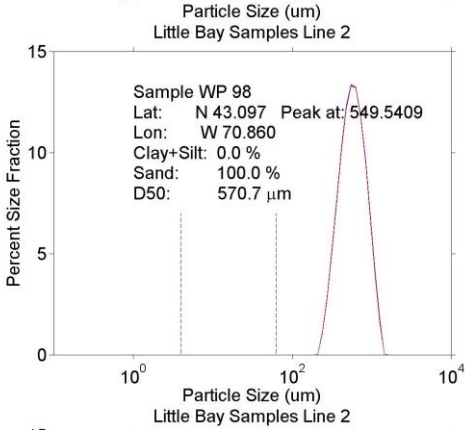
Little Bay Samples Line 2
Sample WP 98
Lat: N 43.097 Peak at: 549.5409
Lon: W 70.860
Clay+Silt: 0.0 %
Sand: 100.0 %
D50: 570.7 μm
Percent Size Fraction
Particle Size (um)

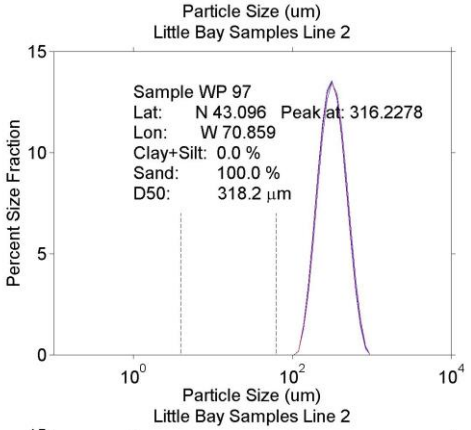
Little Bay Samples Line 2
Sample WP 97
Lat: N 43.096 Peak at: 316.2278
Lon: W 70.859
Clay+Silt: 0.0 %
Sand: 100.0 %
D50: 318.2 μm
Percent Size Fraction
Particle Size (um)

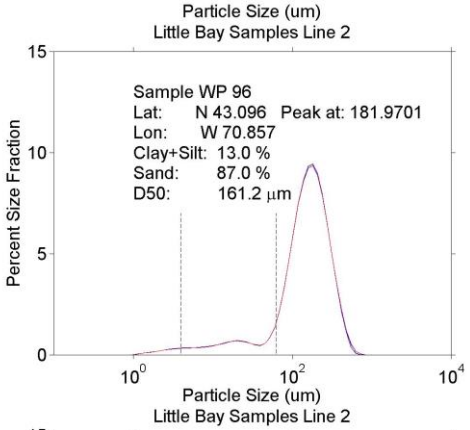
Little Bay Samples Line 2
Sample WP 96
Lat: N 43.096 Peak at: 181.9701
Lon: W 70.857
Clay+Silt: 13.0 %
Sand: 87.0 %
D50: 161.2 μm
Percent Size Fraction
Particle Size (um)

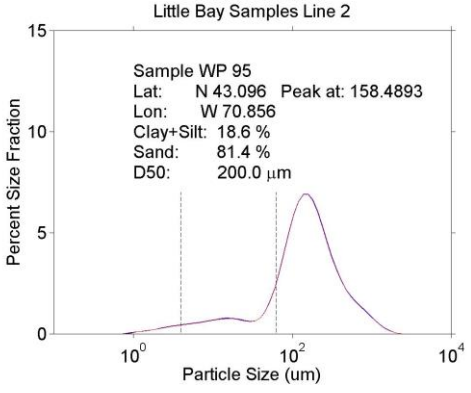
Little Bay Samples Line 2
Sample WP 95
Lat: N 43.096 Peak at: 158.4893
Lon: W 70.856
Clay+Silt: 18.6 %
Sand: 81.4 %
D50: 200.0 μm
Percent Size Fraction
Particle Size (um)

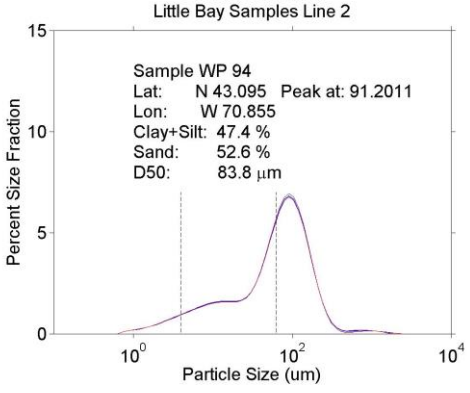
Little Bay Samples Line 2
Sample WP 94
Lat: N 43.095 Peak at: 91.2011
Lon: W 70.855
Clay+Silt: 47.4 %
Sand: 52.6 %
D50: 83.8 μm
Percent Size Fraction
Particle Size (um)

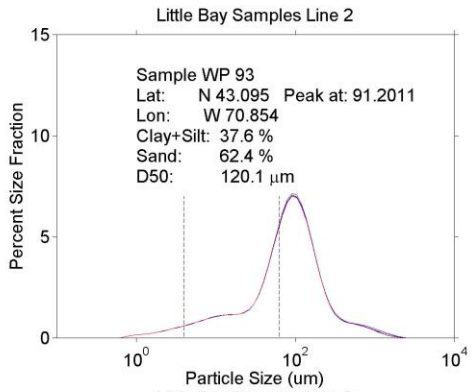
Little Bay Samples Line 2
Sample WP 93
Lat: N 43.095 Peak at: 91.2011
Lon: W 70.854
Clay+Silt: 37.6 %
Sand: 62.4 %
D50: 120.1 μm
Percent Size Fraction
Particle Size (um)

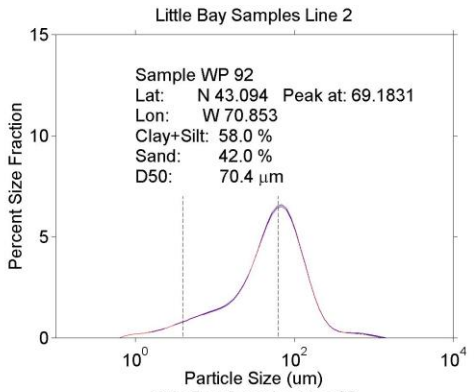
Little Bay Samples Line 2
Sample WP 92
Lat: N 43.094 Peak at: 69.1831
Lon: W 70.853
Clay+Silt: 58.0 %
Sand: 42.0 %
D50: 70.4 μm
Percent Size Fraction
Particle Size (um)

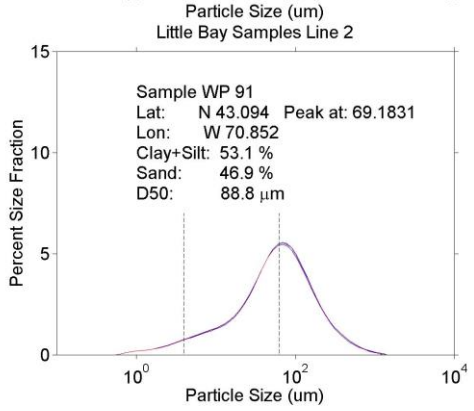
Little Bay Samples Line 2
Sample WP 91
Lat: N 43.094 Peak at: 69.1831
Lon: W 70.852
Clay+Silt: 53.1 %
Sand: 46.9 %
D50: 88.8 μm
Percent Size Fraction
Particle Size (um)

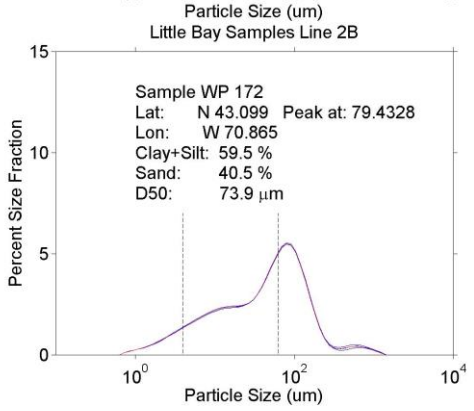
Little Bay Samples Line 2B
Sample WP 172
Lat: N 43.099 Peak at: 79.4328
Lon: W 70.865
Clay+Silt: 59.5 %
Sand: 40.5 %
D50: 73.9 μm
Percent Size Fraction
Particle Size (um)

Line 3:

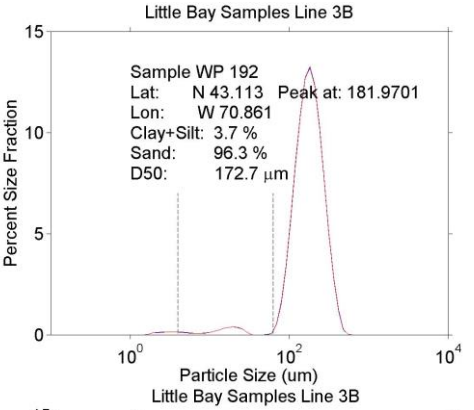
Little Bay Samples Line 3B
Sample WP 192
Lat: N 43.113 Peak at: 181.9701
Lon: W 70.861
Clay+Silt: 3.7 %
Sand: 96.3 %
D50: 172.7 μm
Percent Size Fraction
Particle Size (um)

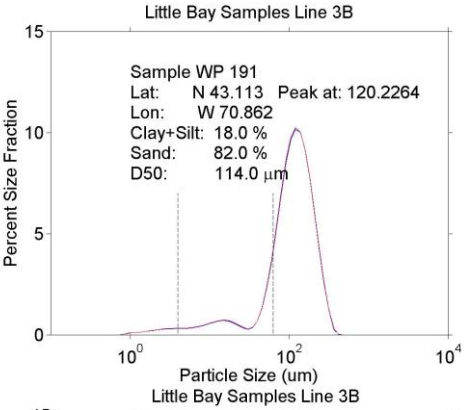
Little Bay Samples Line 3B
Sample WP 191
Lat: N 43.113 Peak at: 120.2264
Lon: W 70.862
Clay+Silt: 18.0 %
Sand: 82.0 %
D50: 114.0 μm
Percent Size Fraction
Particle Size (um)

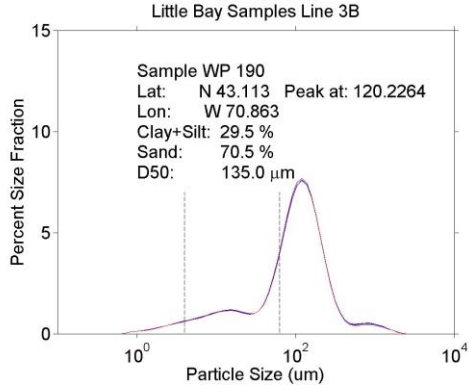
Little Bay Samples Line 3B
Sample WP 190
Lat: N 43.113 Peak at: 120.2264
Lon: W 70.863
Clay+Silt: 29.5 %
Sand: 70.5 %
D50: 135.0 μm
Percent Size Fraction
Particle Size (um)

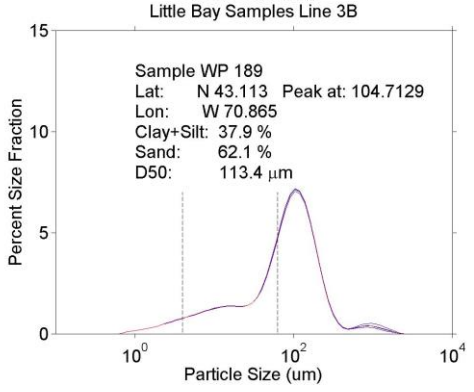
Little Bay Samples Line 3B
Sample WP 189
Lat: N 43.113 Peak at: 104.7129
Lon: W 70.865
Clay+Silt: 37.9 %
Sand: 62.1 %
D50: 113.4 μm
Percent Size Fraction
Particle Size (um)

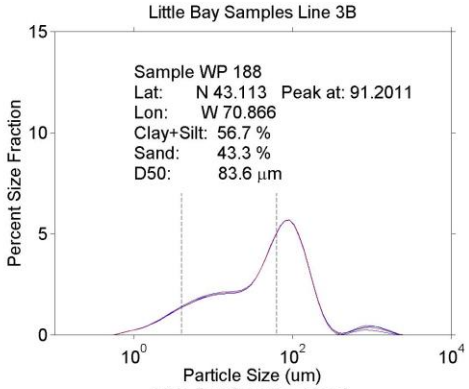
Little Bay Samples Line 3B
Sample WP 188
Lat: N 43.113 Peak at: 91.2011
Lon: W 70.866
Clay+Silt: 56.7 %
Sand: 43.3 %
D50: 83.6 μm
Percent Size Fraction
Particle Size (um)

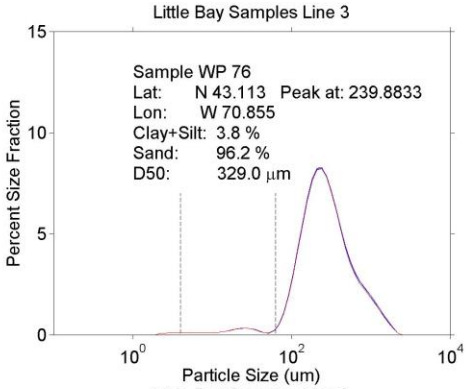
Little Bay Samples Line 3
Sample WP 76
Lat: N 43.113 Peak at: 239.8833
Lon: W 70.855
Clay+Silt: 3.8 %
Sand: 96.2 %
D50: 329.0 μm
Percent Size Fraction
Particle Size (um)

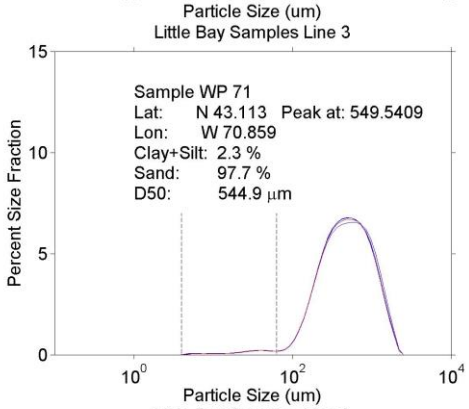
Little Bay Samples Line 3
Sample WP 71
Lat: N 43.113 Peak at: 549.5409
Lon: W 70.859
Clay+Silt: 2.3 %
Sand: 97.7 %
D50: 544.9 μm
Percent Size Fraction
Particle Size (um)

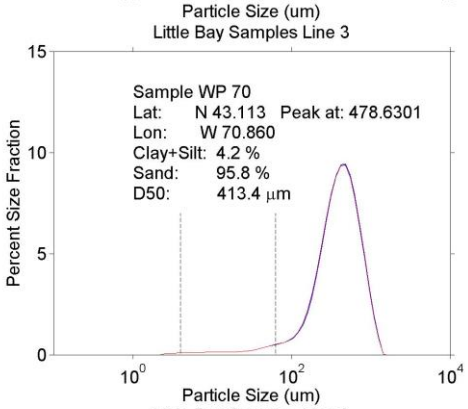
Little Bay Samples Line 3
Sample WP 70
Lat: N 43.113 Peak at: 478.6301
Lon: W 70.860
Clay+Silt: 4.2 %
Sand: 95.8 %
D50: 413.4 μm
Percent Size Fraction
Particle Size (um)

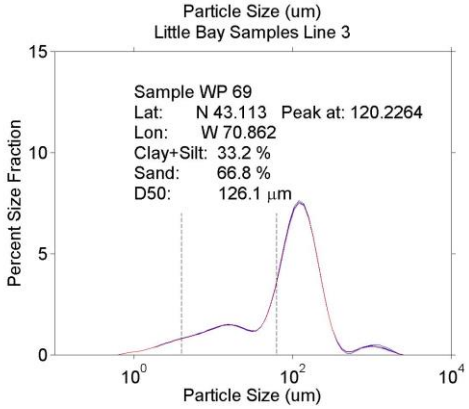
Little Bay Samples Line 3
Sample WP 69
Lat: N 43.113 Peak at: 120.2264
Lon: W 70.862
Clay+Silt: 33.2 %
Sand: 66.8 %
D50: 126.1 μm
Percent Size Fraction
Particle Size (um)

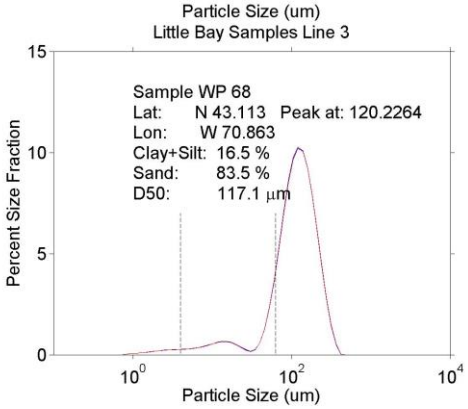
Little Bay Samples Line 3
Sample WP 68
Lat: N 43.113 Peak at: 120.2264
Lon: W 70.863
Clay+Silt: 16.5 %
Sand: 83.5 %
D50: 117.1 μm
Percent Size Fraction
Particle Size (um)

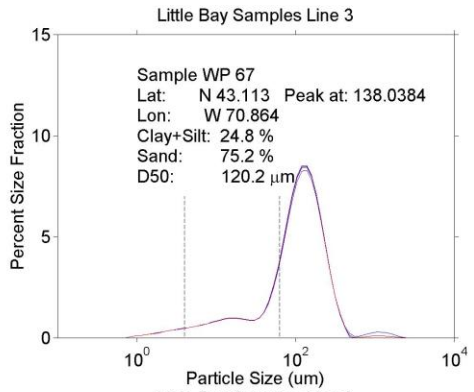
Little Bay Samples Line 3
Sample WP 67
Lat: N 43.113 Peak at: 138.0384
Lon: W 70.864
Clay+Silt: 24.8 %
Sand: 75.2 %
D50: 120.2 μm
Percent Size Fraction
Particle Size (um)

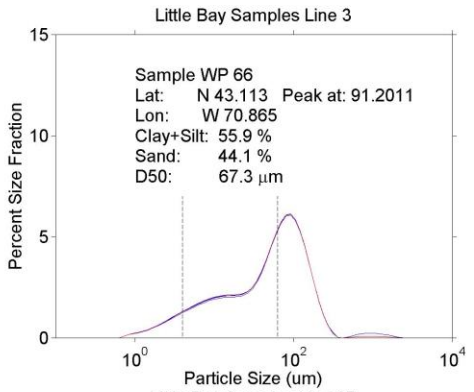
Little Bay Samples Line 3
Sample WP 66
Lat: N 43.113 Peak at: 91.2011
Lon: W 70.865
Clay+Silt: 55.9 %
Sand: 44.1 %
D50: 67.3 μm
Percent Size Fraction
Particle Size (um)

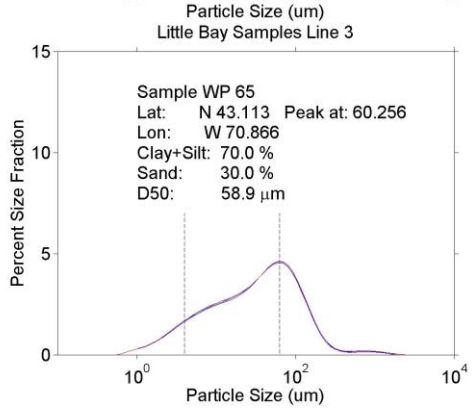
Little Bay Samples Line 3
Sample WP 65
Lat: N 43.113 Peak at: 60.256
Lon: W 70.866
Clay+Silt: 70.0 %
Sand: 30.0 %
D50: 58.9 μm
Percent Size Fraction
Particle Size (um)

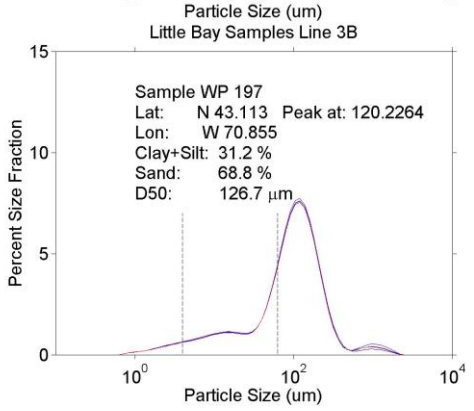
Little Bay Samples Line 3B
Sample WP 197
Lat: N 43.113 Peak at: 120.2264
Lon: W 70.855
Clay+Silt: 31.2 %
Sand: 68.8 %
D50: 126.7 μm
Percent Size Fraction
Particle Size (um)

Lines 4 and 5:

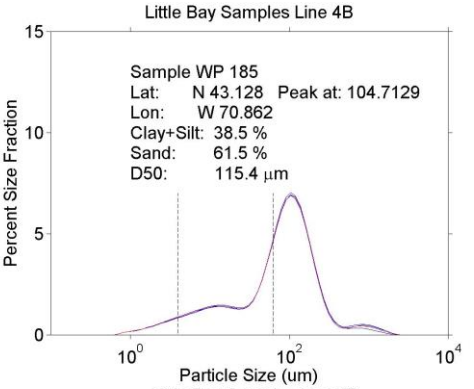
Little Bay Samples Line 4B
Sample WP 185
Lat: N 43.128 Peak at: 104.7129
Lon: W 70.862
Clay+Silt: 38.5 %
Sand: 61.5 %
D50: 115.4 μm
Percent Size Fraction
Particle Size (um)

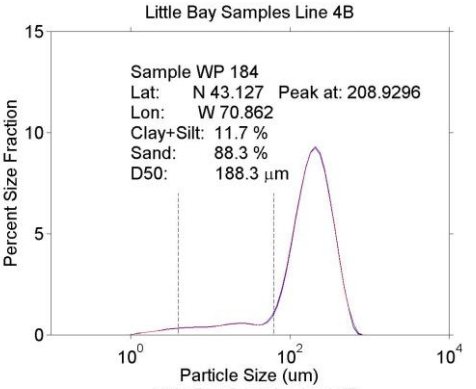
Little Bay Samples Line 4B
Sample WP 184
Lat: N 43.127 Peak at: 208.9296
Lon: W 70.862
Clay+Silt: 11.7 %
Sand: 88.3 %
D50: 188.3 μm
Percent Size Fraction
Particle Size (um)

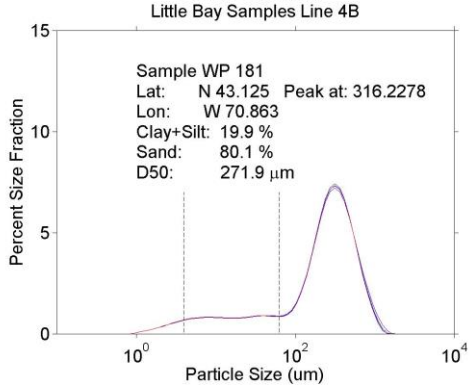
Little Bay Samples Line 4B
Sample WP 181
Lat: N 43.125 Peak at: 316.2278
Lon: W 70.863
Clay+Silt: 19.9 %
Sand: 80.1 %
D50: 271.9 μm
Percent Size Fraction
Particle Size (um)

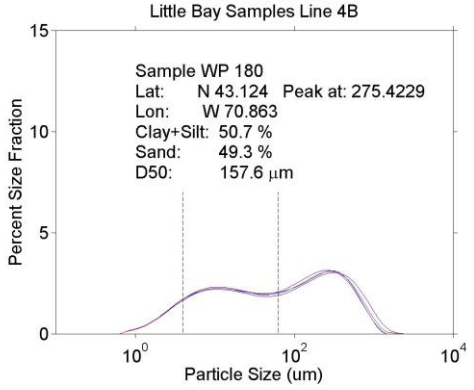
Little Bay Samples Line 4B
Sample WP 180
Lat: N 43.124 Peak at: 275.4229
Lon: W 70.863
Clay+Silt: 50.7 %
Sand: 49.3 %
D50: 157.6 μm
Percent Size Fraction
Particle Size (um)

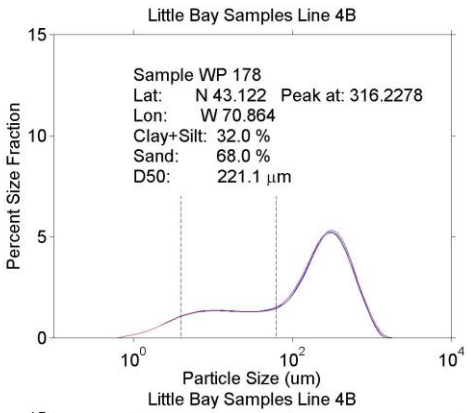
Little Bay Samples Line 4B
Sample WP 178
Lat: N 43.122 Peak at: 316.2278
Lon: W 70.864
Clay+Silt: 32.0 %
Sand: 68.0 %
D50: 221.1 μm
Percent Size Fraction
Particle Size (um)

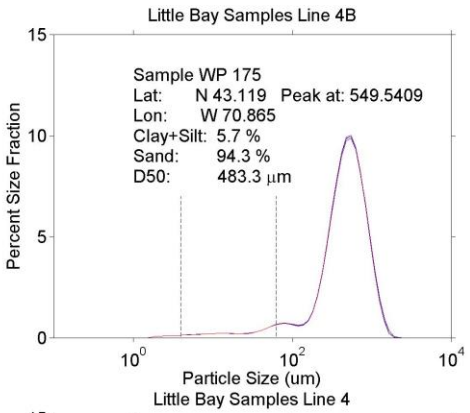
Little Bay Samples Line 4B
Sample WP 175
Lat: N 43.119 Peak at: 549.5409
Lon: W 70.865
Clay+Silt: 5.7 %
Sand: 94.3 %
D50: 483.3 μm
Percent Size Fraction
Particle Size (um)

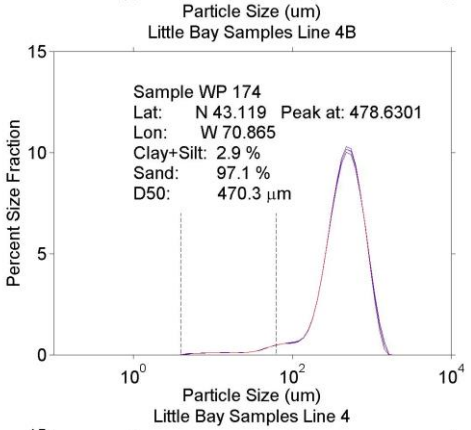
Little Bay Samples Line 4B
Sample WP 174
Lat: N 43.119 Peak at: 478.6301
Lon: W 70.865
Clay+Silt: 2.9 %
Sand: 97.1 %
D50: 470.3 μm
Percent Size Fraction
Particle Size (um)

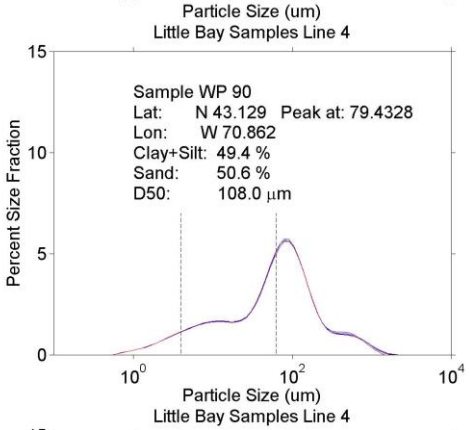
Little Bay Samples Line 4
Sample WP 90
Lat: N 43.129 Peak at: 79.4328
Lon: W 70.862
Clay+Silt: 49.4 %
Sand: 50.6 %
D50: 108.0 μm
Percent Size Fraction
Particle Size (um)

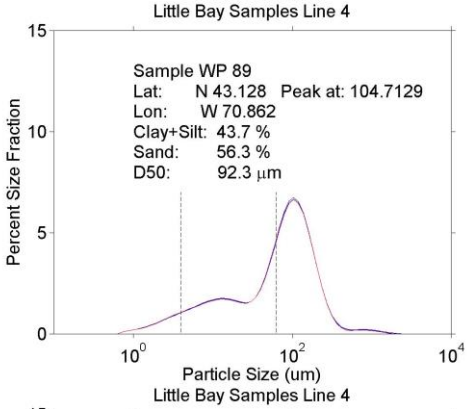
Little Bay Samples Line 4
Sample WP 89
Lat: N 43.128 Peak at: 104.7129
Lon: W 70.862
Clay+Silt: 43.7 %
Sand: 56.3 %
D50: 92.3 μm
Percent Size Fraction
Particle Size (um)

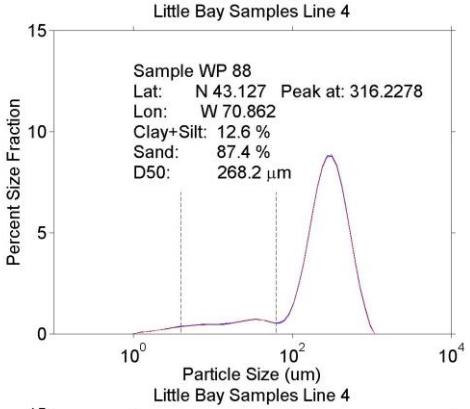
Little Bay Samples Line 4
Sample WP 88
Lat: N 43.127 Peak at: 316.2278
Lon: W 70.862
Clay+Silt: 12.6 %
Sand: 87.4 %
D50: 268.2 μm
Percent Size Fraction
Particle Size (um)

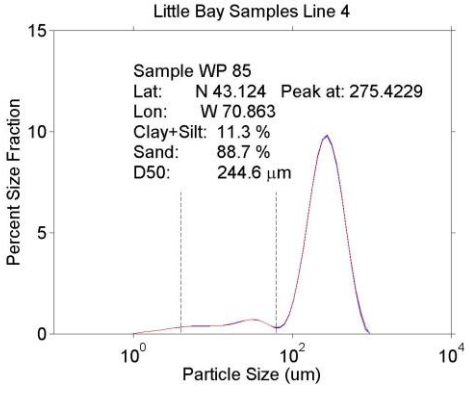
Little Bay Samples Line 4
Sample WP 85
Lat: N 43.124 Peak at: 275.4229
Lon: W 70.863
Clay+Silt: 11.3 %
Sand: 88.7 %
D50: 244.6 μm
Percent Size Fraction
Particle Size (um)

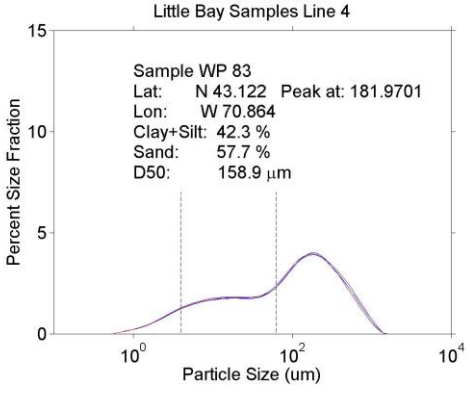
Little Bay Samples Line 4
Sample WP 83
Lat: N 43.122 Peak at: 181.9701
Lon: W 70.864
Clay+Silt: 42.3 %
Sand: 57.7 %
D50: 158.9 μm
Percent Size Fraction
Particle Size (um)

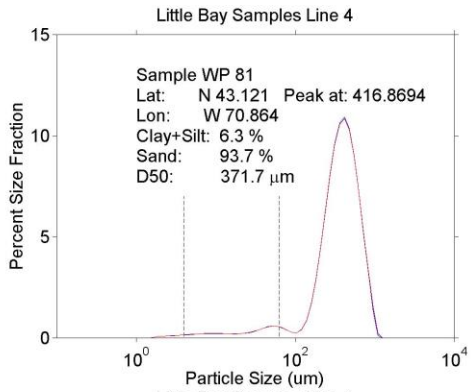
Little Bay Samples Line 4
Sample WP 81
Lat: N 43.121 Peak at: 416.8694
Lon: W 70.864
Clay+Silt: 6.3 %
Sand: 93.7 %
D50: 371.7 μm
Percent Size Fraction
Particle Size (um)

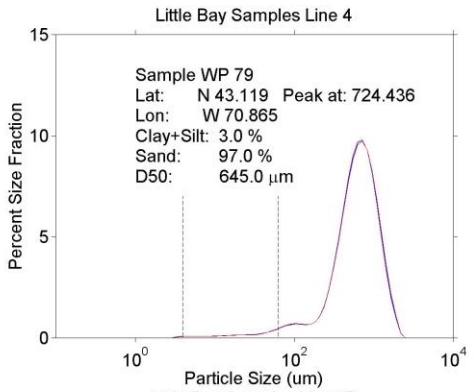
Little Bay Samples Line 4
Sample WP 79
Lat: N 43.119 Peak at: 724.436
Lon: W 70.865
Clay+Silt: 3.0 %
Sand: 97.0 %
D50: 645.0 μm
Percent Size Fraction
Particle Size (um)

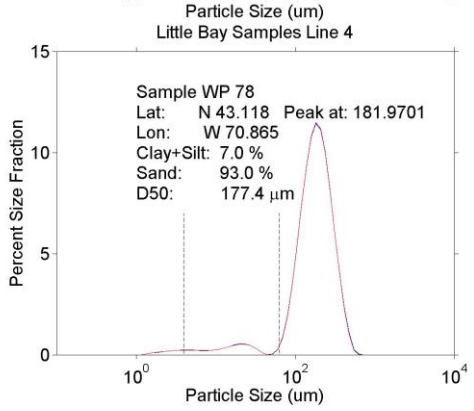
Little Bay Samples Line 4
Sample WP 78
Lat: N 43.118 Peak at: 181.9701
Lon: W 70.865
Clay+Silt: 7.0 %
Sand: 93.0 %
D50: 177.4 μm
Percent Size Fraction
Particle Size (um)

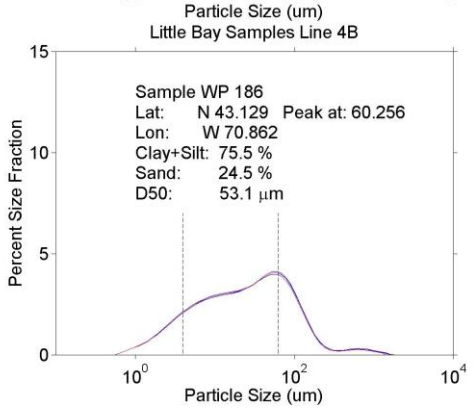
Little Bay Samples Line 4B
Sample WP 186
Lat: N 43.129 Peak at: 60.256
Lon: W 70.862
Clay+Silt: 75.5 %
Sand: 24.5 %
D50: 53.1 μm
Percent Size Fraction
Particle Size (um)

Line 6:

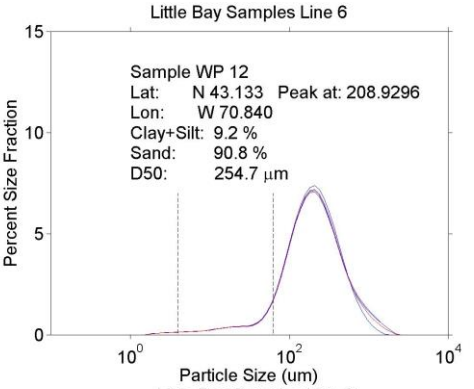
Little Bay Samples Line 6
Sample WP 12
Lat: N 43.133 Peak at: 208.9296
Lon: W 70.840
Clay+Silt: 9.2 %
Sand: 90.8 %
D50: 254.7 μm
Percent Size Fraction
Particle Size (um)

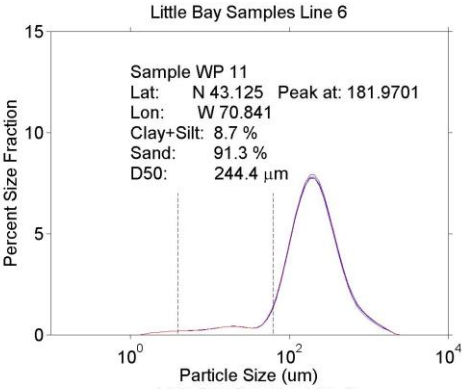
Little Bay Samples Line 6
Sample WP 11
Lat: N 43.125 Peak at: 181.9701
Lon: W 70.841
Clay+Silt: 8.7 %
Sand: 91.3 %
D50: 244.4 μm
Percent Size Fraction
Particle Size (um)

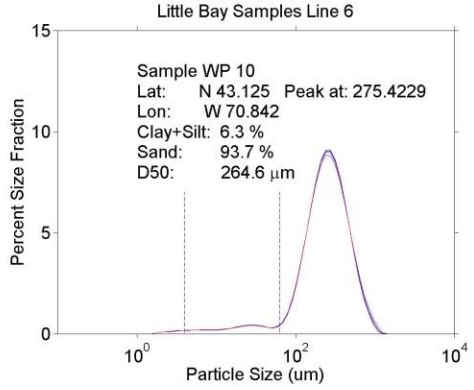
Little Bay Samples Line 6
Sample WP 10
Lat: N 43.125 Peak at: 275.4229
Lon: W 70.842
Clay+Silt: 6.3 %
Sand: 93.7 %
D50: 264.6 μm
Percent Size Fraction
Particle Size (um)

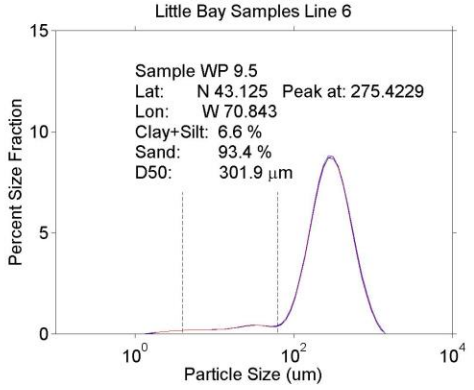
Little Bay Samples Line 6
Sample WP 9.5
Lat: N 43.125 Peak at: 275.4229
Lon: W 70.843
Clay+Silt: 6.6 %
Sand: 93.4 %
D50: 301.9 μm
Percent Size Fraction
Particle Size (um)

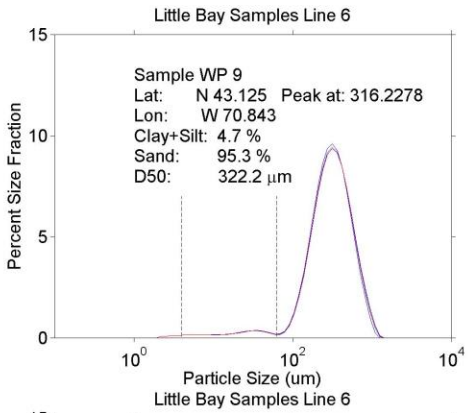
Little Bay Samples Line 6
Sample WP 9
Lat: N 43.125 Peak at: 316.2278
Lon: W 70.843
Clay+Silt: 4.7 %
Sand: 95.3 %
D50: 322.2 μm
Percent Size Fraction
Particle Size (um)

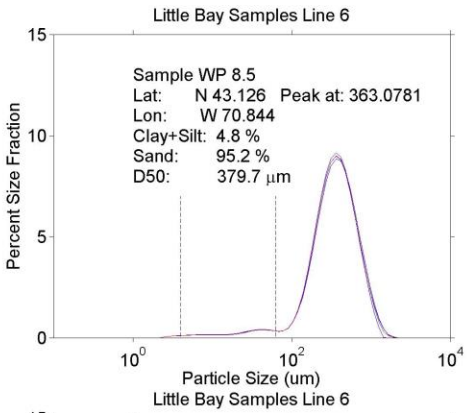
Little Bay Samples Line 6
Sample WP 8.5
Lat: N 43.126 Peak at: 363.0781
Lon: W 70.844
Clay+Silt: 4.8 %
Sand: 95.2 %
D50: 379.7 μm
Percent Size Fraction
Particle Size (um)

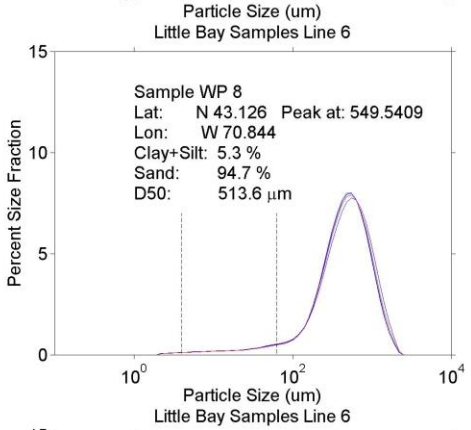
Little Bay Samples Line 6
Sample WP 8
Lat: N 43.126 Peak at: 549.5409
Lon: W 70.844
Clay+Silt: 5.3 %
Sand: 94.7 %
D50: 513.6 μm
Percent Size Fraction
Particle Size (um)

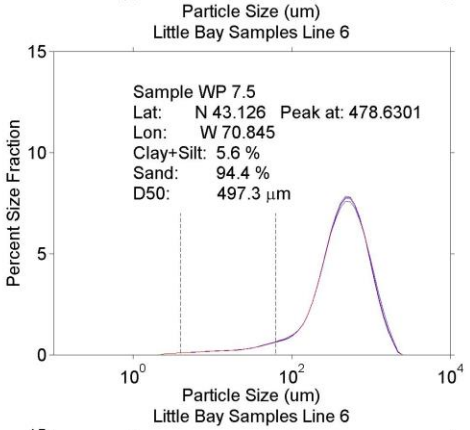
Little Bay Samples Line 6
Sample WP 7.5
Lat: N 43.126 Peak at: 478.6301
Lon: W 70.845
Clay+Silt: 5.6 %
Sand: 94.4 %
D50: 497.3 μm
Percent Size Fraction
Particle Size (um)

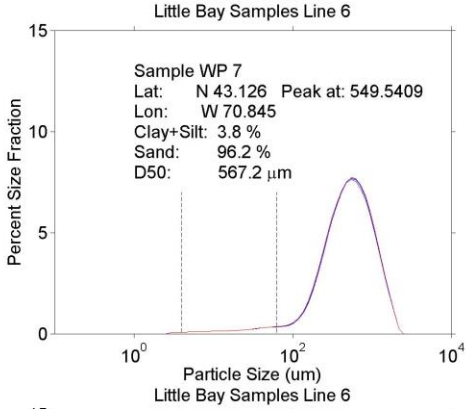
Little Bay Samples Line 6
Sample WP 7
Lat: N 43.126 Peak at: 549.5409
Lon: W 70.845
Clay+Silt: 3.8 %
Sand: 96.2 %
D50: 567.2 μm
Percent Size Fraction
Particle Size (um)

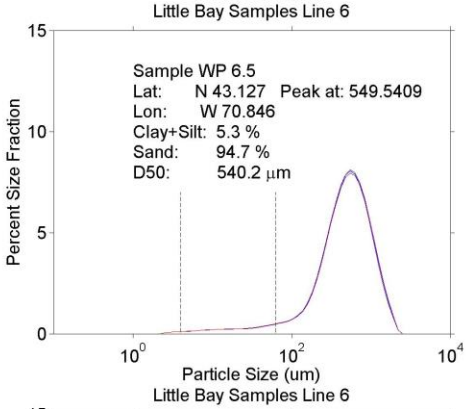
Little Bay Samples Line 6
Sample WP 6.5
Lat: N 43.127 Peak at: 549.5409
Lon: W 70.846
Clay+Silt: 5.3 %
Sand: 94.7 %
D50: 540.2 μm
Percent Size Fraction
Particle Size (um)

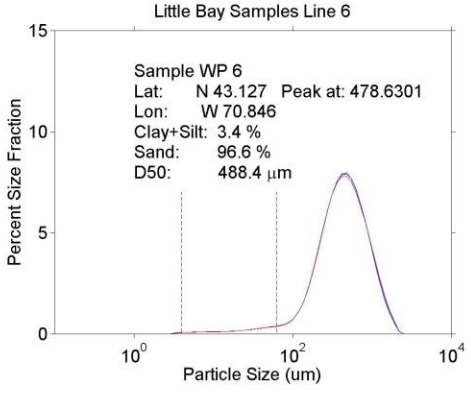
Little Bay Samples Line 6
Sample WP 6
Lat: N 43.127 Peak at: 478.6301
Lon: W 70.846
Clay+Silt: 3.4 %
Sand: 96.6 %
D50: 488.4 μm
Percent Size Fraction
Particle Size (um)

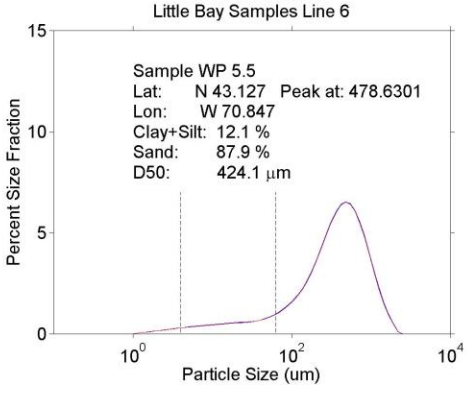
Little Bay Samples Line 6
Sample WP 5.5
Lat: N 43.127 Peak at: 478.6301
Lon: W 70.847
Clay+Silt: 12.1 %
Sand: 87.9 %
D50: 424.1 μm
Percent Size Fraction
Particle Size (um)

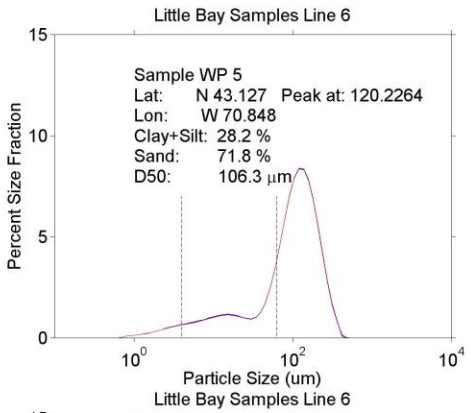
Little Bay Samples Line 6
Sample WP 5
Lat: N 43.127 Peak at: 120.2264
Lon: W 70.848
Clay+Silt: 28.2 %
Sand: 71.8 %
D50: 106.3 μm
Percent Size Fraction
Particle Size (um)

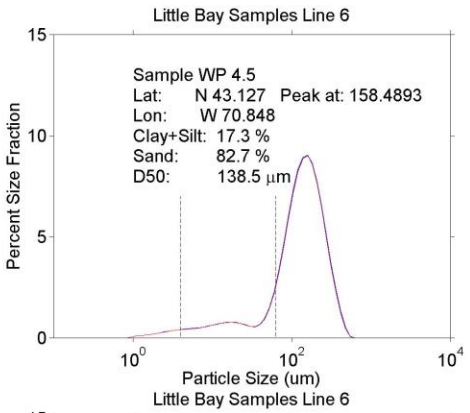
Little Bay Samples Line 6
Sample WP 4.5
Lat: N 43.127 Peak at: 158.4893
Lon: W 70.848
Clay+Silt: 17.3 %
Sand: 82.7 %
D50: 138.5 μm
Percent Size Fraction
Particle Size (um)

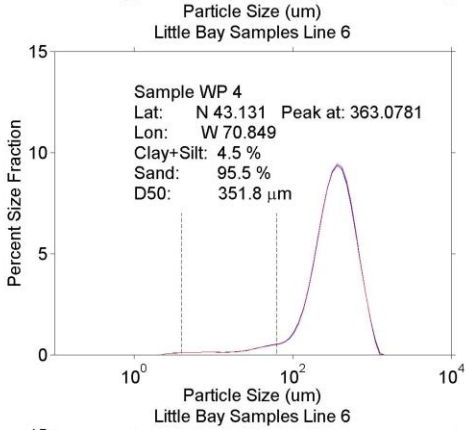
Little Bay Samples Line 6
Sample WP 4
Lat: N 43.131 Peak at: 363.0781
Lon: W 70.849
Clay+Silt: 4.5 %
Sand: 95.5 %
D50: 351.8 μm
Percent Size Fraction
Particle Size (um)

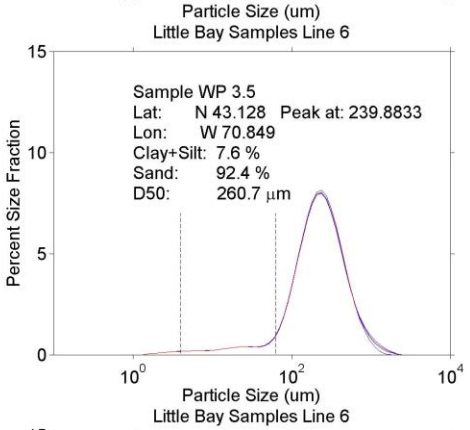
Little Bay Samples Line 6
Sample WP 3.5
Lat: N 43.128 Peak at: 239.8833
Lon: W 70.849
Clay+Silt: 7.6 %
Sand: 92.4 %
D50: 260.7 μm
Percent Size Fraction
Particle Size (um)

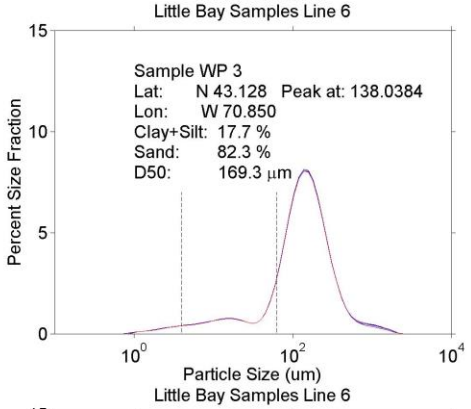
Little Bay Samples Line 6
Sample WP 3
Lat: N 43.128 Peak at: 138.0384
Lon: W 70.850
Clay+Silt: 17.7 %
Sand: 82.3 %
D50: 169.3 μm
Percent Size Fraction
Particle Size (um)

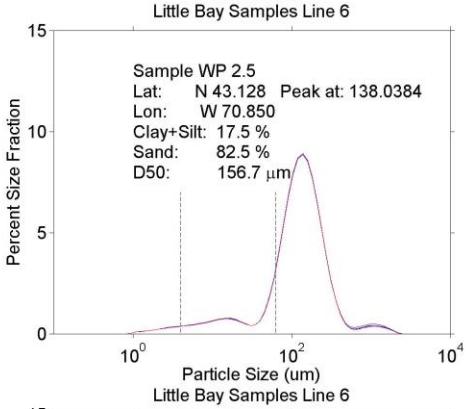
Little Bay Samples Line 6
Sample WP 2.5
Lat: N 43.128 Peak at: 138.0384
Lon: W 70.850
Clay+Silt: 17.5 %
Sand: 82.5 %
D50: 156.7 μm
Percent Size Fraction
Particle Size (um)

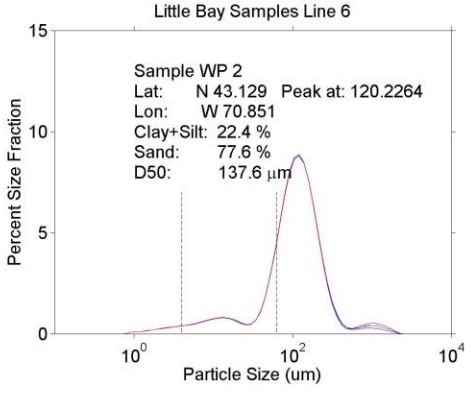
Little Bay Samples Line 6
Sample WP 2
Lat: N 43.129 Peak at: 120.2264
Lon: W 70.851
Clay+Silt: 22.4 %
Sand: 77.6 %
D50: 137.6 μm
Percent Size Fraction
Particle Size (um)

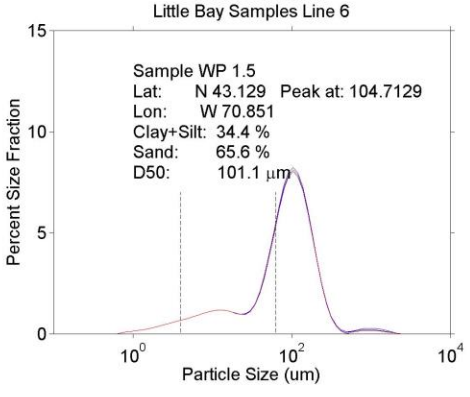
Little Bay Samples Line 6
Sample WP 1.5
Lat: N 43.129 Peak at: 104.7129
Lon: W 70.851
Clay+Silt: 34.4 %
Sand: 65.6 %
D50: 101.1 μm
Percent Size Fraction
Particle Size (um)

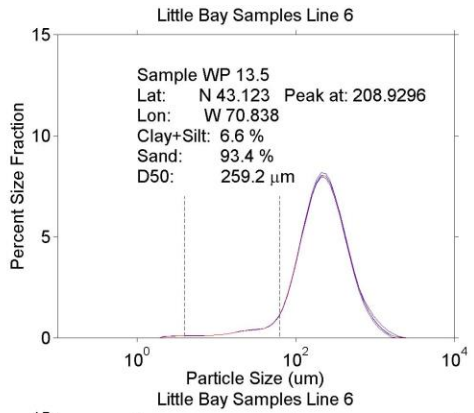
Little Bay Samples Line 6
Sample WP 13.5
Lat: N 43.123 Peak at: 208.9296
Lon: W 70.838
Clay+Silt: 6.6 %
Sand: 93.4 %
D50: 259.2 μm
Percent Size Fraction
Particle Size (um)

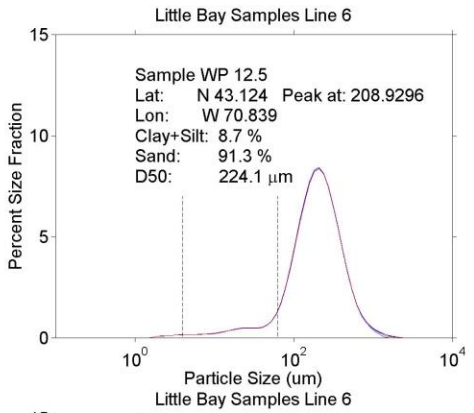
Little Bay Samples Line 6
Sample WP 12.5
Lat: N 43.124 Peak at: 208.9296
Lon: W 70.839
Clay+Silt: 8.7 %
Sand: 91.3 %
D50: 224.1 μm
Percent Size Fraction
Particle Size (um)

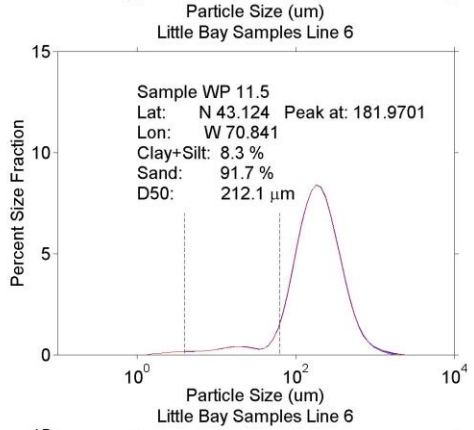
Little Bay Samples Line 6
Sample WP 11.5
Lat: N 43.124 Peak at: 181.9701
Lon: W 70.841
Clay+Silt: 8.3 %
Sand: 91.7 %
D50: 212.1 μm
Percent Size Fraction
Particle Size (um)

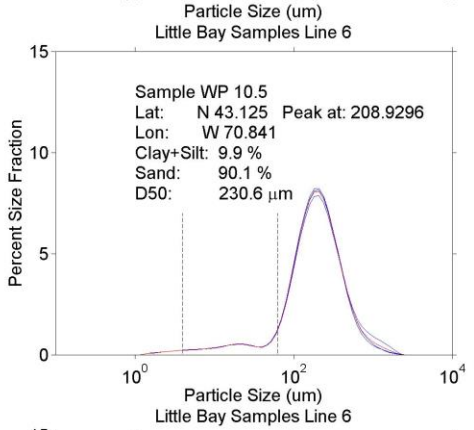
Little Bay Samples Line 6
Sample WP 10.5
Lat: N 43.125 Peak at: 208.9296
Lon: W 70.841
Clay+Silt: 9.9 %
Sand: 90.1 %
D50: 230.6 μm
Percent Size Fraction
Particle Size (um)

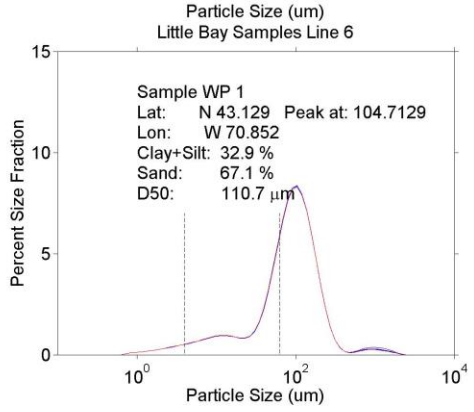
Little Bay Samples Line 6
Sample WP 1
Lat: N 43.129 Peak at: 104.7129
Lon: W 70.852
Clay+Silt: 32.9 %
Sand: 67.1 %
D50: 110.7 μm
Percent Size Fraction
Particle Size (um)

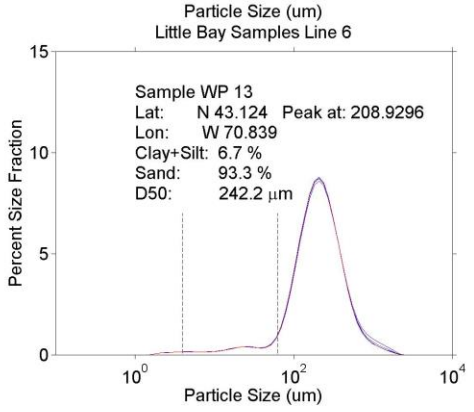
Little Bay Samples Line 6
Sample WP 13
Lat: N 43.124 Peak at: 208.9296
Lon: W 70.839
Clay+Silt: 6.7 %
Sand: 93.3 %
D50: 242.2 μm
Percent Size Fraction
Particle Size (um)

Line 7:

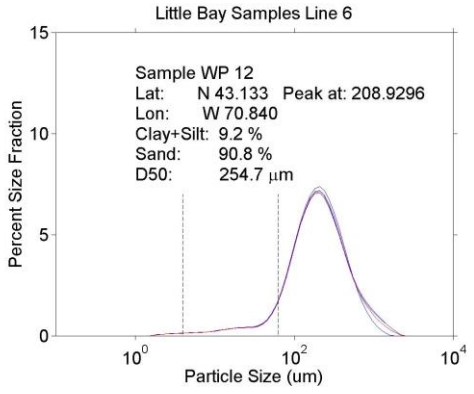
Little Bay Samples Line 6
Sample WP 12
Lat: N 43.133 Peak at: 208.9296
Lon: W 70.840
Clay+Silt: 9.2 %
Sand: 90.8 %
D50: 254.7 μm
Percent Size Fraction
Particle Size (um)

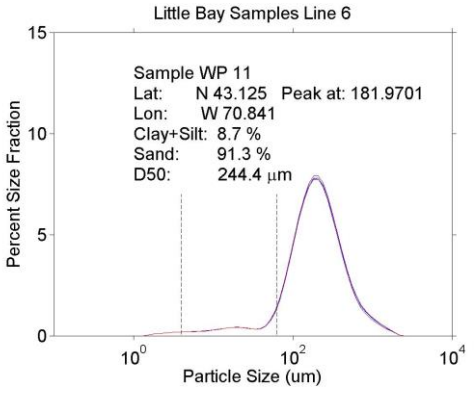
Little Bay Samples Line 6
Sample WP 11
Lat: N 43.125 Peak at: 181.9701
Lon: W 70.841
Clay+Silt: 8.7 %
Sand: 91.3 %
D50: 244.4 μm
Percent Size Fraction
Particle Size (um)

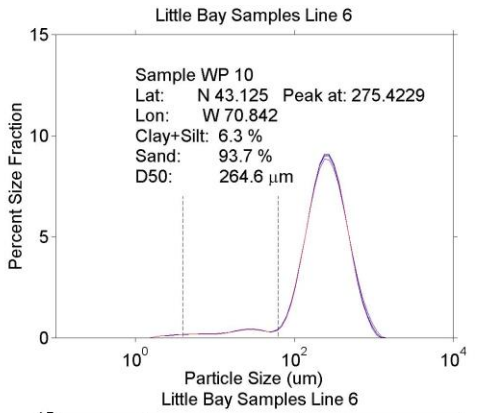
Little Bay Samples Line 6
Sample WP 10
Lat: N 43.125 Peak at: 275.4229
Lon: W 70.842
Clay+Silt: 6.3 %
Sand: 93.7 %
D50: 264.6 μm
Percent Size Fraction
Particle Size (um)

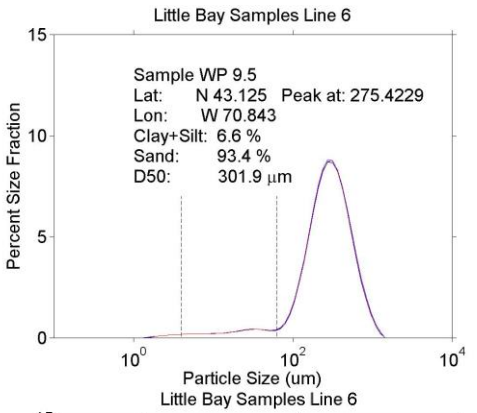
Little Bay Samples Line 6
Sample WP 9.5
Lat: N 43.125 Peak at: 275.4229
Lon: W 70.843
Clay+Silt: 6.6 %
Sand: 93.4 %
D50: 301.9 μm
Percent Size Fraction
Particle Size (um)

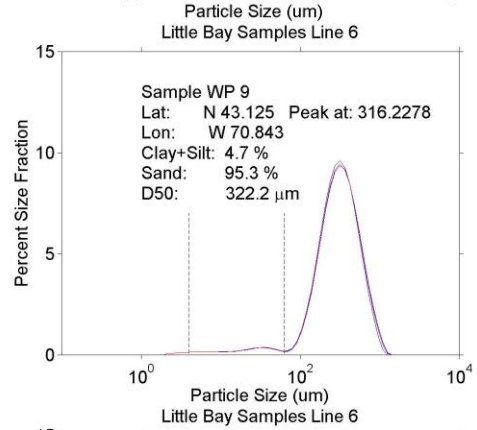
Little Bay Samples Line 6
Sample WP 9
Lat: N 43.125 Peak at: 316.2278
Lon: W 70.843
Clay+Silt: 4.7 %
Sand: 95.3 %
D50: 322.2 μm
Percent Size Fraction
Particle Size (um)

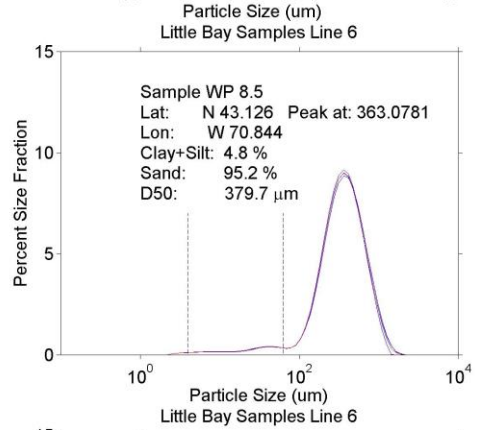
Little Bay Samples Line 6
Sample WP 8.5
Lat: N 43.126 Peak at: 363.0781
Lon: W 70.844
Clay+Silt: 4.8 %
Sand: 95.2 %
D50: 379.7 μm
Percent Size Fraction
Particle Size (um)

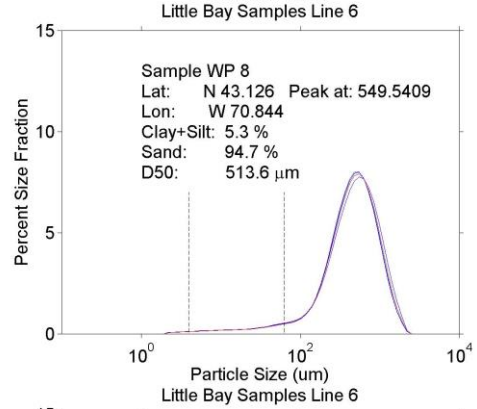
Little Bay Samples Line 6
Sample WP 8
Lat: N 43.126 Peak at: 549.5409
Lon: W 70.844
Clay+Silt: 5.3 %
Sand: 94.7 %
D50: 513.6 μm
Percent Size Fraction
Particle Size (um)

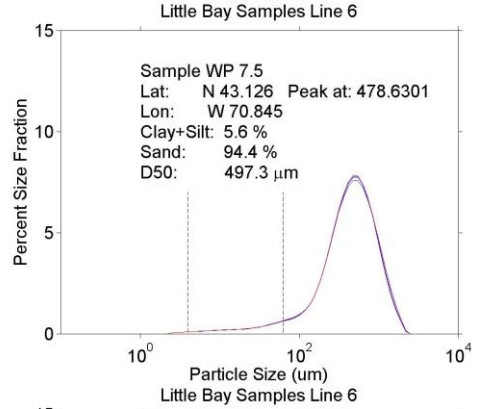
Little Bay Samples Line 6
Sample WP 7.5
Lat: N 43.126 Peak at: 478.6301
Lon: W 70.845
Clay+Silt: 5.6 %
Sand: 94.4 %
D50: 497.3 μm
Percent Size Fraction
Particle Size (um)

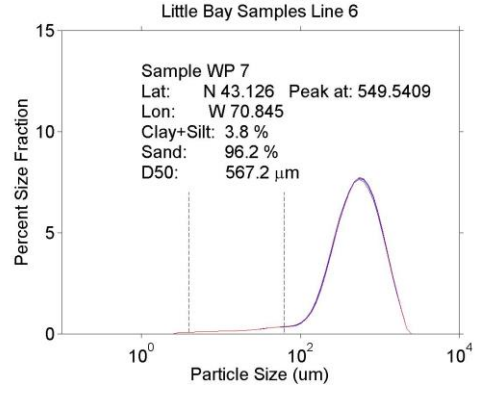
Little Bay Samples Line 6
Sample WP 7
Lat: N 43.126 Peak at: 549.5409
Lon: W 70.845
Clay+Silt: 3.8 %
Sand: 96.2 %
D50: 567.2 μm
Percent Size Fraction
Particle Size (um)

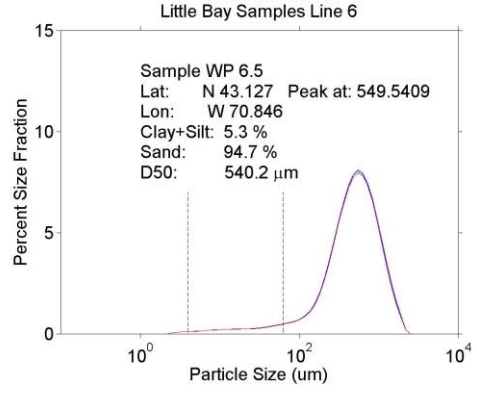
Little Bay Samples Line 6
Sample WP 6.5
Lat: N 43.127 Peak at: 549.5409
Lon: W 70.846
Clay+Silt: 5.3 %
Sand: 94.7 %
D50: 540.2 μm
Percent Size Fraction
Particle Size (um)

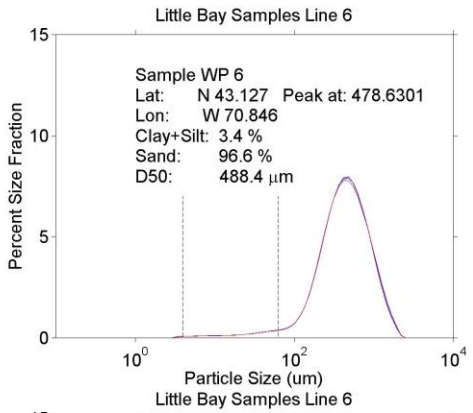
Little Bay Samples Line 6
Sample WP 6
Lat: N 43.127 Peak at: 478.6301
Lon: W 70.846
Clay+Silt: 3.4 %
Sand: 96.6 %
D50: 488.4 μm
Percent Size Fraction
Particle Size (um)

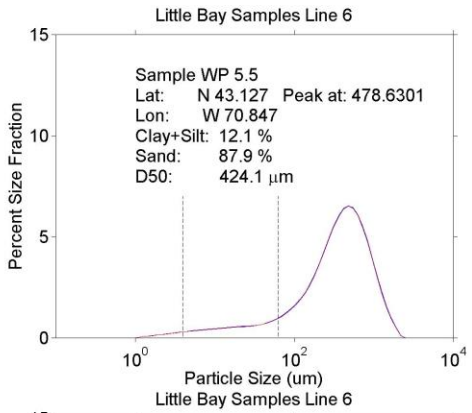
Little Bay Samples Line 6
Sample WP 5.5
Lat: N 43.127 Peak at: 478.6301
Lon: W 70.847
Clay+Silt: 12.1 %
Sand: 87.9 %
D50: 424.1 μm
Percent Size Fraction
Particle Size (um)

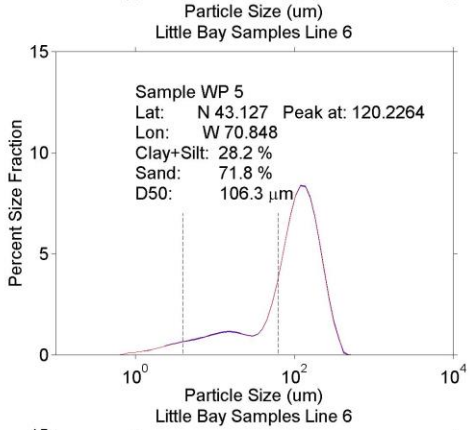
Little Bay Samples Line 6
Sample WP 5
Lat: N 43.127 Peak at: 120.2264
Lon: W 70.848
Clay+Silt: 28.2 %
Sand: 71.8 %
D50: 106.3 μm
Percent Size Fraction
Particle Size (um)

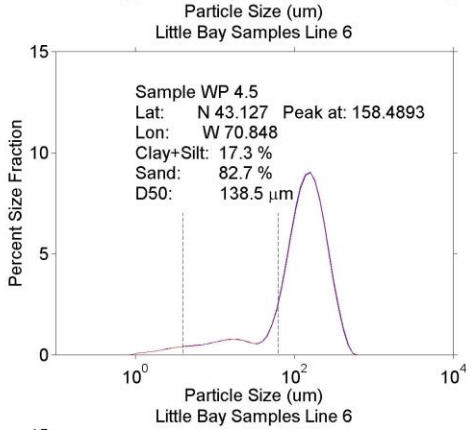
Little Bay Samples Line 6
Sample WP 4.5
Lat: N 43.127 Peak at: 158.4893
Lon: W 70.848
Clay+Silt: 17.3 %
Sand: 82.7 %
D50: 138.5 μm
Percent Size Fraction
Particle Size (um)

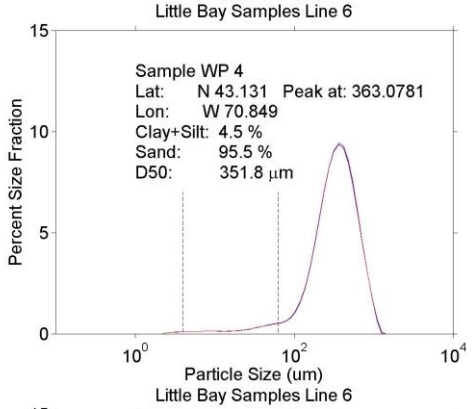
Little Bay Samples Line 6
Sample WP 4
Lat: N 43.131 Peak at: 363.0781
Lon: W 70.849
Clay+Silt: 4.5 %
Sand: 95.5 %
D50: 351.8 μm
Percent Size Fraction
Particle Size (um)

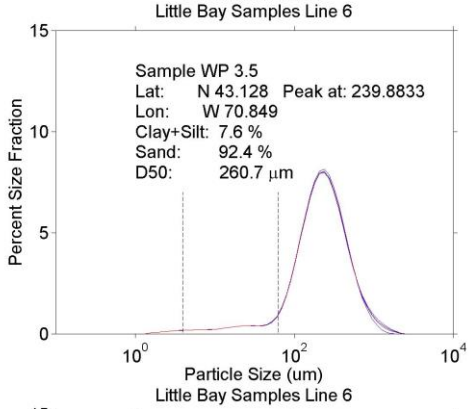
Little Bay Samples Line 6
Sample WP 3.5
Lat: N 43.128 Peak at: 239.8833
Lon: W 70.849
Clay+Silt: 7.6 %
Sand: 92.4 %
D50: 260.7 μm
Percent Size Fraction
Particle Size (um)

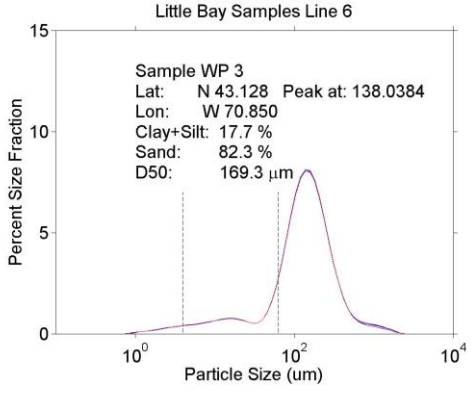
Little Bay Samples Line 6
Sample WP 3
Lat: N 43.128 Peak at: 138.0384
Lon: W 70.850
Clay+Silt: 17.7 %
Sand: 82.3 %
D50: 169.3 μm
Percent Size Fraction
Particle Size (um)

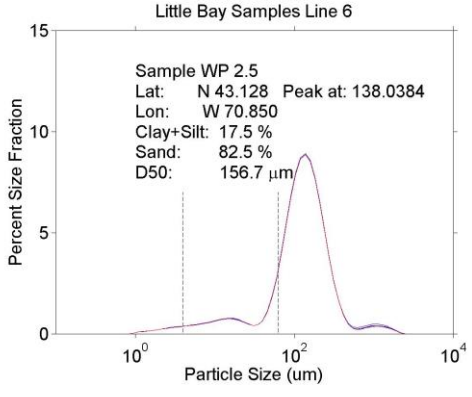
Little Bay Samples Line 6
Sample WP 2.5
Lat: N 43.128 Peak at: 138.0384
Lon: W 70.850
Clay+Silt: 17.5 %
Sand: 82.5 %
D50: 156.7 μm
Percent Size Fraction
Particle Size (um)

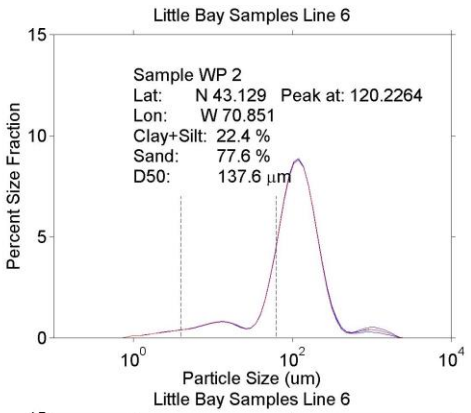
Little Bay Samples Line 6
Sample WP 2
Lat: N 43.129 Peak at: 120.2264
Lon: W 70.851
Clay+Silt: 22.4 %
Sand: 77.6 %
D50: 137.6 μm
Percent Size Fraction
Particle Size (um)

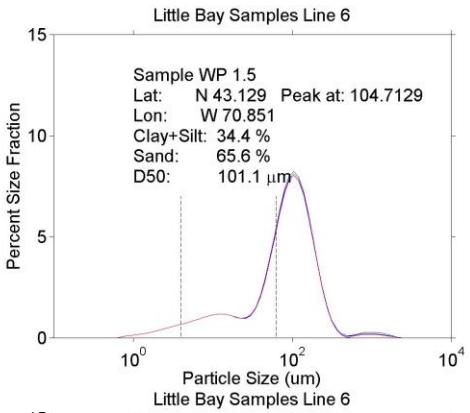
Little Bay Samples Line 6
Sample WP 1.5
Lat: N 43.129 Peak at: 104.7129
Lon: W 70.851
Clay+Silt: 34.4 %
Sand: 65.6 %
D50: 101.1 μm
Percent Size Fraction
Particle Size (um)

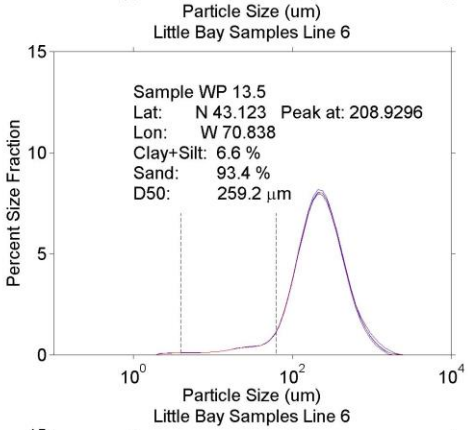
Little Bay Samples Line 6
Sample WP 13.5
Lat: N 43.123 Peak at: 208.9296
Lon: W 70.838
Clay+Silt: 6.6 %
Sand: 93.4 %
D50: 259.2 μm
Percent Size Fraction
Particle Size (um)

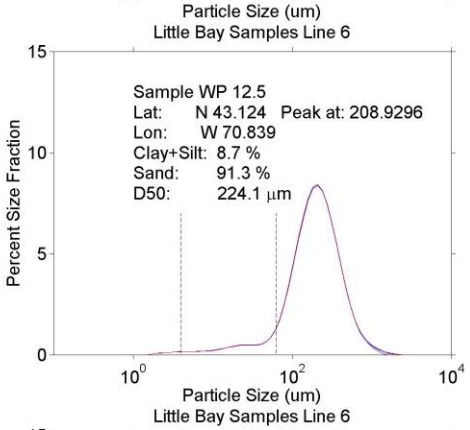
Little Bay Samples Line 6
Sample WP 12.5
Lat: N 43.124 Peak at: 208.9296
Lon: W 70.839
Clay+Silt: 8.7 %
Sand: 91.3 %
D50: 224.1 μm
Percent Size Fraction
Particle Size (um)

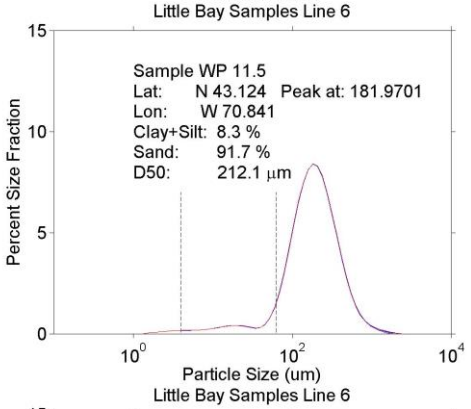
Little Bay Samples Line 6
Sample WP 11.5
Lat: N 43.124 Peak at: 181.9701
Lon: W 70.841
Clay+Silt: 8.3 %
Sand: 91.7 %
D50: 212.1 μm
Percent Size Fraction
Particle Size (um)

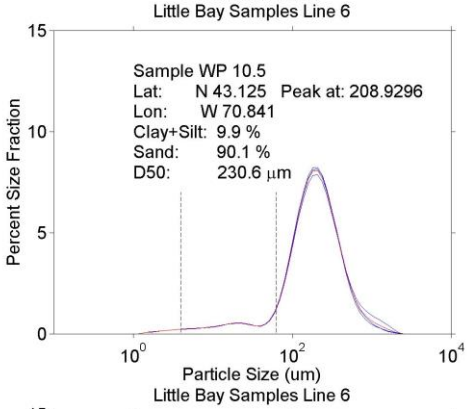
Little Bay Samples Line 6
Sample WP 10.5
Lat: N 43.125 Peak at: 208.9296
Lon: W 70.841
Clay+Silt: 9.9 %
Sand: 90.1 %
D50: 230.6 μm
Percent Size Fraction
Particle Size (um)

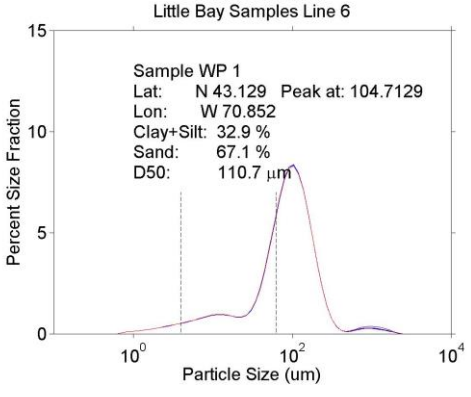
Little Bay Samples Line 6
Sample WP 1
Lat: N 43.129 Peak at: 104.7129
Lon: W 70.852
Clay+Silt: 32.9 %
Sand: 67.1 %
D50: 110.7 μm
Percent Size Fraction
Particle Size (um)

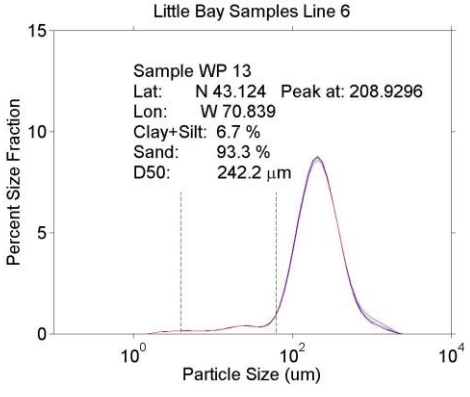
Little Bay Samples Line 6
Sample WP 13
Lat: N 43.124 Peak at: 208.9296
Lon: W 70.839
Clay+Silt: 6.7 %
Sand: 93.3 %
D50: 242.2 μm
Percent Size Fraction
Particle Size (um)

D – EOF Modes

Though only the first mode of the EOF analysis was considered for purposes of modelling, there are as many modes as there are properties used in the EOF analysis. Below are the 7 modes (in order from 1 to 7) resulting from the EOF analysis of all 7 waveform properties.

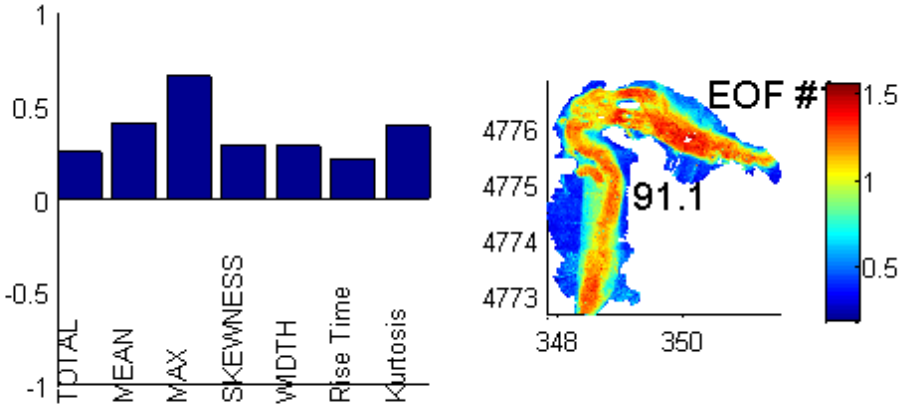

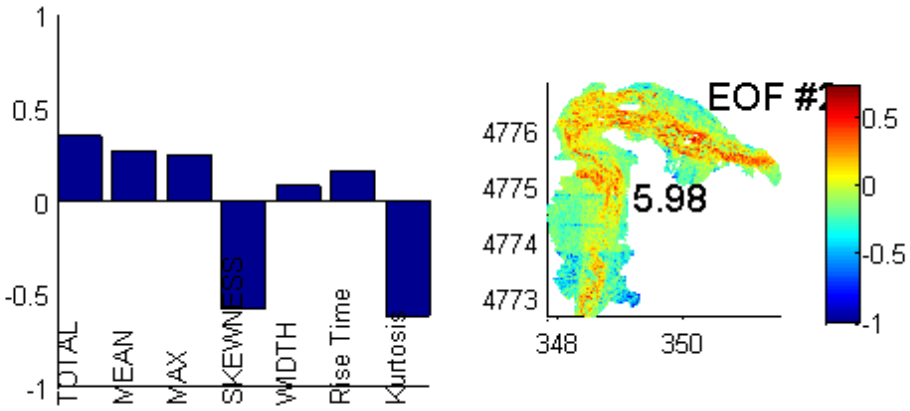

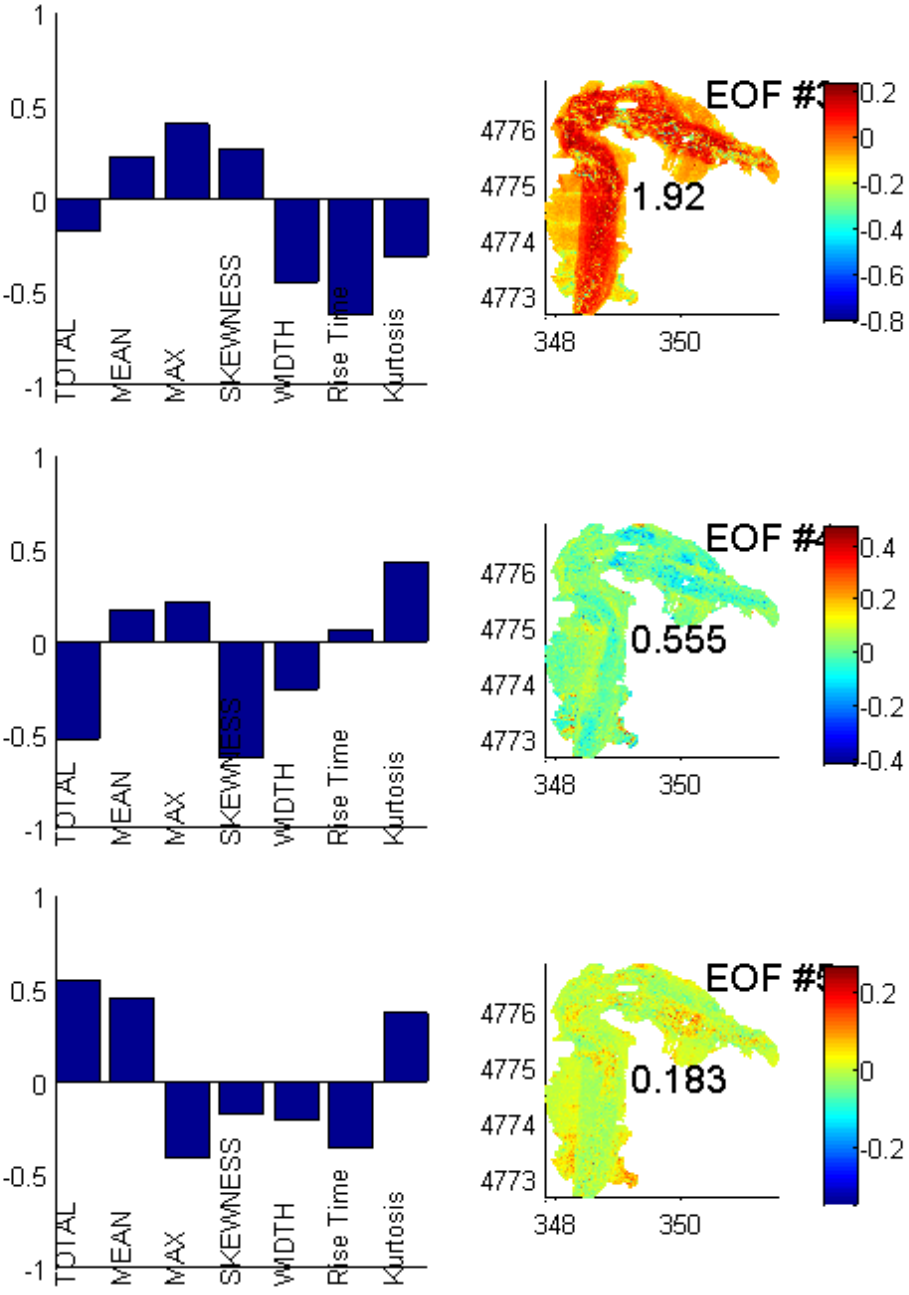
1
0.5
0
-0.5
-1
TOTAL
MEAN
MAX
SKEWNESS
WIDTH
Rise Time
Kurtosis
EOF #1
1.92
4776
4775
4774
4773
348
350
0.2
0
-0.2
-0.4
-0.6
-0.8
EOF #4
0.555
0.4
0.2
0
-0.2
-0.4
EOF #5
0.183

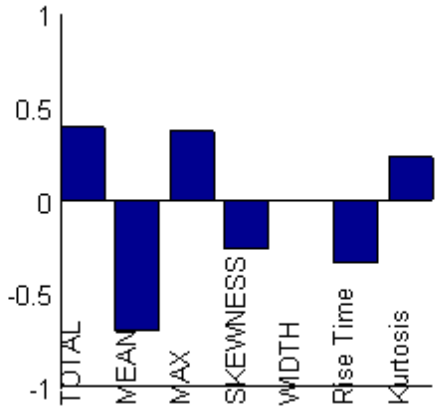
1
0.5
0
-0.5
-1
TOTAL
MEAN
MAX
SKEWNESS
WIDTH
Rise Time
Kurtosis

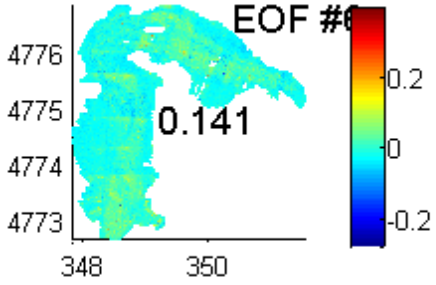
EOF #6
4776
4775
4774
4773
0.141
348
350
0.2
0
-0.2

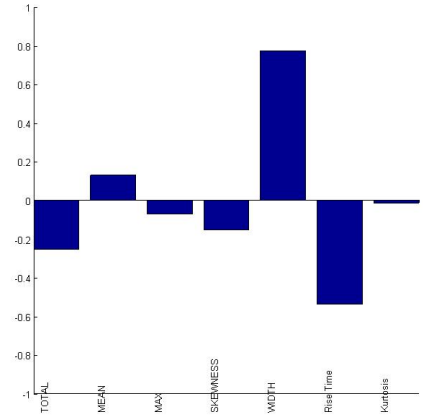
1
0.8
0.6
0.4
0.2
0
-0.2
-0.4
-0.6
-0.8
-1
TOTAL
MEAN
MAX
SKEWNESS
WIDTH
Rise Time
Kurtosis

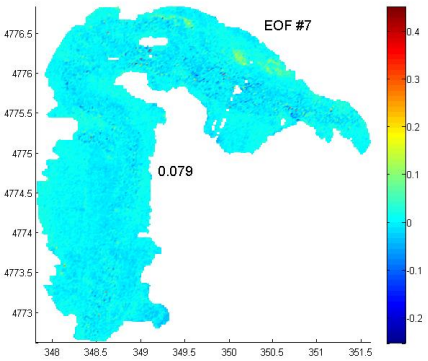
EOF #7
4776.5
4776
4775.5
4775
4774.5
4774
4773.5
4773
0.079
348
348.5
349
349.5
350
350.5
351
351.5
0.4
0.3
0.2
0.1
0
-0.1
-0.2